Graduate School ETD Form 9
(Revised 01/14)

PURDUE UNIVERSITY
GRADUATE SCHOOL
Thesis/Dissertation Acceptance

This is to certify that the thesis/dissertation prepared

By Adeel Altaf

Entitled
Spectroscopy of Ultracold LiRb Molecules Using Ionization Detection

For the degree of Doctor of Philosophy

Is approved by the final examining committee:

Daniel S. Elliott

Yong P. Chen

David D. Nolte

Ephraim Fischbach

To the best of my knowledge and as understood by the student in the *Thesis/Dissertation Agreement. Publication Delay, and Certification/Disclaimer (Graduate School Form 32)*, this thesis/dissertation adheres to the provisions of Purdue University's "Policy on Integrity in Research" and the use of copyrighted material.

Daniel S. Elliott

Approved by Major Professor(s): _____

_____

Approved by: Mark Haugan 02/26/2014

Head of the Department Graduate Program Date

SPECTROSCOPY OF ULTRACOLD LIRB MOLECULES USING IONIZATION DETECTION

A Dissertation

Submitted to the Faculty

of

Purdue University

by

Adeel Altaf

In Partial Fulfillment of the

Requirements for the Degree

of

Doctor of Philosophy

May 2014

Purdue University

West Lafayette, Indiana

To my father and brother, and my mother (1960 – 2008)

ACKNOWLEDGMENTS

I would like to thank my PhD advisor, Dr. Daniel S. Elliott, for his immense support and encouragement during my graduate career. He has been a tremendous source of knowledge and expertise, and has been a constant guide from my first day in the lab. Gratitude is also due to my co-advisor, Dr. Yong P. Chen, for his significant input on the LiRb project. His keen insight into technical matters and grasp of fundamental principles has been instrumental in driving the research in our lab.

I also thank Dr. Ephraim Fischbach and Dr. David Nolte for graciously agreeing to serve on my committee. Their respective mathematical physics and quantum optics courses have served me well through graduate school.

It has been a privilege working with Sourav Dutta and John Lorenz, the two other graduate students who have been involved in the LiRb project since its conception. They have been instrumental in getting the experimental apparatus in the excellent working condition it is currently in. I have learned a great deal from our interactions, ranging from design of our experiment to interpretation of the acquired data. In addition, I would like to thank Dionysis Antypas who also joined the lab at the same time as I did, and worked on the precision measurement experiment. Our frequent discussions on technical aspects of experiments have been of great value and benefit, as have our conversations on all sorts of topics completely unrelated to research.

I would also like to thank Dr. Jesús Pérez-Ríos for helpful discussions and theoretical calculations related to the ground and excited state ionization spectroscopy data. Dr. Daniel Leaird has been very helpful to me during my time setting up and working with the femtosecond Ti:S laser, and offered great insight into optics in general and fiber optics in particular. I'd also like to thank Dave Azpell for the many electronic systems he has repaired and even more instruments he has lent to us. Special thanks to Sandy Formica for knowing answers to questions before I asked them, and taking care of paperwork in which I would otherwise have drowned.

My time at Purdue has been all the more special due to the friends I made here. In particular, Dr. Rameez Chatni has been a source of inspiration and support throughout the numerous ups and downs of graduate school, and I cannot thank him enough for this. The friendships I have developed playing cricket during the summer months will remain with me and have been a source of joy throughout my time at Purdue.

I want to thank my father and brother for their constant support and encouragement throughout my PhD. It has not always been easy going, but they have always been there for me and given their unconditional support to my academic pursuits. I would not be where I am without their love and good wishes. As for my mother, her unconditional love, wishes and prayers have made me the person I am today. May she rest in peace.

TABLE OF CONTENTS

Page

Page

Page

ABSTRACT

Altaf, Adeel. Ph.D., Purdue University, May 2014. Spectroscopy of ultracold LiRb molecules using ionization detection. Major Professor: Daniel S. Elliott.

We present spectroscopic studies of ultracold LiRb molecules using ionization detection. The molecules are created by cooling and trapping Li and Rb atoms in overlapping magneto-optical traps (MOTs) and using light resonant with a free-bound transition to create weakly bound excited state molecules in a process known as photoassociation (PA). We explore weakly bound vibrational levels of LiRb with PA spectroscopy using ionization detection and, where possible, compare our results with earlier measurements performed in our lab using trap-loss spectroscopy. In addition, we also probe vibrational levels of the ground triplet electronic state and excited electronic states using resonantly enhanced multiphoton ionization (REMPI) spectroscopy. We identify several vibrational levels of the $a^3\Sigma^+$, $(3)^3\Pi_\Omega$ and $(4)^3\Sigma^+$ states and compare our observations with theoretical calculations. As LiRb is one of the least studied heteronuclear diatomic molecules, these studies are aimed towards exploring the molecular structure. The spectroscopic work is also in line with the long-term project goals of transferring ultracold LiRb molecules into the lowest rotational and vibrational levels of the ground singlet electronic state. Molecules in this rovibronic ground state possess a large electric dipole moment, which is essential for application of ultracold molecules in various quantum computation schemes. The rovibronic ground state will also be an ideal starting point for investigating molecular entangled states.

1. INTRODUCTION

1.1 Why ultracold molecules?

There has been immense interest recently in the atomic, molecular and optical (AMO) physics community to create and probe ultracold molecules. These are molecules with translational kinetic energy less than 1 mK. The versatility – and hence attractiveness – of ultracold molecules is seen in their application in many different areas of scientific research, such as ultracold chemistry [1, 2, 3], quantum information processing [4, 5, 6], novel quantum phase transitions [7, 8, 9], coherent control [10, 11, 12] and test grounds for the fundamental forces of nature [13, 14, 15], among others. Many of these research endeavors are fueled by the rich and complex structure of ultracold molecules due to various degrees of freedom, and the novel interactions that result from operating in the ultracold regime.

One focus in ultracold molecules has been ultracold diatomic alkali molecules. With their simple electronic structure, alkali atoms offer a convenient starting point for diatomic molecular systems, which are the simplest type of molecules that can be created and studied. In addition, the technology and experimental techniques to manipulate alkali atoms are highly advanced, with many groups around the world regularly producing and investigating ultracold alkali atomic systems.

Among ultracold diatomic molecules we differentiate between homonuclear and heteronuclear molecules. A brief history of work on homonuclear molecules will be presented later in the chapter. As the focus of this thesis is heteronuclear (LiRb) molecules, we next discuss some of their important features that are relevant to our research.

1.1.1 The appeal of ultracold heteronuclear molecules

In our laboratory, we have been engaged in an experimental program whose goal is to create ultracold LiRb molecules, and to manipulate their internal states as a means of creating entangled states between molecules. The specific work described in this thesis, to explore the molecular structure of these molecules through laser spectroscopy, is an essential component of this larger programmatic goal.

Heteronuclear molecules possess an important tunable degree of freedom that makes them an appealing and fruitful system to study: in the ground electronic state, they possess a nonzero electric dipole moment that can be manipulated by external fields. This characteristic immediately opens several avenues to utilizing the dipole moment, such as novel implementations of quantum computation schemes (discussed later), controlling ultracold chemical reactions [1], realization of quantum many-body systems [16, 17], and others. If the heteronuclear molecules are in the absolute rotational-vibrational-electronic, or rovibronic, ground state, they are in the lowest possible energy state (ignoring hyperfine energy). From an ultracold chemistry point of view, molecules in the rovibronic state are an ideal starting point to study chemical reactions that also involve dipolar collisions. Recent experiments [3] in ground state KRb have manipulated dipole-dipole interactions to control chemical reaction rates in an external electric field. Similarly, the rovibronic ground state is suitable for schemes involving quantum computation because decoherence effects due to interactions with the environment are diminished.

While ultracold molecules in the ground rovibronic state are an excellent system to probe, creating such molecules is a different challenge altogether. Whereas atoms can be laser cooled quite easily, the rich internal structure of molecules makes it incredibly challenging to cool molecules to ultracold temperatures. Therefore, to create ultracold molecules, we resort to first cooling the constituent atoms and creating ultracold molecules from these ultracold atoms. This process is known as photoassociation (PA) and will be introduced in more detail later in this chapter.

Having provided motivation for creating and studying ultracold heteronuclear molecules, we next present a brief review of early research in light-matter interactions that ultimately led to the creation of ultracold molecules.

1.2 Brief review of ultracold atoms and molecules

At room temperature, chemical reactions that occur between two constituent atom species create stable, deeply bound molecules with electronic, vibrational and rotational degrees of freedom. Interaction between atoms and light that is resonant between the scattering state of atoms (free) and a molecular electronic state (bound) can also create molecules. An attempt to investigate this interaction between colliding atoms and light was undertaken in the early days of high-powered CO_2 lasers [18]. But researchers quickly realized that rather than helping to control interactions between particles, the laser light was a heating mechanism that rendered ineffective the optical manipulation of particle interactions.

Nevertheless, there were early examples of free-to-bound transitions in alkali thermal vapor [19] and more recent attempts at the same (Refs. 25-28 from [20]. Also refs 5-8 in [21]). The common feature among these findings was a broad absorption profile with a width of several nm due to the large initial kinetic energy of colliding particles in the thermal vapor. It was also observed that the colliding particles possessed substantial thermal motion that limited interactions with the light field [18].

In contrast to free-bound transitions in thermal vapor, ultracold atoms offer a significantly different – and much more favorable – environment for light-matter interactions. In this thesis, ultracold systems imply temperatures of 1 mK or less, where, unlike in thermal vapor, Doppler broadening is reduced to less than the natural linewidth of atomic transitions, enabling very high resolution spectroscopy to be performed. Laser cooling techniques and lasers with narrow linewidths of hundreds of kHz allow vibrational, rotational and hyperfine transitions to be easily resolved for ultracold systems. Free-bound light-assisted transitions in ultracold systems – known as photoassociation (PA) – also probe a different region of the potential energy curves. Whereas particle interactions in thermal vapor occur at short internuclear separation ($< 20a_0$), and hence deeply bound rovibrational levels, two ultracold atoms undergoing PA do so at large ($> 20a_0$) internuclear spacing and create very weakly bound molecules, close to the dissociation energy of the excited electronic state.

1.2.1 Progress in homo- and hetero-nuclear molecule formation

Giant strides made in the field of atom cooling and trapping in the 1980s heralded the study of ultracold atoms and molecules [22, 23, 24, 25, 26]. Researchers demonstrated the use of lasers to

translationally cool atoms, and trap them in a spatially varying magnetic field, giving rise to magneto-optical traps (MOTs). This work laid the foundation for studies of ultracold collisions and the interaction of trapped atoms with lasers to create ultracold molecules. The pioneering work of these early 'atom trappers' and their breakthrough techniques have been recognized with the Nobel Prize in Physics.

The first experiments on PA spectroscopy in the latter half of the 1980s and 1990s were conducted in ultracold homonuclear species. A few years after the theoretical framework for free-bound transitions in ultracold Na was presented by Thorsheim et.al. [27], PA spectroscopy of Rb_2, Li_2, Na_2, K_2, and Cs_2 was performed, detecting free-bound transitions by both trap-loss measurements and multiphoton ionization (these detection techniques will be discussed later). Since these early days, numerous groups around the world have created ultracold atoms and performed spectroscopic studies, among other research topics. Here, we highlight some of the early pioneering work that paved the way for explosive growth and exciting research on ultracold molecules.

D. J. Heinzen's group at the University of Texas, Austin trapped Rb atoms in an optical dipole trap and performed PA spectroscopy to bound Rb_2 vibrational levels with a binding energy of almost 1000 cm^{-1} by scanning the frequency of the dipole trap laser [28, 29]. For PA spectroscopy below the Rb(5s) + Rb($5p_{3/2}$) asymptote, they observed the presence of a 'pure long-range' electronic state with an inner turning point > $25a_0$, compared to inner turning points of ~$10a_0$ or less for most electronic states.

PA spectra of K_2 were generated in Stwalley's group at the University of Connecticut [30, 31]. Instead of a tunable dipole trap, the potassium atoms were confined in a MOT, and a separate tunable PA laser produced highly excited K_2 molecules. PA resonances were detected by a decrease in MOT fluorescence when on resonance. In this way, the Connecticut group identified lines belonging to three different electronic states.

PA spectroscopy of $^6Li_2$ and $^7Li_2$ was performed at Rice University in Hulet's group. Using fluorescence detection, Abraham et.al. [32] detected vibrational levels belonging to excited singlet and triplet electronic states, and the binding energies of these levels. At the ultracold temperatures afforded by the MOT, they also resolved the hyperfine structure of the PA lines.

Ultracold Na_2 molecules were created at NIST, where PA spectroscopy was undertaken to complement double-resonance spectroscopy and laser induced fluorescence [33].

A different detection technique was used by Pillet's group at Laboratoire Aime Cotton in Orsay, France for PA spectroscopy of Cs_2 molecules [34]. They used ionization detection to detect PA molecules that decayed to vibrational levels of the triplet ground state. In addition, measurements made to determine the temperature of the molecular cloud revealed that the temperature of the Cs_2 molecules was ~300 μK.

With the success of PA in homonuclear systems, researchers started working towards PA of heteronuclear species, such as KRb [35], RbCs [36], LiCs [37], NaCs [38] and KLi [39]. The experimental details for dual species PA are more involved than for single species PA, not least because (depending on the two alkali species of interest) the apparatus may require separate sets of light sources and optics, not to mention different atom sources. It is also challenging to optimize the number and density of both species of trapped atoms. Since molecules are produced via light-mediated interatomic collisions, the spatial overlap of the two trapped atom clouds needs to be very well adjusted, which is not always a straightforward task. Once overlapped, however, another potential issue arises: interspecies collisions between the trapped atoms cause loss of atoms from the trap and reduce the efficiency of molecule formation. During our work with the dual species Li-Rb MOT, we have encountered these (and more) challenges, and have iteratively improved the system, and hence the quality of our data acquisition. Details of our experimental setup will be discussed in the next chapter.

1.2.2 Applications of ultracold heteronuclear molecules

The payoff for working with two atomic species is that unlike homonuclear molecules, ultracold heteronuclear molecules possess a permanent dipole moment in the ground electronic state. In 2002, DeMille [4] proposed a novel scheme for quantum computation that relied on the dipole-dipole interaction of heteronuclear molecules. Starting with a dual-species MOT, PA is performed to create ultracold heteronuclear molecules. The molecules are transferred to a one-dimensional optical lattice formed by the standing wave interference pattern of a laser beam. The polar molecules occupy lattice sites spaced by $\lambda/2$, where λ is the optical lattice laser wavelength. An external electric field with a field gradient along the length of the optical lattice creates a non-zero electric dipole moment of the molecules. In essence, the strength of the spatially varying electric field tunes the interaction between nearest neighbor polar molecules, which can be treated as

quantum bits, or qubits that are oriented up or down with respect to the electric field, as shown in Figure 1.1. With demonstrated production of ultracold heteronuclear molecules in the lowest rovibrational states of the ground electronic state [40], this proposal promises an all-optical quantum logic gate operation.

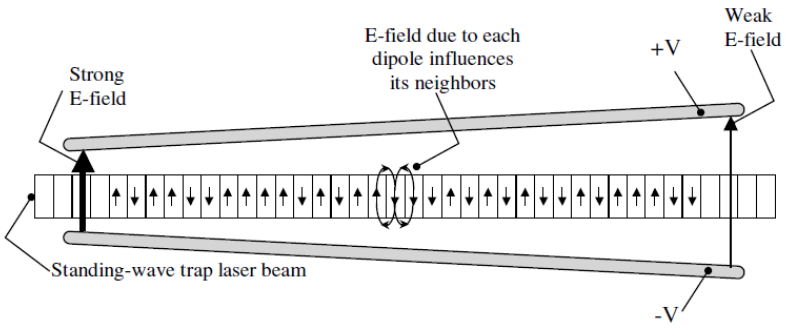

Figure 1. Schematic outline of the quantum computation scheme proposed by DeMille [4]. The small arrows in each rectangular section of the optical lattice represent the orientation of the permanent dipole of polar molecules.

Coherent control has been widely used to study interference between different transition pathways in atomic and molecular systems by using all-optical means. In ultracold systems, this idea can be applied in the PA step as follows: two light fields that are phase locked to each other photoassociate ultracold atoms to an excited electronic state. The first light source employs a conventional one-photon PA resonance, while the second source is two-photon resonant with a free-bound transition. The two PA pathways create molecules in different rotational states, and because the light fields are phase-coherent, they form PA molecules in rotational superposition states. The superposition can be detected by a standard time-of-flight ion imaging setup. More details of this application of polar molecules will be presented later in this thesis.

Spectroscopy of ultracold molecules using PA is also an important area of research. PA complements the spectroscopic picture of excited molecular electronic states. Conventional spectroscopy can access moderate- to deeply-bound vibrational levels, but information on near-dissociation levels is washed out due to the large initial thermal distribution of the sample under study [20]. PA offers a very high resolution spectroscopy tool to glean information about these near dissociation levels of ultracold molecules [18, 41]. Unlike bound-bound spectroscopy that mainly covers short internuclear spacing (See, for example [42] and [43]), PA favors long-range

free-bound transitions, primarily due to good overlap between the initial scattering-state and final molecular wavefunction. Recently, however, evidence has begun to emerge of short-range PA, with ultracold Rb_2 molecules created in excited state vibrational levels above the corresponding molecular asymptote [44], and molecules formed in the $A^1\Sigma_u^+$ state with PA light at 1071 nm (unlike conventional Rb_2 PA at ~780-800 nm) [45].

The vast potential of heteronuclear polar molecules has guided our studies of ultracold LiRb molecules, one of the least studied alkali heteronuclear species. This thesis will present spectroscopic studies of ground and excited electronic states of LiRb using ionization spectroscopy. Our goal in exploring LiRb energy levels is to gain a better understanding of the molecular structure, with the ultimate aim of searching for convenient pathways to transfer these molecules into the ground rovibronic state. This transfer to the least energetic states will create an ideal starting point for studying dipole-dipole interaction of LiRb molecules, and also for creating and manipulating a coherent superposition of rotational states with long decoherence times.

The remainder of this chapter reviews background information needed to understand free-bound and bound-bound transitions (for a rigorous background on molecular spectroscopy, see [46] and [47]). We introduce the framework of molecular potential energy curves, and the different regimes that correspond to deep, strongly bound states, and long-range behavior close to the dissociation energy. Spectroscopic notation and selection rules that apply to different interaction regions are defined. Experimentally, our starting point is the cooling and trapping of atoms. Therefore, to complete the chapter, we present the principles governing the light-matter interaction that are crucial to producing ultracold atoms, and eventually ultracold molecules.

1.3 Background on molecular spectroscopy

1.3.1 Born-Oppenheimer approximation

The non-relativistic Hamiltonian for a diatomic molecule can be written as [48, 49]:

$$H = T_N(\boldsymbol{R}) + T_{el}(\boldsymbol{r}) + V_{elN}(\boldsymbol{r}, \boldsymbol{R}) + V_{NN}(\boldsymbol{R}) + V_{elel}(\boldsymbol{r}) \tag{1.1}$$

where the subscript *el* represents electrons and *N* represents the nuclei. The first two terms are the kinetic energies of the nuclei and electrons, respectively, and the other three represent electrostatic interactions. $\boldsymbol{R}$ and $\boldsymbol{r}$ are the coordinates of the nuclear and electronic coordinates,

respectively. Due to the *el-N* interaction term the Hamiltonian cannot be separated into electronic and nuclear parts. However, electrons move much faster than nuclei, which allows us to use the Born-Oppenheimer approximation and treat electronic motion separately from nuclear motion. With this approximation, the overall molecular wavefunction $\Psi(\boldsymbol{r}, \boldsymbol{R})$ can be written with separate electronic and nuclear wavefunctions as:

$$|\Psi\rangle = |\psi_{el}\rangle\,|\psi_{N}\rangle \tag{1.2}$$

With the electronic and nuclear motion decoupled, we can look at the variation of the potential energy as a function of internuclear spacing and so construct a potential energy curve (PEC). A set of PECs for LiRb are shown in Figure 1.2. Two features are common to all PECs. As $R\rightarrow 0$, the potential energy increases sharply, indicating repulsion. At the other extreme, as $R\rightarrow\infty$, the exchange interactions vanish and the molecule separates into the constituent atoms. Each PEC will also have classical turning points where the molecule preferentially spends more time, which corresponds to a larger probability density.

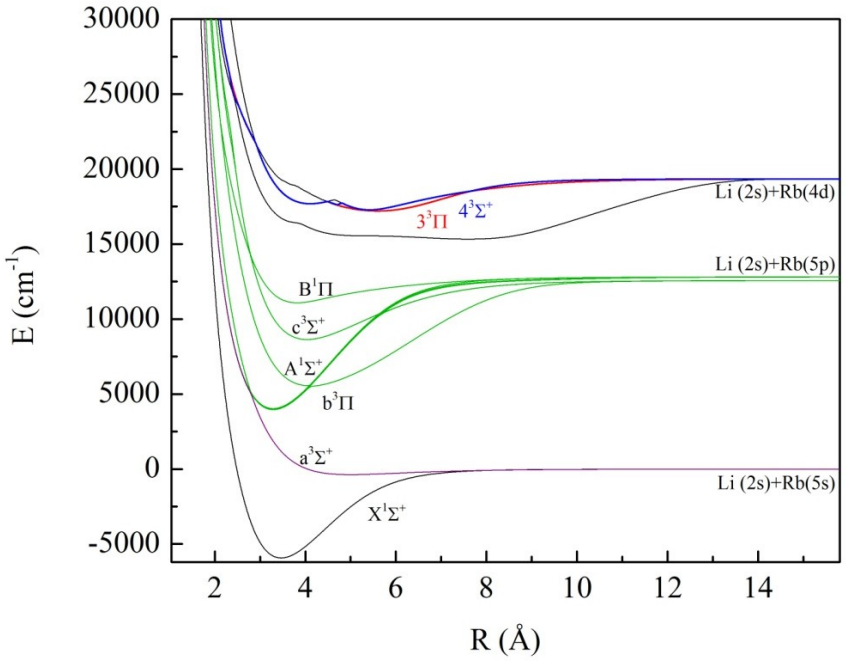

Figure 1.2. A set of potential energy curves (PECs) for $^{7}Li^{85}Rb$, generated from *ab initio* calculations by Korek et.al. [50]. Note that all the curves at long range are asymptotic to a Li or Rb atomic level. We will discuss later the curves relevant to PA and excited state ionization spectroscopy.

1.3.2 Term energies

In addition to electronic motion, molecules can also vibrate and rotate. For a given PEC and ignoring rotational motion, the vibrational levels can be approximated to first order by the equally spaced energy eigenvalues of a harmonic oscillator potential. However, it quickly becomes apparent that the vibrational energy levels for real diatomic molecules are not equally spaced, and we need to consider anharmonic terms that better model the vibrational energy. Thus we can write the vibrational term energies as:

$$G(v) = \omega_e \left(v + \frac{1}{2}\right) - \omega_e\chi_e\left(v + \frac{1}{2}\right)^2 + \ldots \tag{1.3}$$

where ω_e is the vibrational constant and $\omega_e\chi_e$ is the anharmonic constant, both given in units of cm^{-1} ($1\ cm^{-1} \approx 30$ GHz). The subscript denotes the value of the constants at the equilibrium internuclear separation.

The rotational energy of a diatomic molecule will depend on the rotational angular momentum J and the rotational constant $B = h/8\pi^2\mu R_e^2$ (where μ is the reduced mass, and R_e is the internuclear separation at equilibrium) to give $BJ(J + 1)$. In writing this, we have not included the effect of centrifugal distortion on the molecule.

Treating the rotational and vibrational energies separately from each other is a reasonable starting point, but molecules can vibrate and rotate simultaneously. With this modification, along with the addition of centrifugal effects, the rotational term energy becomes:

$$F_v(J) = B_v\left[J(J + 1) - \Lambda^2\right] - D_v[J(J + 1) - \Lambda]^2 \tag{1.4}$$

where B_v is the rotational constant and D_v is the centrifugal distortion constant, and Λ is the projection of the orbital angular momentum on the internuclear axis (more on this later). The subscripts denote the dependence of the rotational and centrifugal distortion constants on the vibrational level under consideration.

Bringing together the electronic, vibrational and rotational terms, the energy of a molecule in a rovibronic state can be written as:

$$E(v, J) = T + F_v(J) + G(v) \tag{1.5}$$

Here, T is the energy of the minimum of a PEC above the bottom of the lowest electronic state.

1.3.3 Long-range interaction

As mentioned earlier, as R becomes large (> $20a_0$ [41]), a PEC will asymptotically approach an atomic energy level, and the molecular interaction is better described as that between two separated atoms. The potential energy as a function of internuclear separation is modeled as:

$$V(R) = D_e + \sum_n \frac{C_n}{R^n} \tag{1.6}$$

D_e is the dissociation energy, and C_n are dispersion coefficients. The dominant multipole term will depend on the PEC being considered. Table 2.1 lists the types of interactions for different powers of R. Homonuclear diatomic molecules interact via the long-range R^{-6} van der Waals interaction in the ground state, and via induced dipole-dipole (R^{-3}) interactions in excited states. For heteronuclear molecules, both ground and excited state potentials go as R^{-6}. As we will see later, this difference has an effect on the spectroscopy of homo- and heteronuclear molecules.

Table 1.1. The different types of long-range interactions, based on the R^{-n} dependence of the interaction potential. For PA of heteronuclear molecules $n = 6$ for the ground and excited electronic states.

n	Type of interaction
3	Dipole-Dipole
4	Dipole-Quadrupole
5	Quadrupole-Quadrupole
6	Induced Dipole-Dipole (van der Waals)

1.3.4 Spin-orbit interaction

So far in our molecular framework, we have not considered relativistic effects, which become important and non-negligible at ultracold temperatures. Of these, the spin-orbit interaction is the strongest, and manifests itself at long range as molecular PECs asymptotically approach the dissociation energy. Consider the first excited state LiRb PEC shown in Figure 1.2. The Li(2s) +

Rb(5p) asymptote is split into the Li(2s) + Rb($5p_{1/2}$) and Li(2s) + Rb($5p_{3/2}$) levels, where the energy spacing is ~230 cm^{-1}.

The relative interaction strengths among the various relativistic (spin-orbit) and non-relativistic (electron exchange) components varies over the PEC. In order to help understand how the different angular momenta and rotation of the molecule couple to one another, we use Hund's representation as described below. We only mention cases (a) and (c), which are relevant to our work. For the complete set of Hund's cases see, for example, Herzberg [46].

Hund's case (a)

In the region of small internuclear separation, the angular momentum coupling is described by Hund's case (a). As shown in Figure 1.3(a) the orbital angular momentum L (= l_1 + l_2. The subscripts denote the two atoms) and spin angular momentum S (= s_1 + s_2) separately couple more strongly to the internuclear axis than to each other. Λ, the projection of L on the internuclear axis, and Σ, the projection of S on the internuclear axis, are both good quantum numbers, and can be used to label case (a) molecules:

$$^{2S+1}\Lambda^{\pm} \tag{1.7}$$

The ± superscript denotes reflection symmetry of the spatial component of the electronic wavefunction in a plane containing the internuclear axis. $\Lambda = 0,1,2,\ldots$ are labeled as Σ, Π, Δ,…, respectively. For example, the ground electronic state of heteronuclear alkali molecules is labeled as $^1\Sigma^+$ (Note: Σ is used to represent the Λ = 0 state, as well as the projection of S onto the internuclear axis. Context should make the distinction clear). The $\pm$ depiction is omitted for $\Lambda \neq 0$ states because these states are degenerate.

Hund's case (c)

In contrast to case (a), at the large internuclear distances where spin-orbit effects become more prominent, the coupling between L and S becomes stronger than the individual coupling to the internuclear axis. In this regime $\Omega = |\Lambda + \Sigma|$ is a good quantum number, and case (c) states are labeled as:

$$\Omega^{\pm} \tag{1.8}$$

Unlike for Hund (a) states, the $\pm$ superscript for Hund (c) denotes reflection symmetry of the total electron wavefunction through a plane containing the internuclear axis. Hund (c) coupling is shown in Figure 1.3(b).

To complete the discussion of Hund's cases, we mention an additional symmetry constraint that arises for homonuclear molecules only. If the wavefunction is symmetric (antisymmetric) upon inversion of the electronic coordinates about the molecular center of mass, the molecule has gerade (ungerade) symmetry. For both Hund (a) and (c), this information is displayed as a g/u subscript. Since this additional restriction does not apply to heteronuclear molecules, the number of allowed transitions and the states accessible by one-photon electric dipole-allowed transitions is different compared to homonuclear molecules.

1.3.5 Electronic state labeling

A set of PECs for a heteronuclear molecule will have several Σ, Π, Δ, etc. states, and it is important to clearly distinguish among them. The following labeling convention is used for heteronuclear diatomic alkali molecules: the lowest electronic energy state is written as $X\ ^1\Sigma^+$. The lowest triplet state is the $a^3\Sigma^+$. In LiRb, both these states are asymptotic to the Li(2s) + Rb(5s) level. The lowest $^3\Pi$ is the $b^3\Pi$ state. After the $X\ ^1\Sigma^+$, the next energetically higher $^1\Sigma^+$ state is the $A^1\Sigma^+$. Finally, the lowest $^1\Pi$ level is labeled as $B^1\Pi$. In literature these may also be labeled as the *X*, *a*, *b*, *A*, and B states, respectively.

Hund's case (c) states have a different labeling convention. These are labeled as numbers in order of increasing energy of the atomic asymptotes. From Figure 1.2 and the discussion above, we can see that, at long range, both the $X\ ^1\Sigma^+$ and the $a^3\Sigma^+$ states are asymptotic to the Li(2s) + Rb(5s) asymptote. The *X* state correlates to the $1(0^+)$ level. Similarly, the *a* state correlates to the $1(0^-)$ and the 1(1) levels. The next 0^+ level is the $2(0^+)$, and so on. The spin-orbit coupling at long-range can result in more than one Hund (c) state correlating to the same Hund (a) level. Table 1.2 lists the Hund's case (a) states and the corresponding case (c) states asymptotic to the first two LiRb atomic levels.

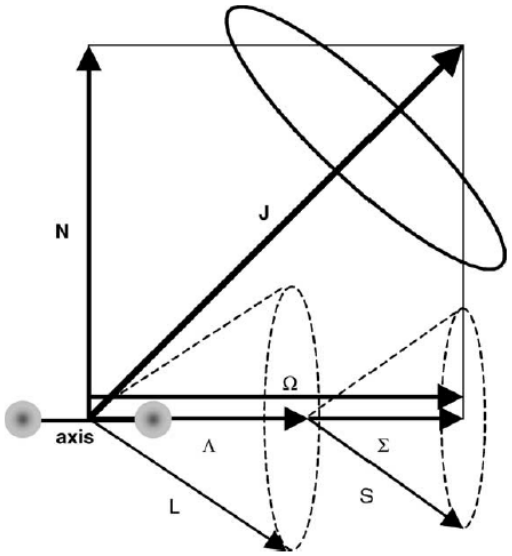

(a)

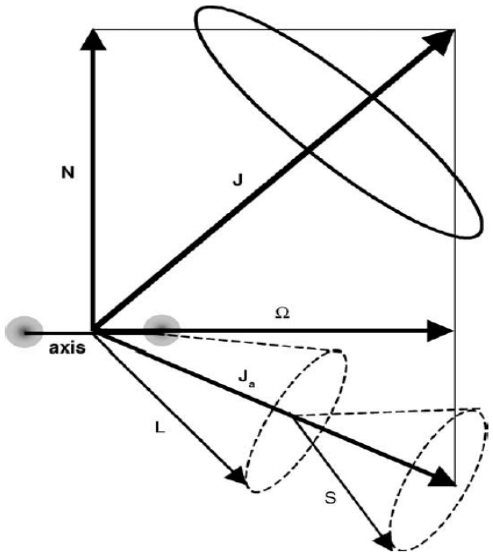

(b)

Figure 1.3. Vector representation of (a) Hund's case (a) and (b) Hund's case (c). **N** is the angular momentum of nuclear rotation. Adapted from [51].

Table 1.2. Electronic state correlation between Hund (a) and Hund (c) potentials. The fine structure splitting of the Li(2s) + Rb(5p) level is not listed here.

Hund's case (a)	Hund's case (c)
Li(2S)+Rb(5S)	
$X^1\Sigma^+$	1(0+)
$a^3\Sigma^+$	1(0-) 1(1)
Li(2S)+Rb(5P)	
$A^1\Sigma^+$	2(0+)
$c^3\Sigma^+$	2(0-) 2(1)
$b^3\Pi$	3(0+) 3(0-) 3(1) 1(2)
$B^1\Pi$	4(1)

1.3.6 Selection rules for allowed transitions

Before embarking on studies of atomic and molecular transitions, we need to know if a particular transition is permitted, given the (one-photon) light field coupling the initial to the final rovibronic state. This information is contained in the transition matrix element:

$$\boldsymbol{M}_{if} = \langle \Psi_f | \, \boldsymbol{d} \, | \Psi_i \rangle \tag{1.9}$$

where Ψ_i and Ψ_f are the initial and final state wavefunctions, and $\boldsymbol{d}$ is the dipole operator. Recall that the molecular wavefunction can be separated into an electronic and nuclear wavefunction using the Born-Oppenheimer approximation, and the nuclear wavefunction can be further separated into vibrational and rotational components to give:

$$\Psi = \psi_{el} \, \psi_{vib} \, \psi_{rot} \tag{1.10}$$

The vibrational wavefunction does not affect the electric dipole matrix element, and can be factored out:

$$\Psi = \left\langle \psi_{el,f}\psi_{rot,f} \right| \boldsymbol{d} \left| \psi_{el,i}\psi_{rot,i} \right\rangle \left\langle \psi_{vib,f} \middle| \psi_{vib,i} \right\rangle \tag{1.11}$$

The dipole matrix element above determines the electric dipole selection rules.

Regardless of the specific Hund's case the selection rule $\Delta J = 0,\pm 1$, except $J' = 0 \nleftrightarrow \mathrm{J} = 0$, is rigorously enforced, where J is the total angular momentum (excluding nuclear spin). The complete list of selection rules for Hund's cases (a) and (c) are listed in Table 1.3.

Table 1.3. One-photon electric dipole-allowed transitions in molecules.

General selection rule	
$\Delta J = 0, \pm 1; J' = 0 \nleftrightarrow J = 0$	
$J \geq \Omega$	
Hund (a)	Hund (c)
$\Delta\Lambda = 0, \pm 1$	$\Delta\Omega = 0, \pm 1$
$\Sigma^+ \leftrightarrow \Sigma^+, \Sigma^- \leftrightarrow \Sigma^-, \Sigma^+ \nleftrightarrow \Sigma^-$	$0^+ \leftrightarrow 0^+, 0^- \leftrightarrow 0^-, 0^+ \nleftrightarrow 0^-$
$\Delta\Sigma = 0$	

1.3.7 Franck-Condon Principle

Whereas the dipole matrix element in Eq.(1.11) governs the selection rules, the overlap between the initial and final state wavefunction determines the strength of a particular transition. This information is conveyed via the Franck-Condon Factor (FCF):

$$\mathrm{FCF} = \left| \left\langle \psi_{vib,f} \middle| \psi_{vib,i} \right\rangle \right|^2 \tag{1.12}$$

As the amplitude of the wavefunction is largest near the classical turning points, a large FCF results when, for example, the outer turning points of the initial and final states lie at the same internuclear separation.

The Franck-Condon principle assumes that in the time scale of electronic transitions, the nuclei remain stationary. Alternatively, electronic transitions are said to be 'vertical' transitions. Figure 1.4 shows a schematic of wavefunction overlap between a ground and excited electronic state.

Having presented an overview of important aspects of molecular spectroscopy, we next discuss electronic states of LiRb molecules.

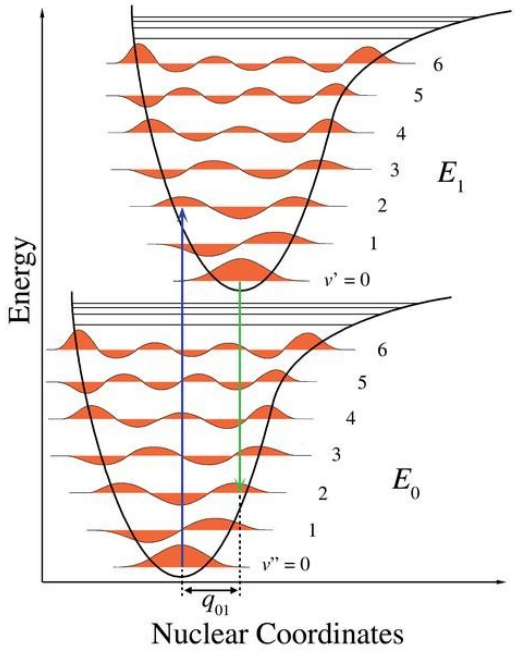

Figure 1.4. Schematic representation of overlap between ground and excited state vibrational levels. The degree of overlap, which in turn determines the strength of the transition, is given by the Franck-Condon factor. Figure adapted from [52].

1.4 Electronic states of LiRb

1.4.1 $X\,^1\Sigma^+$

Until recently, sparse experimental data were available for LiRb. Our interest in the molecule is primarily due to its large permanent dipole moment among diatomic alkali molecules (4.1 Debye [53]), which makes LiRb a suitable system for quantum computing schemes that rely on controlling the dipole moment of molecular qubits.

Ab initio calculations of the LiRb PECs have been performed by Igel-Mann et.al. [54] and Korek et.al. ([55] and [50]; see Figure 1.2 for LiRb PECs based on calculations from ref. [50]), but very limited spectroscopic studies have been reported. Ivanova et.al. [42] used laser-induced

fluorescence (LIF) spectroscopy in a heat pipe to identify the first 45 vibrational levels of the $^{7}Li^{85}Rb$ *X* state. These conventional high temperature spectroscopic techniques can produce high resolution spectra of deeply bound rovibrational levels for both ground and excited electronic states, but the near-dissociation levels still remain out of reach. Our LiRb PA studies should help to complete the energy level picture of the *X* state.

1.4.2 $a^3\Sigma^+$

Ivanova et.al. also reported limited and preliminary data on the *a* state, but no complete study for this state has been performed as of the writing of this thesis. *Ab initio* calculations are the best source of information available on this state. As reported later in this thesis, we have identified near-dissociation levels of the *a* state via resonantly enhance multiphoton ionization (REMPI).

1.4.3 Excited electronic states

Prior to the ultracold experiments in our lab, we conducted spectroscopic studies of hot LiRb molecules that revealed useful information about the ground *X* and excited *B* states. We mapped out the first 21 vibrational levels of the B state using fluorescence excitation spectroscopy (FES) [43]. Briefly, the LiRb vapor produced in a heat pipe is excited using a tunable cw dye laser. Fluorescence produced by the molecules decaying to the ground state is collected and analyzed with a high resolution monochromator. For FES studies, as the dye laser is tuned, the monochromator is set to detect fluorescence as an excited molecular state decays radiatively to a specific ground rovibrational state. In this way we are able to map out the excited $B^1\Pi$ state. Details of the heat-pipe spectroscopy measurements can be found in [56]. In 2013, Ivanova et.al. reported spectra for the $B^1\Pi$ and $D^1\Pi$ states of LiRb [57].

These studies started to reveal information about LiRb, but all of the accessible transitions were to deeply bound levels of the excited electronic states. Our current work on PA spectroscopy started to probe the least deeply bound levels at large internuclear spacing. The next section outlines the PA process.

1.5 Photoassociation (PA)

As mentioned earlier, ultracold molecules are formed when the PA laser frequency, ν_{PA}, is resonant with a bound molecular level. The overlap between the ground- and excited-state

wavefunctions is large at large internuclear spacing, leading to molecule formation in high-lying vibrational states close to the atomic asymptote. These molecules can decay via either a bound-to-bound transition or a bound-free transition. In the first instance, the excited molecule decays to rovibrational levels of ground (singlet or triplet) electronic states and forms a stable molecule. If the molecule undergoes a bound-free transition via spontaneous decay, it breaks apart into the constituent atoms, which take away the excess kinetic energy released in the decay process. The kinetic energy can be greater than the MOT trap depth and the atoms escape the trapping region. The photoassociated molecules are nonresonant with the cycling transition and are not confined to the trapping region either. Both of these decay channels cause a reduction in the number of trapped atoms, with the corresponding decrease in fluorescence from spontaneous decay.

As we tune the frequency of the PA laser, we can observe changes in the MOT fluorescence level as the laser goes through free-bound transitions and produce 'trap-loss' spectra. These spectra provide information about the spacing of high-lying vibrational levels of the photoassociating state. As we keep scanning the PA laser farther from the dissociation level (red-detuning), the Franck-Condon factor between the ground-state scattering wavefunction and the excited-state bound wavefunction decreases, and is reflected in the strength of the trap-loss resonances.

Trap-loss can tell us whether a free-bound transition has occurred, but gives no information about the decay path of the excited state molecules. Resonantly enhanced multiphoton ionization (REMPI) fills this gap by probing PA molecules that decay to the ground singlet or triplet electronic states. Most PA REMPI schemes use two identical photons from a pulsed laser. The ion signal is maximized by tuning the laser to be resonant with an intermediate state (the two-photon ionization scheme is also referred to as resonantly enhanced two-photon ionization or RE2PI). For alkali diatomic molecules, pulsed dye lasers operating in the visible to near-IR wavelength range can easily ionize ground state molecules.

Whereas trap-loss spectra only contain information about the PA state, analysis of REMPI spectra is complicated because of the ionization pathway that includes the initial ground state as well as the intermediate ionizing state. The advantage of ionization spectra is that not only can we detect if the excited state molecule decays to the ground state, but also the specific vibronic level that the molecule decays to. In this way we can determine the vibrational structure of the intermediate ionizing state, as well as the structure of the ground state. LiRb REMPI spectra are discussed in Chapter 4.

The first step towards creating ultracold LiRb molecules is to produce a sample of ultracold Li and Rb atoms. In the next section, we discuss the principles behind optical cooling and trapping that lead to Li and Rb atoms in a magneto-optical trap (MOT).

1.6 MOT principles

1.6.1 Cooling and trapping of atoms

To create a sample of atoms at sub-milli-Kelvin temperatures, we make use of atom-photon collisions to transfer momentum from the atoms and reduce the translational motion, which in turn decreases their temperature. If we think about a few photons scattering off of atoms, they do not significantly affect the momentum of the atoms. However, for large scattering rates (millions of photon scattering events per second), the atoms decelerate to kinetic energies equivalent to a temperature of a milli-Kelvin or less. A useful (though limited) classical analogy to describe this situation is slowing a bowling ball by firing a stream of ping pong balls at it. Spontaneous emission, which must occur after each absorption process, occurs randomly in all directions, and so on average there is no net gain of momentum by the atoms. The application of magnetic fields to spatially trap the atoms completes the cooling and trapping process to produce a MOT.

At this point we may ask: instead of cooling atoms first to form ultracold molecules, can we instead form the molecules first and then cool them using cooling and trapping techniques similar to the ones used for atoms? Optical cooling works for atoms because of cycling transitions between the ground and excited hyperfine states which ensure the atoms keep losing momentum to the cooling light by undergoing repeated absorption and stimulated emission between the same initial and final states that are resonant with the cooling light. Optical cooling of molecules is an extremely challenging task because they possess vibrational, rotational and hyperfine degrees of freedom. These numerous decay channels would require an impractical number of repump frequencies for efficient cooling. Nevertheless, recent developments in optical cooling of molecules have produced good results [58], with the caveat that these approaches work for molecules that have favorable decay rates to very few ground state levels. Thus, as of now, the schemes to cool and trap molecules are not as widely applicable as those for atoms.

A rigorous treatment of MOT principles is presented in [59]. Here we mention the salient features of laser cooling and trapping.

1.6.2 Optical Cooling

In the general picture of optical cooling described earlier, we assumed that the photon frequency is always resonant with an atomic transition. This is obviously not the case, since the moving atoms see light that is Doppler shifted above or below resonance by a frequency $\boldsymbol{k} \cdot \boldsymbol{v}$, where $\boldsymbol{v}$ is the atomic velocity vector and $\boldsymbol{k}$ is the photon wavevector. Consider a one-dimensional picture in which atoms are moving towards the left as shown in Figure 1.5 and the laser frequency ω_L is red-detuned from the resonant frequency ω_0. Since the atoms are moving towards the laser beam, they will see blue-shifted laser frequency and be resonant with the light when $v_{\|} = (\omega_0 - \omega_L)/k$, where $v_{\|}$ is the component of $\boldsymbol{v}$ along $\boldsymbol{k}$. They will undergo a transition to an excited state and a short time later (tens of ns) decay back to the ground state through spontaneous emission and slow down via momentum transfer. Atoms moving in the opposite direction see red-shifted photons that are out of resonance and are unaffected by the photons. In steady state the cooling process is balanced by the heating effect due to spontaneous emission in random directions. At this point the minimum temperature of the atoms is $T_D = \hbar\Gamma/2k_B$. T_D is called the Doppler temperature, and Γ is the excited state decay rate, or the transition linewidth. For example, ^{85}Rb with a transition linewidth $\Gamma = 2\pi \times 5.6$ MHz has a Doppler temperature of $T_D = 140$ μK.

As it turns out, however, atoms can be cooled to below the Doppler limit. Our earlier model did not predict this sub-Doppler cooling because it was based on a simplified, one dimensional, two-level system that ignored magnetic sublevels. In the refined energy level picture, the ground state atoms can be distributed among the various Zeeman sublevels, with the population distribution dependent upon the laser polarization. Metcalf and van der Straten [59] showed that the laser polarization varies along the direction of propagation. This position-dependent polarization gradient acts to redistribute the atomic sublevel population and hence cool them to below the Doppler temperature.

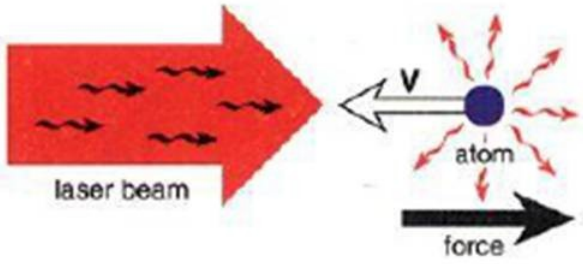

Figure 1.5. Schematic representation of the Doppler cooling force on a moving atom by resonant laser light [60].

1.6.3 Magnetic trapping

By using the three pairs of orthogonal, counter-propagating lasers, we can achieve cooling of atoms, but there is no force that can confine the atoms. This can be achieved by using either electric fields or magnetic fields. Our experimental setup employs the latter approach.

The presence of a magnetic field B causes a Zeeman shift of the energy level E_i:

$$\Delta E_i = -\vec{\mu}_i \cdot \vec{B} = -\mu_B g_F m_F B \tag{1.13}$$

where μ_B is the Bohr magneton, g_F is the Landé g-factor, and m_F is the projection of the total angular momentum F onto the field axis.

To trap the slowed atoms, we need a linearly varying magnetic field that goes through zero at the intersection of the lasers. Using two identical coils with the current flowing in opposite directions – known as an anti-Helmholtz configuration – creates this effect. The coils are set up with their axes parallel to one of the three laser directions, most conveniently the vertical (z-) direction. In combination with the circularly polarized laser light, the Zeeman shift transfers population from one magnetic hyperfine level to another (for right (left) circular polarization, the selection rule for m_F is: $\Delta m_F = +\,(-)1$). Each pair of lasers consists of a right-circularly polarized field (σ^+) and a counter-propagating left-circularly polarized field (σ^-). See Figure 1.6.

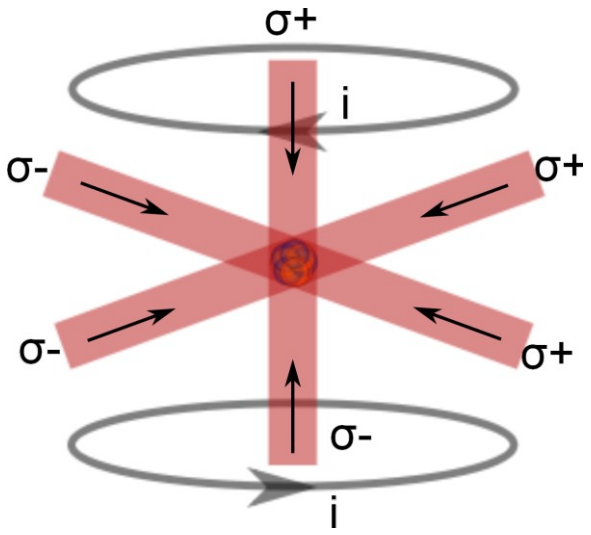

Figure 1.6. Cooling and trapping of atoms using a combination of resonant light (red) and a pair of anti-Helmholtz magnet coils.

Since the magnetic field varies linearly as we move along the *z*-axis, we can qualitatively describe the atomic motion as follows: At $z = 0$ (trap center) the average momentum transfer to the stationary atoms from the *z*-pair of lasers is zero since the photon absorption rates are equal for the two lasers. For $z > 0$, the σ^- laser is more likely to be absorbed because of the Zeeman shift, giving a momentum kick to the absorbing atom in the *-z* direction, and thus towards trap center. The analogous situation arises for atoms at $z < 0$ getting a momentum kick from the σ^+ laser in the *+z* direction, again towards trap center. The atoms are therefore trapped in the harmonic oscillator potential created by the magnetic field. The magnetic trapping scheme is shown in Figure 1.7 for a simplified two level atom with one and three magnetic sublevels in the ground and excited states, respectively.

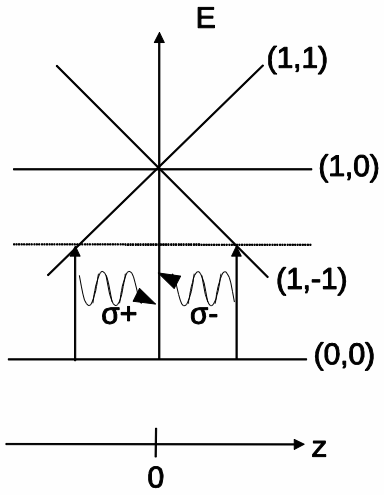

Figure 1.7. Scheme for trapping cooled atoms. The left (σ^+) and right (σ^-) circularly polarized light provides a momentum kick to the atoms and slows them, while the magnetic field creates a trapping potential for spatial confinement. The vertical arrows denote transitions from the ground $F = 0$, $m_F = 0$ state (0, 0) to the excited $F = 1$, $m_F = -1, 0, 1$ states (1, -1), (1, 0) and (1, 1), respectively.

1.7 Conclusion

In this chapter, we have provided motivation for investigating ultracold heteronuclear molecules, in particular LiRb as our choice of system. We have presented background information on molecular spectroscopy to aid in our spectroscopic studies. To create ultracold molecules, we have introduced laser cooling and trapping as the starting point for creating ultracold atoms, and subsequent PA as the mechanism for creating ultracold LiRb molecules.

In the next chapter, we give details of our dual-species MOT apparatus, including means for detecting LiRb molecules.

2. SETUP FOR CREATING AND DETECTING ULTRACOLD LIRB MOLECULES

Table-top experiments in AMO physics require various instruments that include light sources, optical elements, vacuum chambers, electronics, and data acquisition hardware and software. Building such a setup from the ground up is a complex undertaking, and requires substantial time and effort, not only to assemble the different sections of the system but also to troubleshoot and debug problems. It should be noted here that all aspects of the dual species MOT apparatus and detection system described in this chapter have only been possible due to significant teamwork and contributions from Sourav Dutta and John Lorenz, the other two graduate students involved in this project from its initial phases.

Every system comes with its advantages and drawbacks, and our system is no different. Here we give details of our magneto-optical trap (MOT) apparatus, starting with our indispensable sources of coherent radiation.

2.1 Lasers

The light sources used in our lab range from cw semiconductor diode lasers to high peak power pulsed dye lasers. In all, their purpose is i) to create the ultracold atoms, ii) use light-matter interactions to create ultracold molecule, and iii) probe the molecular sample to obtain information about its energy levels and to precisely control the molecular degrees of freedom.

2.1.1 Diode lasers

Diode lasers are a mainstay in AMO experiments for their versatility, durability, ease of use and cost effectiveness. Over the course of this project, we have constructed several diode lasers for different aspects of the experiment. Here we present the operating principles of diode lasers, means of reducing the output frequency linewidth, and frequency stabilization schemes.

2.1.2 External cavity diode lasers

The active medium in a diode laser is a semiconductor chip that emits photons when a current is applied. The output of standalone diode lasers has a range of several nm and is governed by the diode gain profile. As current is applied, the emitted photons bounce back and forth between a highly reflective back facet and a slightly transmissive front facet of the diode chip. Lasing ensues once population inversion is achieved above a threshold current. At this point the bare laser diode has a broad linewidth of hundreds of MHz. For the purposes of creating a MOT or to probe the trapped atoms, we need to narrow the laser linewidth to within ~1 MHz or less of the desired frequency. This can be done by using optical feedback from an external optical element. Diode lasers are highly susceptible to stray reflections that can influence their output characteristics. In many applications, this feedback is a nuisance and has to be minimized, but it is advantageous if the goal is to reduce the laser linewidth.

Both linewidth reduction and the required frequency tuning can be achieved by adding a diffraction grating in the so-called Littrow configuration. Optical feedback is provided by a diffraction grating which, along with the back facet of the diode chip, acts as an external lasing cavity to form an external cavity diode laser (ECDL). The first order diffraction from the grating is fed back to the diode to reduce the linewidth, while the zeroth order is the useable – and tunable – output. The grating angle θ for optical feedback in Littrow is:

$$2d\sin\theta = \lambda \tag{2.1}$$

where d is the grating groove density and λ is the output wavelength. For a 780 nm diode laser and a diffraction grating with a groove density of 1200 lines/mm, the Littrow angle θ is about 45°.

Figure 2.1 illustrates how to think of the optical feedback. The curve labeled ‘medium’ is the gain profile of a 671 nm bare diode (without the external grating). Lasing takes place due to reflections from the front and back facet of the diode chip. The thickness of the chip determines the frequency spacing between adjacent cavity modes, called the free spectral range (FSR) of a cavity:

$$FSR = c/2d \tag{2.2}$$

where d is the cavity length and c is the speed of light. For a typical internal cavity length of 1 mm, the *FSR* is 150 GHz. This is the 'internal cavity' curve in Figure 2.1.

Similar to the internal cavity gain profile, the feedback from the external cavity formed by the grating and diode back facet also has a gain profile, shown as the 'grating feedback' curve. Since the external cavity is much longer compared to the internal cavity (a few cm), the FSR is a few MHz (external cavity modes shown in Figure 2.1). With the optical feedback, we not only stabilize the diode output but also reduce its linewidth to a few MHz, compared to hundreds of MHz for the bare diode. The external cavity mode nearest the maximum of the diode and external cavity gain profiles experiences the lowest round trip losses, and the ECDL preferentially lases in that mode. The vertical line in Figure 2.1 highlights such a lasing mode.

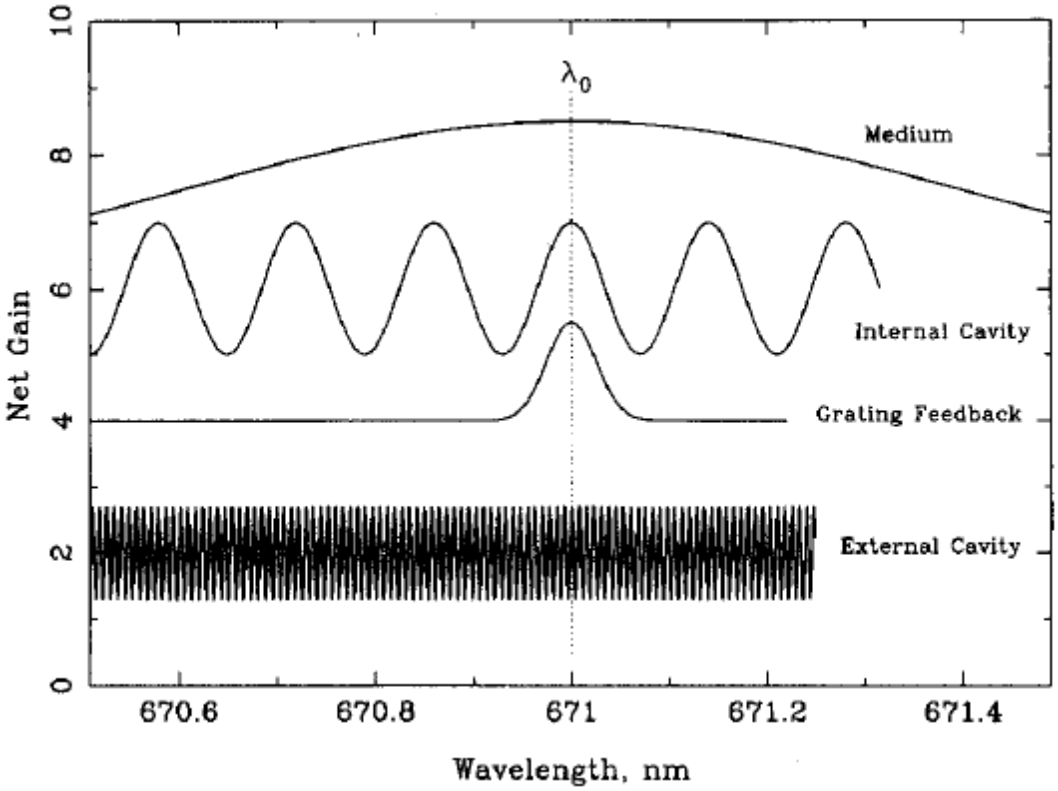

Figure 2.1. ECDL gain curves for a 671 nm diode laser [61]. The curve labeled 'Medium' is the gain curve for the diode chip. 'Internal Cavity' curve shows the mode structure of the cavity set up by the front and back facets of the diode chip. 'External Cavity' shows the numerous lasing modes of the cavity made up of the back facet of the diode chip and the diffraction grating. 'Grating Feedback' shows the gain profile of the external cavity. The ECDL lases on the external cavity mode that has maximum gain near the maximum of the other three gain curves.

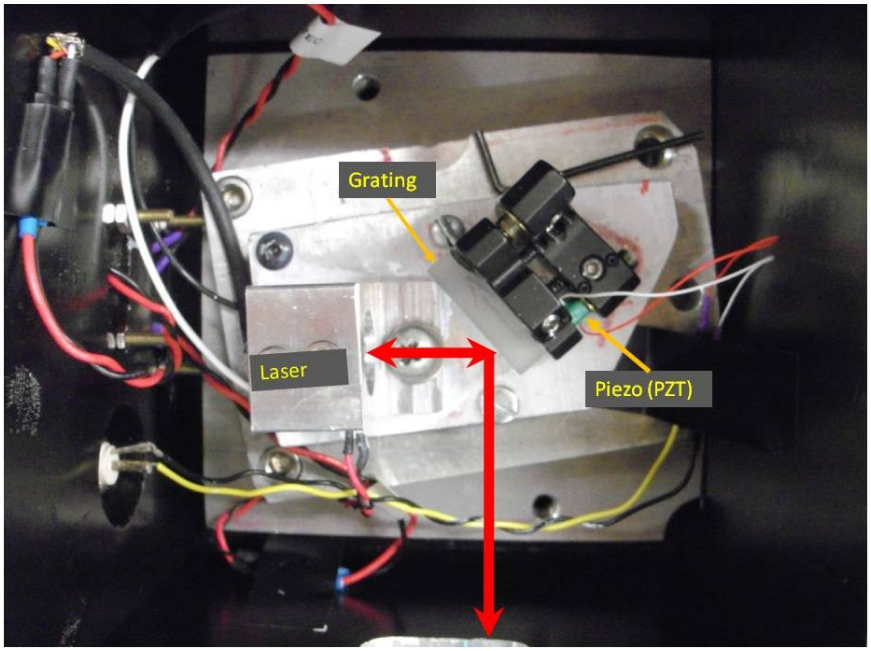

(a)

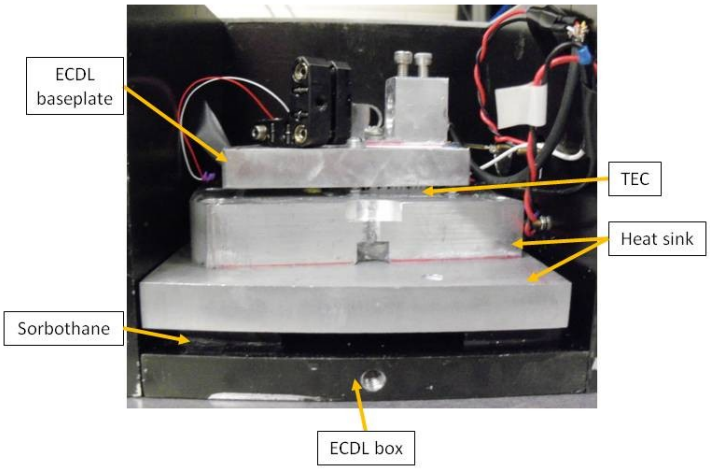

(b)

Figure 2.2. (a) Top and (b) side-on views of one of our homemade ECDLs.

2.1.3 ECDL design

Figure 2.2 shows one of our home-made lasers. All the parts needed to construct our ECDLs are either commercially available or readily machined in the Physics machine shop. The output from a bare diode is highly divergent and needs to be collimated. We use a Thorlabs aluminum tube assembly (Thorlabs model LT230P) to house the laser, with a 4 mm lens placed at one end of the tube to produce a collimated output. This tube is secured inside a machined aluminum mount.

We use a diffraction grating with 1200 lines/mm groove density as the optical feedback element. Using epoxy, the grating is glued to an ultrastable 1/2" mirror mount, also from Thorlabs (model KM05). In Littrow, the horizontal tilt adjustment on the mirror mount allows coarse (tens of GHz) tuning of the output wavelength. For finer (~MHz) tuning we use a piezoelectric transducer (PZT; Micromechatronics AE0203D04F) that can adjust the external cavity length by up to 6μm when 150 V (maximum) is applied. For locking the laser to an atomic transition, we send an electronic feedback signal to the PZT to stabilize the output frequency.

ECDLs are also extremely sensitive to changes in temperature, mechanical vibrations and air currents. Temperature changes not only influence the diode and its internal cavity, they can also cause noticeable fluctuations in the external cavity length and make the entire system unstable. This problem is mitigated by using thermoelectric coolers (TEC) that maintain the laser diode and the external cavity at a constant temperature. A TEC uses the Peltier effect to transfer heat from a source to a sink. The diode housing and grating are mounted on an aluminum baseplate that sits directly on top of a 30 mm × 30 mm TEC element. The TEC in turn is positioned above a 5" × 5" × 1" aluminum block that acts as the heat sink.

We place the ECDL inside a 6" × 6" aluminum box to minimize the effect of air currents. Even so, the laser is susceptible to mechanical noise, from dropping a tool on the optical table to moving a chair along the floor. To mechanically decouple the ECDL, we put ½" thick pieces of sorbothane between the thermal sink and the bottom of the laser box. In Figure 2.2(b), we show the laser cavity, TEC and sorbothane pads.

Once the laser box is assembled, current is supplied to the laser diode using a commercially available, low noise, modular laser diode driver from Thorlabs (LD8002). The TEC is controlled using a separate Thorlabs temperature controller, model TED8020.

2.2 Locking ECDL to an atomic reference

As mentioned earlier, the optical feedback provided by the grating provides single mode output. It also stabilizes the frequency to a linewidth on the order of a few MHz. To resolve hyperfine levels that are separated by ~MHz spacing, we need to further reduce the laser linewidth. Active feedback based on an absolute, stable reference offers a solution by reducing the linewidth to < 1 MHz. We use the hyperfine transitions of atomic ^{85}Rb and ^{7}Li to lock the 780 nm and 671 nm MOT lasers, respectively. Below we discuss the technique of saturated absorption spectroscopy to obtain the hyperfine spectrum, and include a brief mention of the homemade electronics that are needed to lock the ECDLs.

2.2.1 Background on saturated absorption spectroscopy

Doppler-free saturated absorption spectroscopy provides a means of probing an atomic sample by eliminating linewidth broadening due to the Doppler effect. A schematic outlining the procedure is shown in Figure 2.3. A strong pump beam tuned through a hyperfine transition is incident upon the atoms, with a weaker probe beam, also at the same frequency as the pump, counter-propagating and interacting with the same atoms as the pump laser. Atoms in motion in the interaction region see one laser beam blue-shifted, while the other beam is red-shifted. Only those atoms with close to zero velocity will concurrently interact with both laser beams. A high intensity pump laser significantly depletes the ground state, causing the ground-to-excited-state transition to saturate. This decreases the probe absorption, and we can observe narrow peaks in the Doppler broadened absorption background. Subtracting the background via a second probe beam produces the Doppler-free hyperfine peaks, which are suitable for producing an error signal to lock the laser.

2.2.2 Peak locking scheme

The output frequency of a laser diode drifts on a short time scale due to noise in the control electronics, mechanical vibrations, low frequency noise, etc., and on a longer time scale due to temperature fluctuations that cause changes in the external cavity length. One approach to stabilizing the laser with a linewidth $<$ 1 MHz is to directly lock the laser to one of the peaks obtained from saturated absorption spectroscopy. Essentially, the idea is to create a signal that can provide information on not only the frequency drifts but the direction of the drifts as well, and

feed this information back to the laser diode to correct for these drifts. In the process, we have to provide a signal that is relatively insensitive to noise, intensity fluctuations, etc.

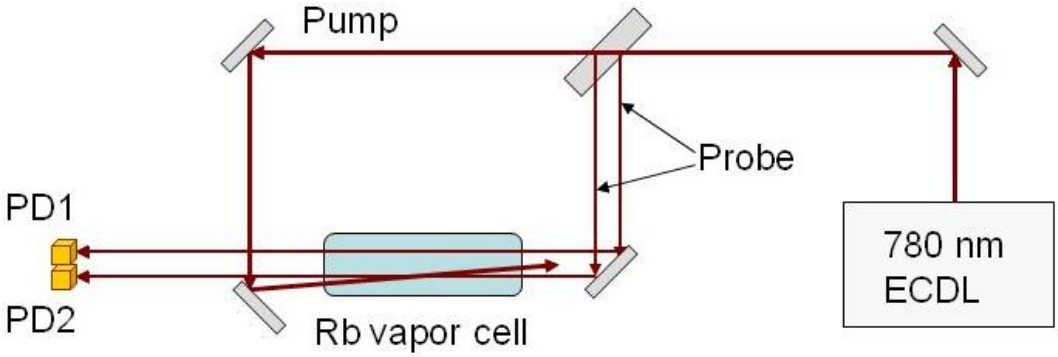

Figure 2.3. Saturated absorption spectroscopy setup. The Doppler broadened saturated absorption peaks are detected by photodiode 2 (PD2) and the Doppler broadened background is detected by PD1. The background is electronically subtracted as part of the locking circuit.

Locking the laser to the top of a saturated absorption peak reduces most of these discrepancies. The procedure is as follows: we monitor the difference signal of two photodetectors, with one photodiode detecting the probe beam interacting with the pump, and the second monitors the noninteracting probe. Electronically subtracting the signal therefore gives us Doppler-free saturated absorption peaks. As the laser frequency is being scanned across these resonances at a few Hz, it is also being 'dithered' at a frequency Ω which is typically tens of kHz. Thus the laser frequency ω is:

$$\omega\,(t) = \omega_0 + a\cos(\Omega\, t) \tag{2.3}$$

The dither signal affects the voltage output of the photodiodes:

$$V\,(\omega(t\,)) = V\,(\omega_0 + a\cos(\Omega\, t\,) \tag{2.4}$$

Expanding the above equation to first order gives:

$$V(\omega(t\,)) \sim V(\omega_0) + \frac{dV}{d\omega} a\cos\,(\Omega\, t) \tag{2.5}$$

The first term is dc and can be ignored. The second term contains the error signal correction. The error signal changes sign depending on the drift – given by $dV/d\omega$ – of the laser, and also crosses zero at the top of the peak, thus providing a good reference for the locking circuit. As an example, Figure 2.4 shows the error signal for the ^{85}Rb(5s) $F = 3 \rightarrow (5p_{3/2})$ F' hyperfine peaks.

The Doppler-free hyperfine structure and the corresponding error signal are generated using a homemade feedback and locking circuit. Briefly, the circuit takes the difference current from the saturated absorption photodetectors and uses a transimpedance amplifier for current-to-voltage conversion. This voltage is mixed with a 7 kHz dither signal using a commercial mixer chip and produces an error signal. A part of the mixer output is delivered to the modulation input of the laser current controller and corrects for fast frequency changes. The other part provides feedback to the PZT (via an integrator op-amp) for a robust peak lock. More details of the locking circuit can be found in the thesis of Dionysis Antypas [62].

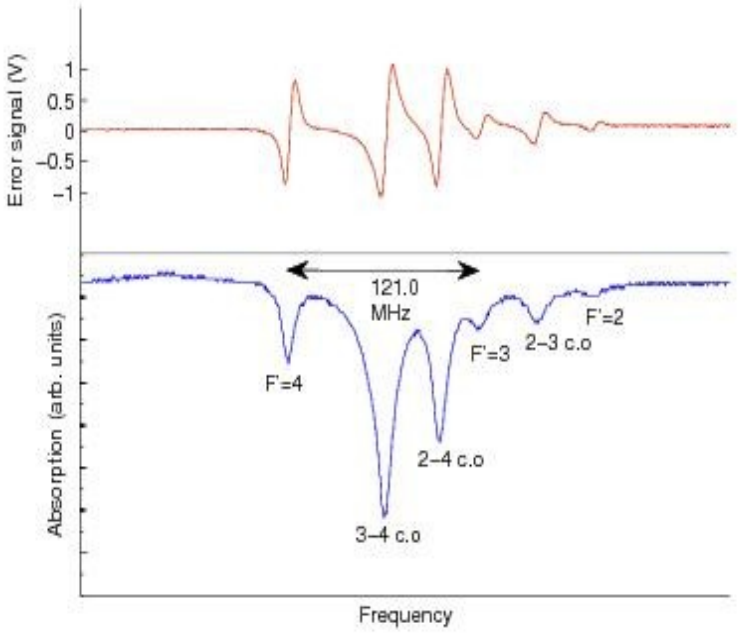

Figure 2.4. Error signal (top) corresponding to the respective hyperfine and crossover (c.o) peaks (bottom) for the ^{85}Rb(5s) $F = 3 \rightarrow (5p_{3/2})$ $F' = 2, 3, 4$ hyperfine transitions. The wavelength (frequency) increases (decreases) to the right.

2.2.3 Mode-hop-free ECDL

For reliable MOT operation we need all of the diode lasers to be tightly locked with minimal frequency drift. Other applications of ECDLs may instead require large, continuous frequency tuning. Going back to Figure 2.1, the vertical line indicates the preferred external cavity mode, n, that suffers the least round trip losses. If we start to tune the output frequency of the laser by changing the PZT voltage, the resulting change in the external cavity length translates the mode structure. Since we have not changed the injection current, the internal cavity mode remains unchanged. Once mode n has shifted by more than half the FSR, the losses for the $(n + 1)^{st}$ mode will decrease, and the frequency will jump so that lasing occurs on this mode. This 'mode-hopping' is an undesirable outcome of tuning the length of the external cavity.

One approach to solving this problem is to tune the internal and external cavity modes in sync by adjusting the PZT voltage and injection current in a fixed ratio. To determine this tuning factor, the PZT voltage is scanned and the injection current is kept fixed. This tells us how the laser frequency changes as a function of PZT voltage, i.e. ν/V_{PZT}. Similarly, we apply a voltage to the modulation input of the laser current controller while keeping the PZT voltage constant. The current controller has a specified modulation coefficient that controls the change of current for an input voltage. Similar to the PZT, we can determine the change of laser frequency as a function of modulation voltage: ν/V_{MOD}. The ratio V_{MOD}/V_{PZT} gives the voltage ratio needed for mode-hop-free tuning of the diode laser.

We implemented the feedforward circuit with a 1560 nm homemade ECDL that acts as the seed laser for a 1 W erbium-doped fiber amplifier (EDFA). To test the mode-hop free tuning range of the laser, we frequency doubled the EDFA output and scanned across the Rb D_2 hyperfine lines.

The second harmonic was produced with an MgO doped PPLN crystal from Covesion, Ltd. Figure 2.5 shows the mode-hop free spectrum. The ^{85}Rb and ^{87}Rb hyperfine lines are superimposed on the Doppler broadened background. With the feedforward circuit, we can scan at least 20 GHz without mode-hops. A larger mode-hop free laser at 780 nm has also been demonstrated in our lab [63]. We will return to the 1560 nm ECDL in Chapter 5.

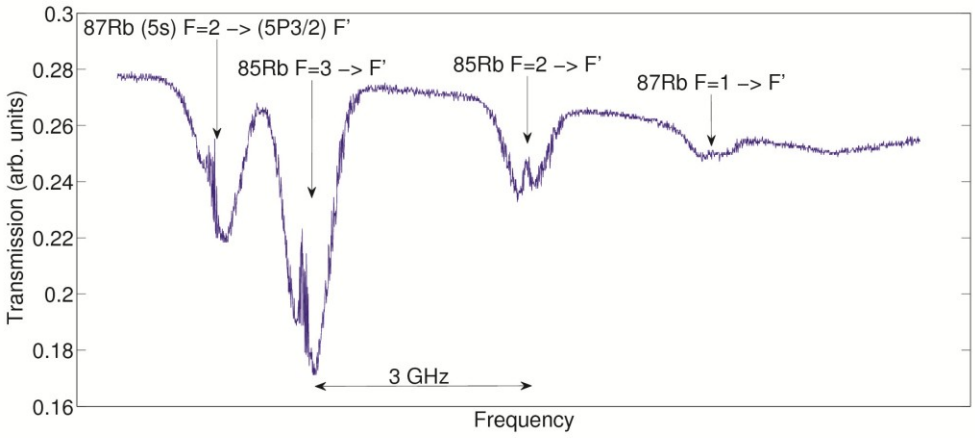

Figure 2.5. A section of the 20 GHz mode-hop-free scan of the frequency doubled 1560 nm ECDL, showing the hyperfine peaks of ^{85}Rb and ^{87}Rb.

2.3 Rb MOT lasers

Rb atoms interacting with light resonant with a cycling transition undergo thousands of photon scattering events per second. Momentum conservation ensures that we are reduce the kinetic energy of the atoms and cool them in the process. However, because the energy level structure of real atoms deviates from an ideal two-level system, the atoms will not be completely confined to the cycling transition, and will decay to the ground hyperfine level that is nonresonant with the cooling light. To efficiently cool Rb atoms, therefore, we need light at two frequencies: a cooling laser resonant with the cycling transition and a repump laser to bring the atoms occupying the 'dark' ground hyperfine level back into the cycling transition. The cooling and repump transitions for ^{7}Li and ^{85}Rb are shown in Figure 2.6.

2.3.1 Rb cooling (trap) laser

The trap light is provided by a Sacher Lasertechnik Tiger laser in Littrow configuration. The specified maximum output power of the laser is 1 W, but after two optical isolators and a polarizing beamsplitter cube (to pick off light for the saturated absorption spectroscopy setup) we have ~750 mW of maximum available power.

Due to the Doppler shift of the background Rb vapor source, we detune the trap laser frequency from the 5s (F = 3) $\rightarrow$ 5p$_{3/2}$ (F' = 4) transition. The frequency shift is carried out using an

acousto-optic modulator (AOM; Crystal Technologies, model 3080-120, center frequency 80 MHz). Phonons generated in a TeO_2 crystal scatter the incoming photons, and based on momentum conservation, the diffracted beam has either a higher or lower frequency compared to the undiffracted (incident) beam. Given the available AOM frequencies and allowed hyperfine transition frequencies, we proceed as follows: using the saturated absorption setup, we lock the trap laser to the $F = 3 \rightarrow F' = 2$–4 crossover resonance. This transition is 92.05 MHz below the cycling transition, and so we upshift the cooling laser frequency using the AOM by 73 MHz for a detuning $\delta_{Rb} = -19$ MHz. The detuning is a balance between two factors: as the cooling light is brought closer to resonance, the trapped atoms fluoresce more, which gives rise to radiative heating and in effect increases the MOT temperature. Detuning too far away from resonance can reduce the number of trapped atoms to begin with.

2.3.2 Rb repump laser

The repump laser is a homemade ECDL using a Sanyo DL7140-201S 70 mW laser diode. The design is identical to the ECDL shown in Figure 2.2. As with the Rb trap laser, the repump also uses an AOM to shift the frequency for an appropriate locking transition. For ^{85}Rb, atoms falling out of the cycling transition decay to the ^{85}Rb(5s) $F = 2$ ground hyperfine state and are 'repumped' into the cooling transition via the $F = 2 \rightarrow F' = 3$ transition. The repump is locked using a separate saturated absorption spectroscopy scheme to the $F = 2 \rightarrow F' = 1$–2 crossover peak, and the AOM upshifts the output by 78 MHz.

2.4 Li MOT lasers

The setup for the Li cooling and repump lasers has undergone modifications since the initial observation of LiRb PA with trap-loss spectroscopy. In the original version (ver. 1), we used a Toptica DLPro ECDL (Littrow) as a master laser in an injection locking configuration. To injection lock one laser to another, the output of a single mode laser – the master laser – is injected into a free-running slave laser (using a polarizing beamsplitter (PBS), for example). This technique utilizes the sensitivity of diode lasers to optical feedback, and allows the slave laser to acquire the characteristics of the master laser and thus operate as an optical amplifier.

Compared to a hyperfine splitting of 3.03 GHz for ^{85}Rb, the ground state hyperfine splitting for ^{7}Li is 803.5 MHz. We can therefore use AOMs to generate the required cooling and repump frequencies. In ver. 1, we split the DLPro output into three: a beamsplitter picked off light for the

saturated absorption setup, and the remaining light propagated through two 200 MHz AOMs. Both AOMs were setup in a double-pass configuration, in which the 1st order diffracted light is retroreflected through the AOM to double the frequency shift. One AOM upshifted the light by 400 MHz, while the other downshifted by 400 MHz to provide the cooling and repump frequencies, respectively. The shifted outputs were injected into two free-running lasers (Opnext HL6545MG, 130 mW maximum output). The outputs of the injection-locked lasers were combined on a non-polarizing beamsplitter cube, and injected into a Toptica BoosTA tapered amplifier (TA) to provide ~250 mW of total power. Using a half-waveplate (HWP) before the beamsplitter, we could control the fraction of amplified power in the cooling and repump transitions.

During day-to-day operation of the Li lasers, we noticed that the injection lock was unstable and the lock time varied from ~1 hr at best to less than 10 minutes. As the slave lasers had a center frequency of 667 nm, significant heating (55 °C) was required to increase the output wavelength to near 671 nm. At 55 °C the diodes were operating near the maximum design temperature, and this may have been a contributing factor to the lock instability, although we could not further investigate this matter further. Nevertheless we were still able to operate the system and study collisions between atoms in the Li and Rb MOTs, and perform initial trap-loss measurements of LiRb PA transitions.

The current incarnation of the Li MOT laser system has removed the need to use injection locking and is vastly more stable. The DLPro output is directly injected into the TA, and part of the TA output is used for saturated absorption spectroscopy. Unlike the excited state hyperfine splitting of ^{85}Rb, the $2p_{3/2}$ hyperfine splitting for ^{7}Li is small enough that it cannot be resolved with our lasers (see Figure 2.6). As a result, the Doppler-free saturated absorption spectrum consists of transitions from the two ground state hyperfine levels, and the ground hyperfine crossover resonance. We lock the Li laser to the crossover resonance by upshifting the saturated absorption light using a 200 MHz AOM that is set up in a double pass configuration, as shown in Figure 2.7. The remaining output is focused into an EOM driven at 800 MHz with 6 W of input rf power. As the laser frequency is locked at f_0 + 400 MHz, where f_0 is the DLPro output frequency, the cooling and repump frequencies are generated by the carrier and upper sideband of the EOM, respectively. Using the EOM simplifies the optical setup and takes care of the instability observed earlier in ver. 1.

For ease of alignment, the EOM is mounted on a rotation mount that is fixed to a 2D translation stage. We pick off part of the Li light after the EOM and steer it towards a 2 GHz Fabry-Perot cavity to monitor the repump sideband. As rf modulation is applied to the crystal, the carrier and sideband frequencies are clearly visible at the correct spacing. Second order sidebands can also be seen. Inevitably the effect of these higher order sidebands (and of the unused first order sideband) is to reduce the power in the relevant frequency components (cooling and repump) of the light.

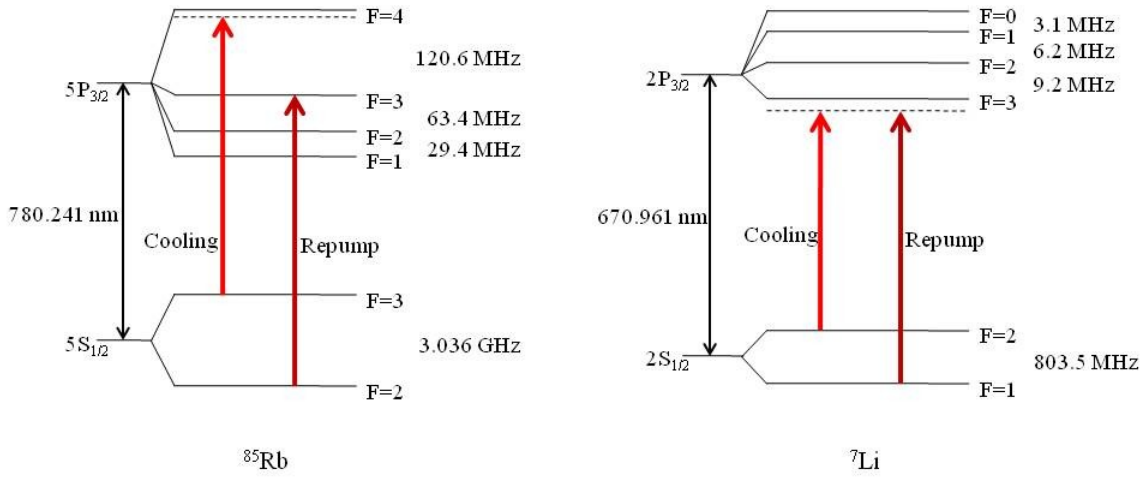

Figure 2.6. Energy levels and MOT laser transitions for ^{85}Rb and ^{7}Li.

2.5 Li Zeeman slower

The Li MOT is loaded from a Li oven that produces a collimated beam of atoms traveling at over 1000 m/s. The vast majority of these atoms are travelling too fast to be captured in the MOT region, and so a means to decelerate the atom beam is needed. Momentum transfer between a light field and the atoms is a viable option (similar to the cooling light for the MOT, except only along the axis of the atom beam). The light should be resonant with a cycling transition; hence we can pick off part of the EOM output for this purpose. Due to Doppler shifts, most of the atoms

will be off resonant with any slowing light, but a spatially varying magnetic field can induce a Zeeman shift that will keep atoms on resonance. This combination of a counterpropagating, near-resonant slowing beam and a 'Zeeman slower' imparts sufficient momentum kicks to decelerate the atoms and capture them in the MOT region. Light for the Zeeman slower is picked off after the EOM and downshifted by 80 MHz with an AOM.

The schematic for the Li and Rb MOT lasers is shown in Figure 2.7.

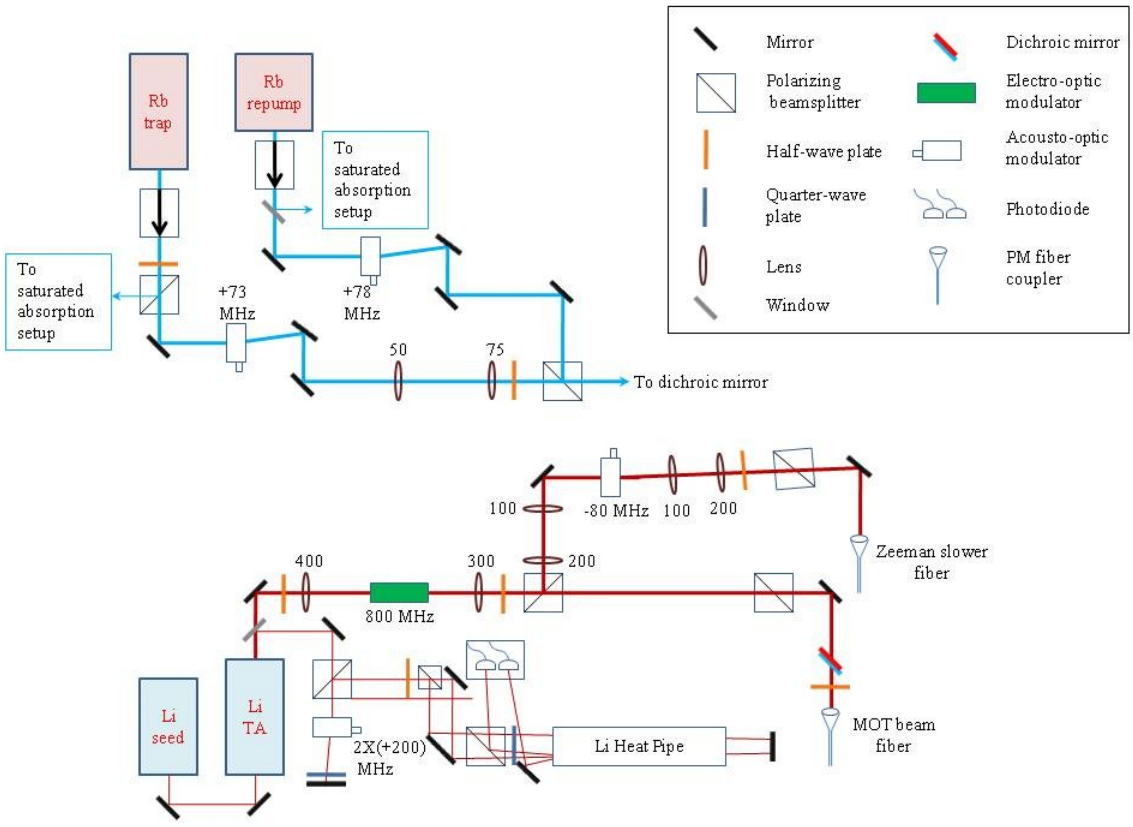

Figure 2.7. Layout of the MOT lasers. After adjusting the laser frequencies using AOMs (Rb trap and repump) and EOM (Li), all three MOT laser beams are combined on a dichroic mirror and launched into the MOT beam fiber. For the Zeeman slower, part of the Li TA output after the EOM is frequency shifted with an AOM and launched into a separate Zeeman slower fiber. The focal length of lenses is given in mm.

2.6 AOM board

All the AOMs needed for the experiment are controlled using a homemade circuit board that is interfaced to Labview (see the thesis of John Lorenz for more details). The PCB was designed and implemented by REU student Roger Ding. The AOM frequency sources are voltage controlled oscillators (VCO) from Minicircuits. AOMs typically need over 1 W of rf power; the VCO outputs are amplified using rf amplifiers (Minicircuits ZHL-1A). Rf switches are installed to rapidly switch on and turn off the AOMs. Attenuators placed on the outputs limit the rf power to the AOMs, which is typically ~1.3 W. The VCO frequencies are controlled using a Labview program.

2.7 Transporting light to experimental chamber

Light from the laser table is transported to the MOT chamber using polarization-maintaining (PM) fibers. The fibers were custom-made by OzOptics, based on the input beam characteristics of our lasers. In order to simplify the optical setup, we combine the Rb trap, Rb repump and Li lasers (with the cooling and repump sidebands) onto the same PM fiber, with the beam sizes individually adjusted using telescoping lenses to maximize the coupling efficiency. A second PM fiber is used to transport the Zeeman slower light. Table 2.1 shows the beam sizes and coupling efficiencies for all the four beams. The output end of the MOT laser coupling fiber has an attached collimating lens that produces a 5 mm $1/e^2$ diameter output beam.

Table 2.1 Beam sizes and typical coupling efficiencies of the MOT lasers and Zeeman slower beam.

	$1/e^2$ beam diameter (mm)	PM fiber coupling %
Rb trap	2 x 1.02	51
Rb repump	2 x 0.74	54
Li TA output	2 x 1.28	55
Zeeman slower	2 x 1.28	50

As the name suggests, PM fibers preserve the polarization of the input light, given that the input polarization is aligned with the fiber's polarization axis. Slight misalignment can be detected as a fluctuation in s- and p-polarization power at the output (by measuring the power reflected or transmitted by a PBS, respectively). This fluctuation is minimal for good polarization alignment

and least sensitive to mechanical or thermal perturbation of the fiber. For the fiber to work effectively, however, the input polarization extinction ratio (PER; ratio of p- to s- polarization) has to be at least 1000:1 (30 dB), as specified by the manufacturer. None of our lasers satisfy this requirement, but the PER can be improved by using a half-wave plate (HWP) and PBS. The beamsplitters in our setup had a better extinction ratio for p-polarization (30 dB) than s-polarization (20 dB), and so we used the HWP-PBS combination to maximize the transmitted (p-) polarization separately for each source. Finally, a HWP was placed immediately before the MOT fiber input to adjust for any reduction in the extinction ratio caused by the last steering mirrors and/or the dichroic mirror before the coupling input (see Figure 2.7).

We used a similar HWP-PBS combination for the Zeeman slower beam. Unlike the output end of the MOT PM fiber, there is no collimating lens for the fiber coupling the Zeeman beam. Instead, we have placed a pair of lenses at the output that expand and collimate the beam to a ~25 mm beam diameter.

2.7.1 Optimizing fiber coupling efficiency

The PM fiber coupling efficiency is highly sensitive to minor changes in alignment. We've observed that the coupled power of the Rb trapping laser can change by ~5% due to drifts in the mirror mount knobs, whereas the Rb repump laser coupling is slightly more stable. If the coupling power has been optimized, the drift may be less, again more so for the Rb repump than the Rb trap laser.

For the Li laser, the beam shape is significantly distorted by the EOM crystal, which in turn reduces the coupling efficiency. The beam shape may also visibly change as the crystal heats up when the rf power is applied. We let the EOM reach thermal equilibrium after turning on the rf source (~30 minutes) and translate the EOM mount to optimize the coupling efficiency. To avoid major realignment, we monitor coupling efficiencies for all the lasers on a regular basis.

Recently the power coupled into the MOT fiber decreased significantly (15% coupling for the repump, compared to a maximum of 56%). The problem was traced to a sharp kink in the fiber jacket where it was secured to a metal frame. Fixing the kink returned the coupling efficiency to previous values; however extreme care has to be taken when working around the fiber to ensure there is no further damage.

2.8 MOT optics

Light for the Li (671 nm) and Rb (780 nm) MOTs falls in a range such that the same set of broadband dielectric mirrors can be used for both wavelengths. The same also applies for the AR-coated lenses and beamsplitters. Figure 2.8 shows the MOT optics layout. The PM fiber output (5 mm $1/e^2$ beam diameter) is directed towards a telescoping lens assembly that magnifies the beam to ~20 mm. This enlarged beam is split into vertical and horizontal components with a 1:2 power ratio that is adjusted using a HWP placed before the PBS. A second HWP-PBS pair placed in the horizontal path gives the two orthogonal horizontal beams. In this way we have independent control on the power ratio of each of the three orthogonal MOT beams.

Quarter-wave plates (QWPs) are placed in each beam path after the final steering mirrors before the MOT chamber. Each beam is centered on the respective MOT window by using an aperture. The beams transmitted through the MOT chamber pass through QWPs in each arm, and are retroreflected with the opposite handedness than the incident circularly polarized beam. Due to window losses, the retroreflecting mirrors are carefully positioned to balance the intensity in each pair of MOT beams.

2.9 MOT characteristics

2.9.1 Measuring atom number and density

Once the MOT optics are set up and aligned carefully, we start loading Li and Rb atoms in the respective MOTs. Rb atoms decaying from the $5p_{3/2}$ state fluoresce at 780 nm, which is barely visible to the naked eye. To confirm the presence of the Rb MOT, we set up an IR camera using one of the 1.33” windows. As the MOT trapping and repump beams are unblocked and the anti-Helmholtz magnet coils are turned on, we observe fluorescence from the trapped atoms. Whereas we need the IR camera to identify the Rb MOT, the Li MOT fluoresces at a clearly visible 671 nm and can be seen with the naked eye.

After visual confirmation of the MOTs, we set up photodiodes to determine the fluorescence levels, which are needed to calculate the number of trapped atoms for each species. The optical power P from MOT fluorescence incident on the photodiode is given by

$$P = \frac{\Omega}{4\pi}\frac{hc}{\lambda}\gamma_{sc}N \tag{2.6}$$

where N is the number of trapped atoms, Ω is the unit solid angle over which fluorescence is collected, λ is the fluorescence wavelength (780 nm for ^{85}Rb, 671 nm for ^{7}Li) and γ_{sc} is the photon scattering rate per atom:

$$\gamma_{sc} = \frac{\Gamma}{2}\frac{s}{1+s+\left(\frac{2\delta}{\Gamma}\right)^2} \tag{2.7}$$

Here Γ is the natural linewidth of the cycling transition, δ is the detuning from resonance, and $s = I/I_0$, the ratio of MOT beam intensity to the saturation intensity I_0. The relevant parameters for Rb and Li MOT operation are given in Table 2.2.

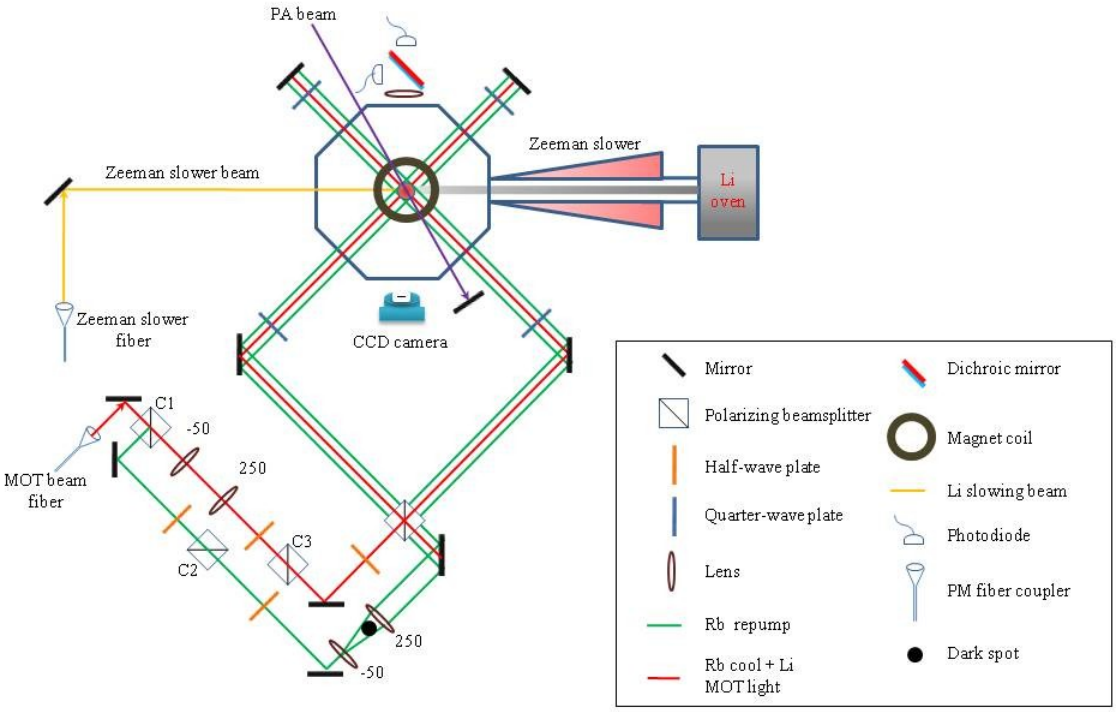

Figure 2.8. Top view of the MOT chamber and the optics directing the Li and Rb lasers towards the MOT region. All focal lengths are given in mm.

Table 2.2 MOT parameters used for initial MOT diagnostics and atom number calculations.

	Γ (MHz)	δ (MHz)	I_0 (mW/cm^2)	I (mW/cm^2)
^{7}Li	$2\pi \times 5.87$	-12	2.5	12.7
^{85}Rb	$2\pi \times 6.07$	-24	1.7	79.6

Next, we determine the MOT atom density. We use a CCD camera to capture images that are recorded and analyzed in Labview. The camera is a Basler SCA640-70fm, with 659 × 490 pixels and a pixel size of 7.4 um × 7.4 um. A 5 cm lens focuses the MOT images onto the CCD. We calibrate the camera magnification using a known object at the same distance from the CCD as the MOT, from which we get a magnification factor of 0.34. Once the images are recorded, we use a second Labview script to calculate the size of each image. The script loads and plots the raw pixel value information and takes a horizontal and vertical slice through the center of each image to calculate the 1/e diameter of the cloud. This information allows us to calculate the volume and together with the atom number measurement, we can determine the MOT density. Typically we trap ~5×10^7 Li atoms at a density of ~5×10^9 cm^{-3}. For Rb, the numbers are ~1×10^8 and ~4×10^9 cm^{-3}, respectively. Figure 2.9 shows CCD images of our Rb and Li MOTs.

2.9.2 MOT loading and collision rates

We have performed extensive studies of collisions between trapped Li and Rb atoms [64 and 56] based on MOT fluorescence measurements. Here we present a brief discussion of these collision measurements and the need to minimize these interspecies collisions for efficient molecule formation.

Figure 2.10 shows Li and Rb MOT fluorescence captured by two photodiodes. The Li (Rb) curve is recorded in the absence of the Rb (Li) MOT. The Rb fluorescence is picked off from a dichroic mirror placed after a pair of collecting lenses which reflects light at 780 nm and transmits at 670 nm (Figure 2.8). There is of course leakage at both wavelengths, but this contributes a negligible background offset. During the MOT operation, atoms are lost due to collisions between trapped atoms and also collisions of trapped atoms with background (untrapped) atoms. This loss is balanced by the steady trapping of background atoms, and a steady state is reached as seen by the fairly constant fluorescence signal for both Li and Rb in Figure 2.10.

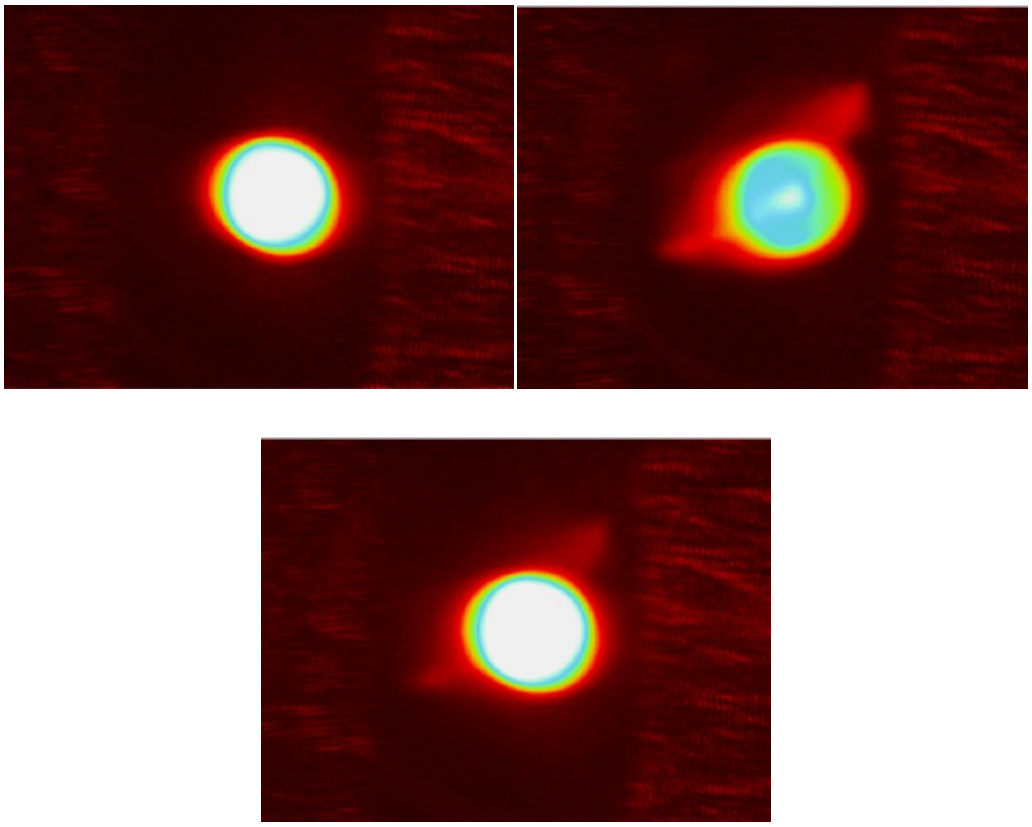

Figure 2.9. CCD images of the Rb MOT (top left), Li MOT (top right) and overlapped Li and Rb MOTS (bottom).

If we load one MOT in the presence of the other, there are significant collisions between trapped Li and Rb atoms and as a result we lose atoms from the MOT. Figure 2.11 clearly shows this behavior. We load the Rb MOT in the absence of the Li MOT at t = 20 s. At t = 100 s, we start loading the Li MOT, and observe ~50% decrease in Rb MOT fluorescence, which indicates that approximately half as many atoms as before are now trapped. When we turn off the Rb MOT at t = 175 s, we notice that the Li MOT fluorescence increases by more than 50%, indicating more Li atoms are trapped when the Rb MOT is absent. These interspecies collisions reduce the atom density, which is not ideal for creating ultracold LiRb molecules. We mitigate this loss of atoms by implementing a dark-SPOT Rb MOT, as explained in the next section.

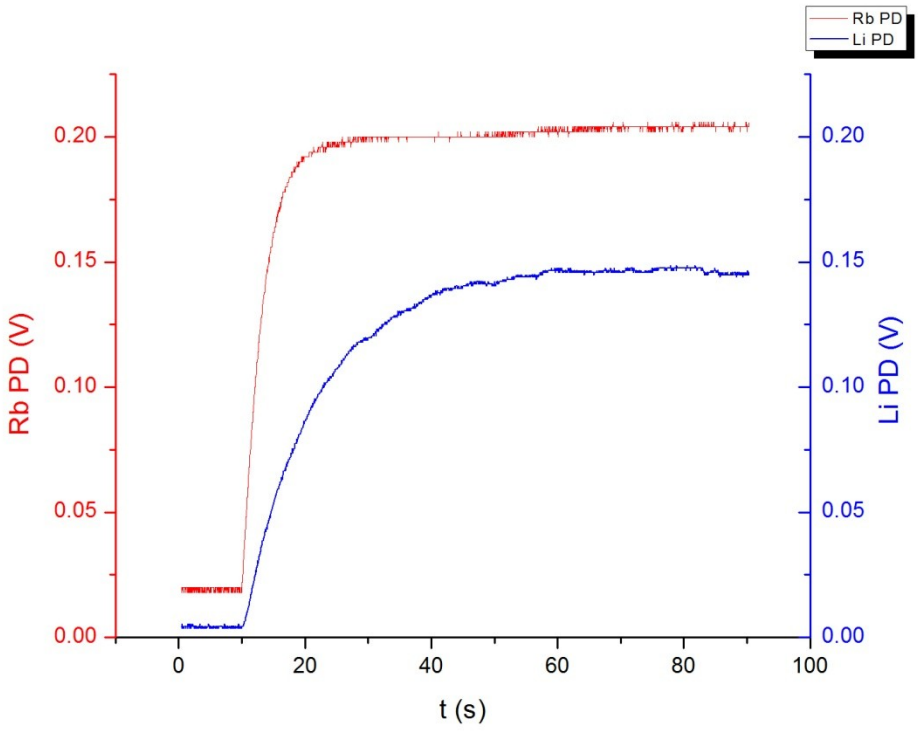

Figure 2.10. Li (blue) and Rb (red) MOT loading curves. Each MOT is loaded in the absence of the other. The DC offset seen from t = 0 to t = 10 s is due to the photodetectors picking up stray reflections from the chamber.

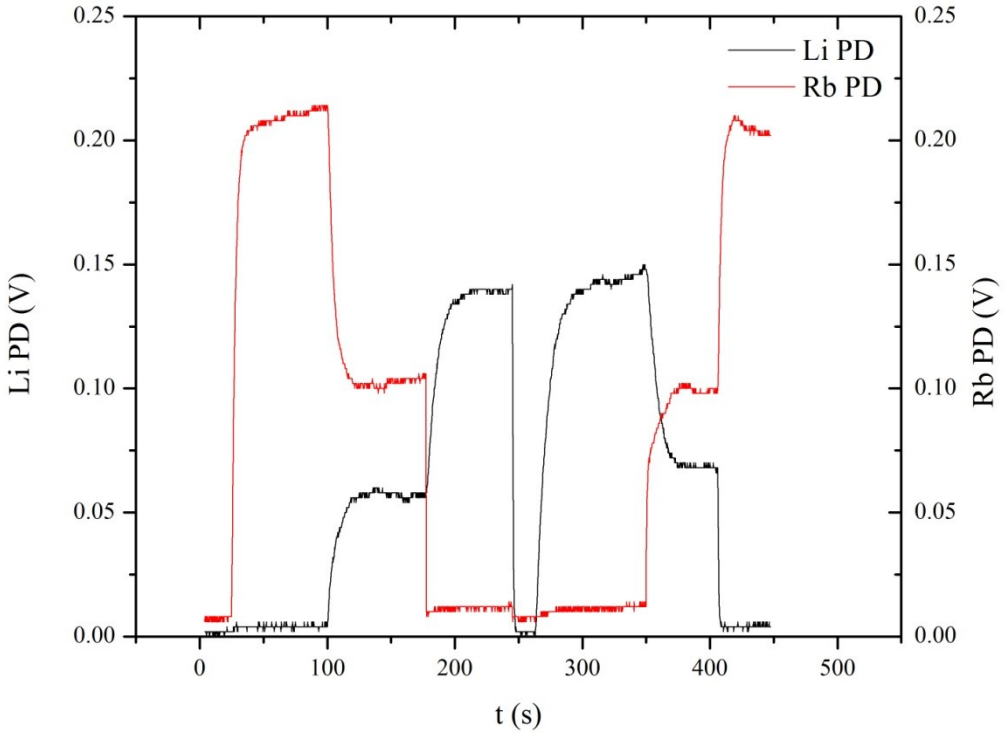

Figure 2.11 Evidence of inter-species collisions in Li and Rb. The Rb MOT is loaded first and reaches steady state. When we turn on the Li MOT at t = 100 s, there is a ~50% decrease in the Rb MOT fluorescence, which indicates a proportional decrease in trapped Rb atoms. Next, we turn off the Rb MOT at t = 175 s and see an increase in the Li MOT fluorescence. This behavior reflects significant inter-species collisions.

2.9.3 Rb Dark MOT

The collision-induced trap losses were an encouraging sign that the MOTs were overlapped (also confirmed by MOT CCD images), but the Rb atom loss in particular was severe, causing ~50% trap loss with the Li MOT present (shown in Figure 2.11) and a reduction in Rb number density. As the PA rate depends on MOT density (among other factors), this collision-induced density reduction needed to be mitigated.

In the early 1990s, Wolfgang Ketterle and coworkers at MIT devised a scheme to maximize MOT density as a step towards creating Bose-Einstein condensates (BECs) of sodium atoms [65]. Their research indicated two important factors that limited the maximum achievable density in a MOT. Consider a single species MOT. Collisions between atoms in the ground and excited state can transfer sufficient kinetic energy to escape the trapping potential. In addition, trapping light also acts as a heating mechanism. As atoms continuously absorb and scatter photons, equilibrium is reached between inward confining forces and repulsive forces due to the scattered photons that limit the MOT density. The MIT group was able to mitigate both these factors by using a dark spontaneous-force optical trap (SPOT) MOT. Both the additional kinetic energy and fluorescence are a consequence of excited state atoms. The dark SPOT MOT functions to reduce this excited state fraction by forcing trapped atoms into the ground hyperfine state, which is out of resonance with the cooling light. As a result, the MOT density can be increased by an order of magnitude. This approach can be applied to single and dual species MOTs.

To implement this scheme, we need a way to first trap atoms and then force them into the dark state. Ketterle and coworkers did this by blocking the central portion of the repump beam while the trapping light remains unblocked. Atoms on the periphery of the trapping volume are trapped and confined to the cycling transition because both the trapping and repump light are present in this outer ‘shell’. As they move inwards, the atoms cease to interact with the repump light in the dark region created by blocking the repump light, and are shelved to the dark state.

For our experiment, we use a Rb dark SPOT MOT, as the collisional losses are significant between Rb atoms in the $F = 3$ (upper) ground hyperfine state and trapped Li atoms. Our setup before coupling light into the MOT PM fiber is such that the Rb trap and Li laser polarizations are perpendicular to the Rb repump light. Since the fiber maintains the polarization of each laser, a PBS at the fiber output (C1) reflects the Rb repump light and transmits the other two (Figure 2.8). Light transmitted by a HWP-PBS (C2) pair in the repump beam path goes through a -50 mm lens. We put a glass slide with a 6mm opaque disk (cut out from the cover of a floppy disk using a hole punch) in the expanded beam path. A second 250 mm lens gives collimated Rb repump light with a dark center part. It is then combined with the trapping light on C3. With the dark MOT operational, the collisional losses between trapped Li and Rb atoms are greatly reduced.

2.10 Vacuum chamber

Our work with a dual species MOT apparatus began with a markedly different MOT chamber, a 6" stainless steel spherical octagon (Kimball Physics MCF600-SphOct-F2C8). The first observation of Rb and Li MOTs took place in this chamber. However, with an eye towards future experiments, we came to the conclusion that this chamber would be insufficient to satisfy our needs for greater optical access and space for an ion detection assembly.

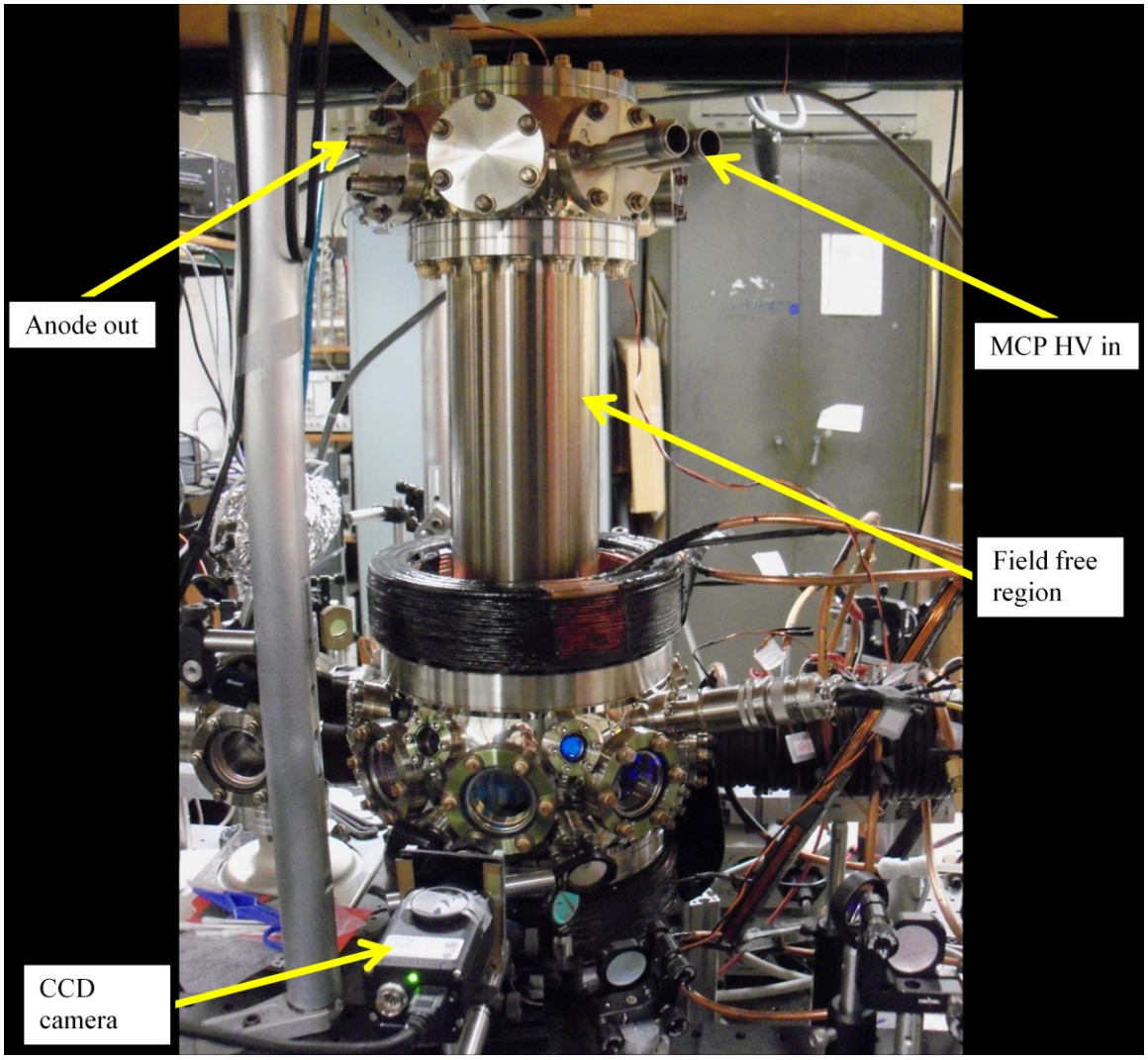

Figure 2.12. Li and Rb MOT chamber. We monitor the MOT clouds using the CCD camera. For ionization spectroscopy, the ion species are accelerated towards the field-free region by field plates. The MCP assembly is set up in the smaller chamber above the field free region.

Figure 2.12 shows the MOT chamber, which is a commercial 8" spherical octagon from Kimball Physics (MCF800-ExtOct-G2C8A16). It has two 8", eight 2.75" and sixteen 1.33" CF ports. All of the windows mounted on the chamber are AR coated for the 650 – 1100 nm range. The 8" ports are used for the vertical MOT beams, with the top flange connected to a 10.6" long CF 6" nipple that acts as the field free region for TOF experiments. The other end of the nipple connects to the smaller 6" spherical octagon chamber that now holds the MCP assembly.

The horizontal MOT beams pass through two pairs of orthogonal CF 2.75" windows. One of these windows also transmits the PA laser, which is non-collinear with the MOT beams. To collect the MOT fluorescence and image the cloud with the CCD camera, we use a third pair of CF 2.75" windows. Of the two remaining windows, one is connected to the Li Zeeman slower (and through it to the Li oven and one of two ion pumps), and the other leads to a six way cross that connects to an ion gauge. Directly across from the Zeeman slower, a 1" sapphire window-mounted flange is secured to the cross to transmit the Zeeman slower light. Unlike borosilicate glass, sapphire reacts minimally with Li.

The CF 1.33" ports are used for the following: one port is used for the Rb getter feedthroughs, one for the electric field plate feedthroughs, and a window is mounted on the third port to direct the ionizing laser into the chamber. Four of the CF 1.33" ports have blank flanges connected to them, while the rest all allow optical access to the chamber. These can be used for future experiments that require a high powered laser to create a dipole trap, for example.

The MOT chamber, Zeeman slower tube and the Li oven are all maintained at ultra-high vacuum (UHV), $\sim 10^{-10}$ Torr, using two ion pumps. For good system performance, it is critical to maintain the lowest possible pressure, and the ion pumps are continuously run to maintain UHV.

The sapphire window that transmits the Zeeman slower beam is another part of the vacuum chamber that needs to be periodically monitored. The Zeeman slower reduces the Li atom velocity so that we can capture the slower moving atoms, but fast moving atoms escape the trapping region and hit the sapphire window. Over time, a coating of Li atoms starts appearing on the window, which reduces the Zeeman slower light transmission and deteriorates the Li MOT performance. We overcome this problem by heating only the sapphire window and the nipple connecting the flange to the six-way cross. We use heat tape, with aluminum foil wrapped around the flange and nipple, and heat up to 190°C for two days before slowly returning to room temperature. This procedure removes the Li layer and returns the system to normal operation.

2.11 PA laser

We use a Coherent 899 cw Ti:Sapphire (Ti:S) ring dye laser as our PA light source. Initially the laser was pumped by a 5 W, 532 nm Coherent Verdi V5, to give a maximum output power of ~200 mW. More recently we have upgraded to an 8 W Lighthouse Photonics Sprout-G pump laser which has increased the Ti:S output to over 400 mW.

The Ti:S offers a broad tuning range and narrow linewidth operation. The laser can be tuned between 770 nm and 900 nm, but the majority of our work is focused on PA transitions below the Li(2s) + Rb($5p_{1/2}$) and Li(2s) + Rb($5p_{3/2}$) levels, which correspond to wavelengths red of 780 nm and 795 nm, respectively. The Ti:S is locked to an external reference cavity with a linewidth of ~1 MHz, which is sufficiently narrow to resolve not only PA transitions but any rotational and hyperfine structure that may be present for individual PA resonances.

We periscope the Ti:S beam up to the center of the MOT chamber. The beam is collimated to a ~0.85 mm diameter with a pair of converging lenses. Part of the beam is picked off at the Ti:S output and fiber coupled to a Bristol 621A wavemeter (accuracy ±60 MHz). The laser lock and frequency are continuously monitored in all of our experiments (for more details of the Ti:S laser, see the thesis of John Lorenz).

As an initial test of the PA laser and MOT operation, we recorded trap-loss spectra for Rb_2, shown in Figure 2.13. Taken with a normal 'bright' Rb MOT, the Ti:S was scanned over ~200 GHz below the Li(2s) + Rb($5p_{3/2}$) asymptote, where we observed many PA resonances previously observed by Heinzen and coworkers [28, 29].

Proper Ti:S beam alignment with the MOT is critical to obtaining a strong PA signal. Before our first observation of LiRb trap-loss, we aligned the PA laser by tuning it first to the Rb (5s) $\rightarrow$ ($5p_{3/2}$) transition. The PA laser disrupts MOT operation when tuned to a Rb atomic transition and results in a decrease in MOT fluorescence. Optimal PA laser alignment is achieved when the MOT fluorescence is minimized. The alignment was then double-checked by switching the Ti:S to a Rb_2 PA resonance and again minimizing the trap-loss signal. Once LiRb PA resonances were observed, minor adjustments of the Ti:S alignment were carried out by fixing the laser frequency on a PA transition and minimizing the MOT fluorescence level.

2.12 Ion detection setup

Our apparatus is capable of detecting ultracold molecules by monitoring changes in MOT fluorescence level, and also by ionizing the molecules and detecting the ion fragments. To create and detect ions in our system, we use ns pulses from an Nd:YAG pumped dye laser that ionize atoms and molecules in the MOT chamber, which are then steered towards a microchannel plate (MCP) assembly and recorded using hardware and software signal acquisition. The details are presented below.

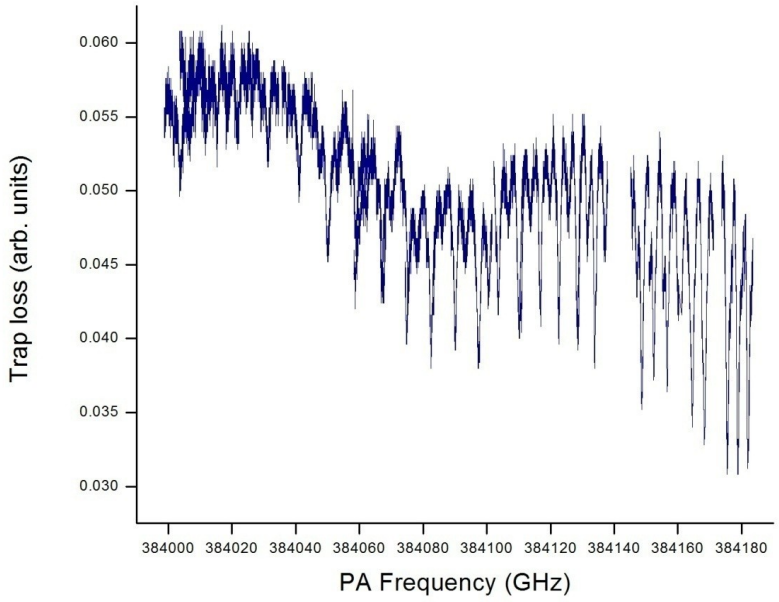

Figure 2.13. Trap-loss spectroscopy of Rb_2, performed as an initial diagnostic of our MOT operation and Ti:S laser. The dips show positions of Rb_2 PA resonances (in PA laser frequency units).

2.12.1 Pulsed dye laser

PA ionization spectra are acquired using multiphoton ionization, as mentioned in Chapter 1. Pulsed dye lasers pumped by ns pulse width Nd:YAG systems deliver ~10^6 W of peak power (~mJs of energy) and can easily ionize PA molecules via multiphoton ionization. In our experiment, we use the second harmonic of a Spectra-Physics Lab 190 Nd:YAG as the pump

source. The YAG generates ~7 ns pulses at 532 nm with a 10 Hz repetition rate. The maximum output energy of the Lab 190 is 500 mJ, but during normal operation we do not require 100% output energy.

The YAG pumps a Spectra-Physics PDL-2 dye laser. The advantage of using the PDL-2 is the large continuous tuning range (tens of nm) and remote control using Labview. Replacing dye is also a straightforward procedure and allows us to work with a large wavelength range. The PDL operates as follows: the pump beam enters the PDL and part of it is picked off by a beamsplitter and focused onto the dye oscillator cell. The generated fluorescence travels perpendicular to the pump direction and is incident on a diffraction grating on one end and an output coupler on the opposite side. This forms a cavity similar to the external cavity in our diode lasers. Once lasing is established, the output wavelength is tuned by tilting the grating either by manually turning a stepper motor control knob, or via remote control through a stepper motor driver interface.

The oscillator cell output strikes the amplifier cell and is set to counterpropagate with the pump beam transmitted by the pump beamsplitter. Finally, the amplified output is directed towards the MOT chamber. For the experiments presented in this thesis, we use rhodamine R590 dye dissolved in spectrophotometric grade methanol. The concentration for the oscillator and amplifier cells is 115 mg/L and 17 mg/L, respectively. With the 532 nm pump, the wavelength range of the dye is between 554 nm and 580 nm, with peak energy at ~560 nm. The dye lasing threshold can be extended by a couple of nm to either the lower or higher wavelength end by making the oscillator dye solution more or less concentrated, respectively.

2.12.2 MCP assembly

For ion detection, we have installed a system of field plates that accelerate the ions towards a microchannel plate (MCP) assembly. The assembly is based on the design proposed by Wiley and McLaren [66] that accelerates ions with three field plates. Each circular plate has a 3.2 cm center hole for the vertical MOT beams. The bottom and middle field plates are spaced by 4.7 cm, and the middle and top plates by 2 cm. This 3-plate assembly helps to focus ions on the detector regardless of their initial positions in the MOT region, thus acting as an ion lens and improving spatial resolution. This feature is critical for future studies on ultracold molecular alignment and orientation. For optimal time-of-flight (TOF) resolution, the field plate voltages are set to the following values: 400 V (bottom), 340 V (middle) and the top plate is permanently grounded to the vacuum chamber body.

The accelerated ions travel through a 30 cm field free region and strike the MCP assembly, shown schematically in Figure 2.14. For unrestricted optical access for the vertical MOT beam, the MCP assembly is positioned ~35 mm away from the axis of the vertical MOT window. To ensure that ions are accelerated towards the MCP assembly, the accelerating field plates are tilted by 5° from the vertical. In addition, we have also positioned permanent magnets on the outer wall of the nipple (field free region) to steer the ions towards the MCPs. We empirically optimize the position of the magnets by maximizing the recorded ion counts for a known LiRb PA resonance.

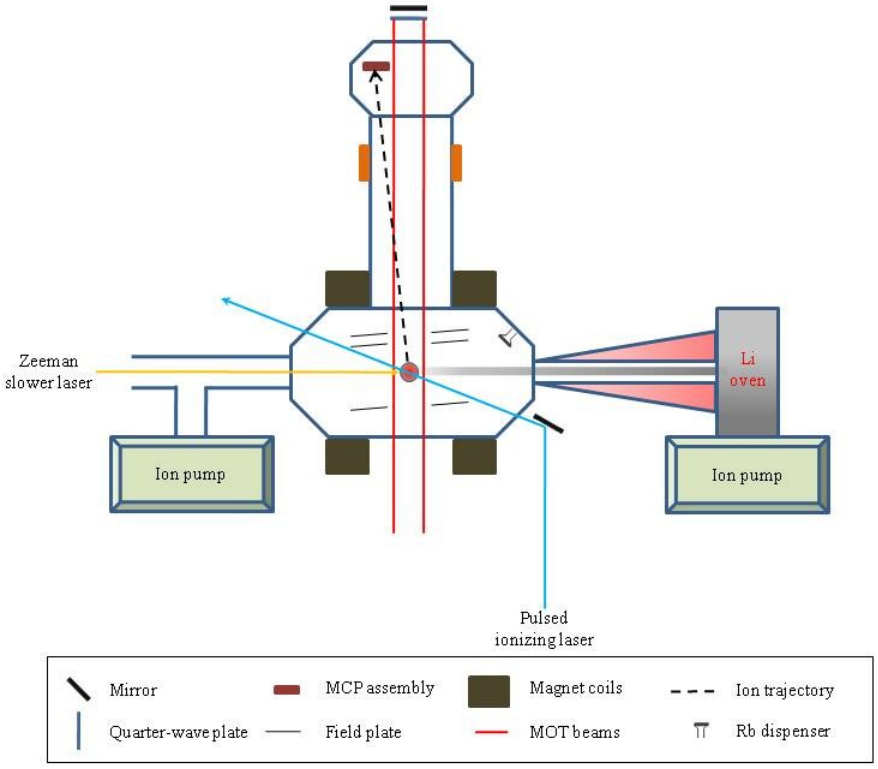

Figure 2.14 MOT chamber schematic showing the field plate and MCP assembly. The field plates are tilted at 5° with respect to the vertical axis of the chamber. This allows clear optical access for the vertical MOT beams. Permanent magnets (orange) on the side of the field-free region steer the ions towards the MCP assembly.

We have installed a double stack MCP (resistance 330 MΩ) and phosphor screen manufactured by Tectra Physikalische Instrumente, Germany. The MCPs can be operated at a maximum

potential difference of 2 kV; however, during daily operation we do not exceed 1.8 kV (lower MCP -1.9 kV, upper MCP -0.1 kV). Care has to be taken to slowly increase the MCP voltage to avoid damaging the assembly. For the first -1000 V, we increase the voltage in steps of -50 V every two minutes. From -1000 V to -1500 V, the voltage increase is -50 V every 5 minutes, and from -1500 to -1900 V, the rate is -50 V every 10 minutes. This turn on sequence has been conveniently automated using Labview.

For TOF ionization spectroscopy, we monitor the MCP current generated by individual ion strikes. The electron cascade from the MCPs hits the metal coated bottom part of the phosphor screen and produces the observable signal. For ionization spectroscopy we do not require spatial resolution of incident ions and do not apply a potential difference to the phosphor screen (this is needed for future studies of LiRb alignment and orientation). The BNC feedthrough is connected to a 50 Ω impedance oscilloscope (bandwidth 350 MHz) to monitor the signal and to the ion counting hardware.

The scheme for detecting ions and acquiring the resulting signal is shown in Figure 2.15. The signal generated by the ion strikes travels via the BNC feedthrough to an Ortec FTA 420-C preamplifier module with a gain of 400. The voltage output from the preamplifier is sent to a LeCroy 821 quad discriminator. For each input signal that is above a user-specified threshold voltage, the discriminator outputs a NIM-logic pulse (NIM stands for Nuclear Instrumentation Methods. NIM logic 0 is 0V and logic 1 is -0.8 V). Both the preamplifier and discriminator are housed in a NIM controller unit. The preamplifier output is also sent to a 50 Ω input impedance oscilloscope to monitor the ion signal. The NIM logic levels are incompatible with our data acquisition (DAQ) hardware that recognizes TTL logic (logic 0 is 0 V, logic 1 is 5 V), and so we use a MC10H125 chip for NIM-to-TTL signal conversion.

The DAQ monitors signal from all four ion species incident on the MCP assembly. However, since we are only interested in $LiRb^+$, a means to selectively record the relevant ion signal is needed. Using Labview, we create (in software) a time gate that allows us to record only those ions that arrive within the time width of the gate. We set a 700 ns wide gate centered on the $LiRb^+$ arrival time. The gate, along with the trigger that fires the Nd:YAG pulses, are derived from the same clock signal to ensure synchronization between the ionizing pulse and the recorded ion signal. We have incorporated this trigger and time gating into Labview programs to record

ionization spectra while scanning either the PA laser or the pulsed dye laser. Details of these Labview programs can be found in the thesis of John Lorenz.

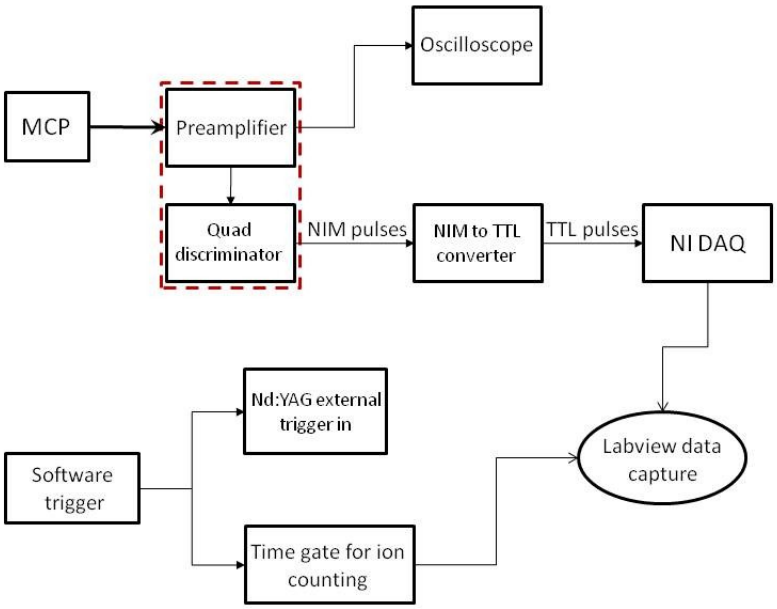

Figure 2.15. Setup for ion detection and counting. The MCP current output is converted into an amplified voltage signal using the preamplifier, and sent to a monitoring oscilloscope and a discriminator. The NIM output of the discriminator is converted into TTL signal for the National Instruments DAQ hardware. For gated ion counting, a software clock triggers the Nd:YAG pulse firing and also produces a time gate at the $LiRb^+$ arrival time. The gated ion signal is recorded using Labview programs.

With this setup we record individual ions incident on the MCPs, where each event produces a ~5 ns pulse width voltage signal as seen on the oscilloscope. At the field plate voltages mentioned above, the expected arrival times for the four ion species are listed in Table 2.3. Figure 2.16(a) shows a sample TOF signal showing Rb^+ and $LiRb^+$ ions recorded over 100 ionization laser

pulses. Also shown in Figure 2.16(b) is the averaged TOF trace that we use to determine the FWHM ion spread, Δt. From the fitted Gaussian, $\Delta t(Rb^+) = 110$ ns, and $\Delta t(LiRb^+) = 125$ ns.

Table 2.3 TOF for the four ion species present in our system. The arrival times are referenced to the rising edge trigger of the YAG pulses.

Ion species	TOF (μs)
$^7Li^+$	5.8
$^{85}Rb^+$	20.1
$^7Li^{85}Rb^+$	20.9
$^{85}Rb_2^+$	28.4

Search for the $LiRb^+$ signal was conducted by fixing the PA laser (Ti:S) frequency at a known PA resonance (from trap-loss spectroscopy) and scanning the dye laser. We confirmed that the signal originated from ionization of photoassociated LiRb molecules by i) blocking the PA laser, ii) blocking the Li MOT beam only, and iii) blocking the Rb MOT beam only. The Rb^+ signal persisted for the first two cases but vanished without the Rb MOT present. The $LiRb^+$ signal was absent in all three cases.

Having presented details of the experimental setup, we discuss PA spectroscopy studies using ionization detection in the next chapter.

2.13 Conclusion

In this chapter we have presented various aspects of our experimental setup, starting with the diode lasers used to cool and trap Li and Rb atoms. We describe our MOT optical table layout and features of our main experimental chamber, including the ion detection setup. In Chapter 3, we present PA spectroscopy studies performed on our apparatus.

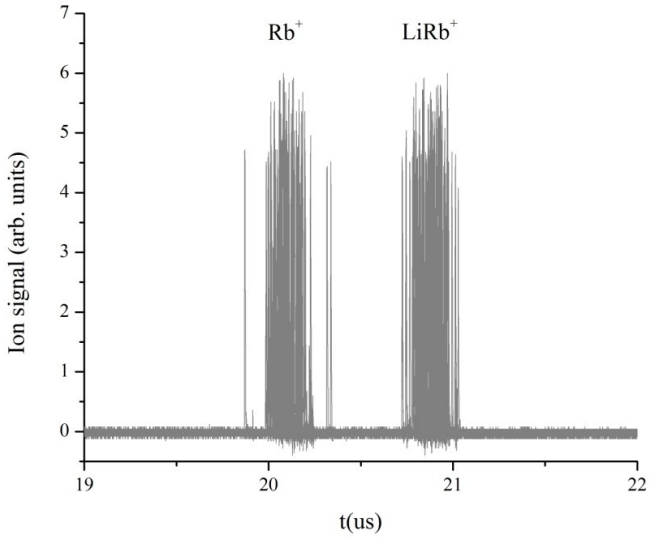

(a)

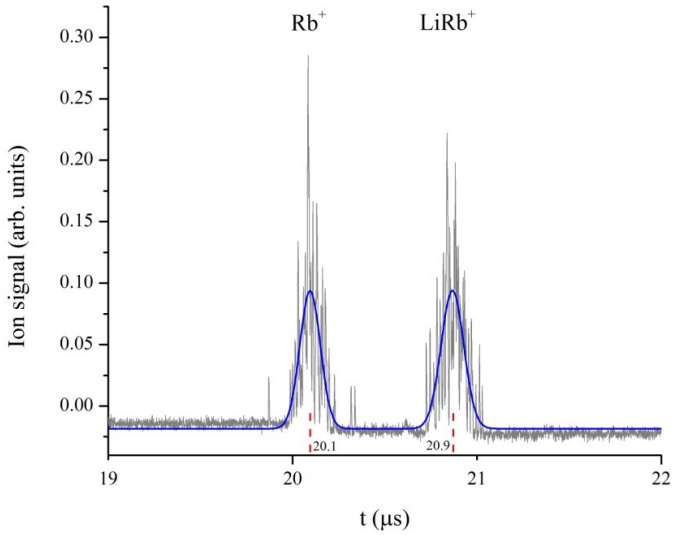

(b)

Figure 2.16 (a) Rb^+ and $LiRb^+$ TOF data recorded for 100 ionizing pulses. (b) Average of the data shown in (a). This plot is used to calculate the FWHM time spread Δt of the signal. Compared to the respective arrival times, the ion spread is sufficiently narrow to clearly differentiate signal originating from the two ion species. The Li^+ (Rb_2^+) ions arrive much earlier (later) and fall outside the display range shown here.

3. PA RESONANCES VIA IONIZATION SPECTROSCOPY

This chapter builds on earlier PA experiments conducted in our lab using the complementary trap-loss spectroscopy approach. We verify with ion detection the majority of PA resonances observed in trap-loss for electronic states asymptotic to Li(2s) + Rb($5p_{1/2}$) and Li(2s) + Rb($5p_{3/2}$) and obtain similar line positions and line features. In addition we observe new, more deeply bound PA lines that expand our knowledge of excited state potentials. From these new lines, we refine the long-range C_6 dispersion coefficients that can be used to extrapolate PA line positions at larger binding energies. We also resolve rotational structure of the $2(0^-)$ $v = 8$ level with ion detection, and use this information to calculate the outer turning point. This calculation is useful to determine classical turning points of vibrational levels, which in turn give an indication of ground and excited state wavefunction overlap. We compare the PA lineshape of the $2(0^-)$ $v = 8$, $J = 1$ resonance with a theoretical model that calculates the collision energy of atoms in the scattering state [67], and hence gives us an upper limit of our MOT temperature as ~1.1 mK. We demonstrate trapping of ground triplet molecules in the MOT magnetic field, and conclude the chapter by calculating PA molecule formation rate R_{PA} using ion detection parameters. These new observations further shed light on our MOT operation, ion detection system, and the energy level structure of LiRb molecules, and will be important for future identification of schemes to create LiRb molecules in the ground rovibronic state.

We start the chapter with the *ab initio* potential energy curves that are involved in the LiRb PA process.

3.1 Molecular potentials relevant for PA

Figure 3.1 shows the ground and excited state PECs that dissociate to the Li(2s) + Rb($5p_j$) asymptotes ($j = 1/2$ and $3/2$) and labeled according to Hund's case (a) notation, valid in the region of short internuclear spacing. Ultracold Li and Rb atoms approach each other along the Li(2s) + Rb(5s) asymptote and collide in the presence of a light field resonant with an excited

state rovibrational level. As mentioned in Chapter 1, PA occurs at large internuclear spacing – $R \gtrsim 20a_0$ (~ 11 Å) – where the overlap between the initial scattering state wavefunction and the excited state molecular wavefunction is large (Figure 3.2). At this and larger spacing the states are described by Hund's case (c) notation, as shown in Figure 3.3. After PA, the highly excited LiRb* molecules may undergo spontaneous emission and decay to the ground singlet and triplet electronic states to form more tightly bound LiRb molecules.

The long-range excited state interaction for heteronuclear molecules goes as $-C_6/R^6$, which is shorter range compared to the R^{-3} behavior of excited state homonuclear molecules. The difference in interaction strength is reflected in the different values of the Condon point, R_C, defined as the internuclear spacing (corresponding to the outer turning point of the PA vibrational level) at which the PA laser is resonant with the free-bound transition. R_C is larger ($> 100a_0$) for homonuclear molecules than heteronuclear molecules ($< \sim 50a_0$ for LiRb), which results in a larger wavefunction overlap for the former and therefore a more efficient PA process. On the other hand, the similar R-dependence of the ground and excited states for heteronuclear molecules allows favorable spontaneous decay to more deeply bound ground state levels. This characteristic is relevant to our eventual goal of transferring PA molecules to the ground rovibronic state. For a more detailed comparison between homonuclear and heteronuclear molecules, see [17, especially Table 5.2].

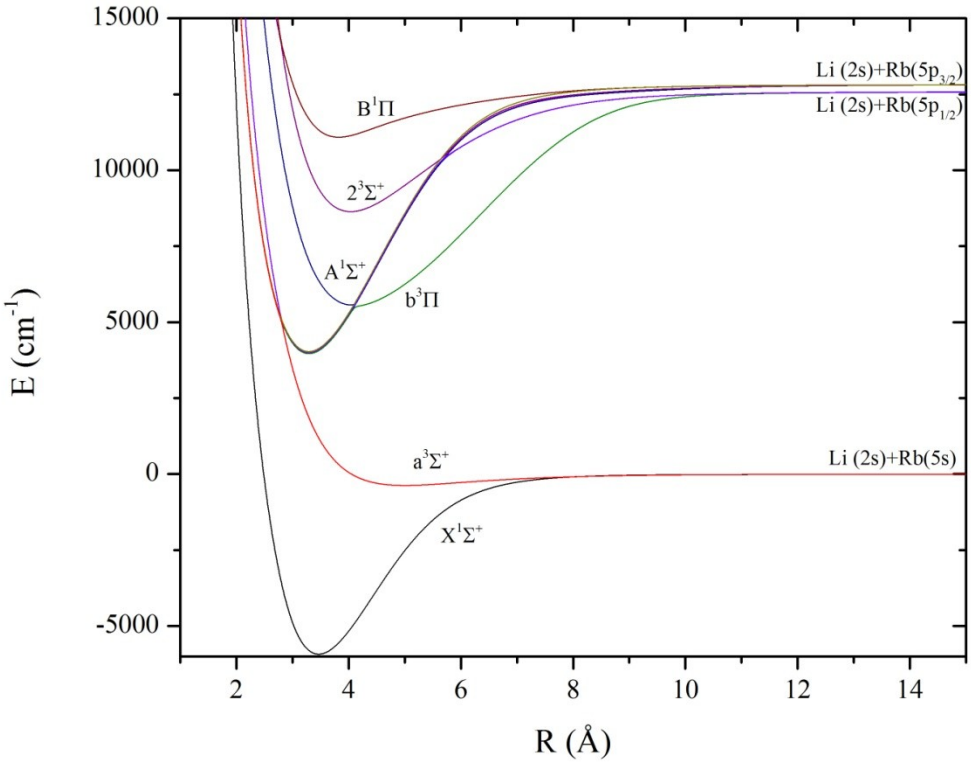

Figure 3.1. LiRb *ab initio* ground- and excited-state PECs [50]. Our PA step creates LiRb* molecules in states asymptotic to the Li(2s) + Rb($5p_{1/2}$) and Li(2s) + Rb($5p_{3/2}$) levels.

3.2 Experimental setup

We start with a Li MOT with ~5×10^7 atoms and a density of ~5×10^9 cm^{-3}. Li atoms predominantly occupy the $F = 2$ upper hyperfine level of the ground 2s state. The Rb MOT traps ~10^8 atoms at a density of ~4×10^9 cm^{-3}. For the data presented in this chapter, we use a dark-SPOT Rb MOT, unless otherwise specified. In this mode of operation the majority of Rb atoms populate the $F = 2$ lower hyperfine level of the ground 5s state. During data acquisition, the operation and overlap of both MOTs is monitored using CCD cameras and photodetectors that record the Li and Rb MOT fluorescence. The PA laser is the cw Ti:S mentioned in Chapter 2, with an output power between 300 and 350 mW and a collimated beam diameter of ~0.85 mm. The laser linewidth is ~1 MHz when locked to the external reference cavity. The laser has a

mode-hop free scan range of 20 GHz, and its frequency is monitored with a wavemeter (Bristol 621A) that is accurate to within 60 MHz.

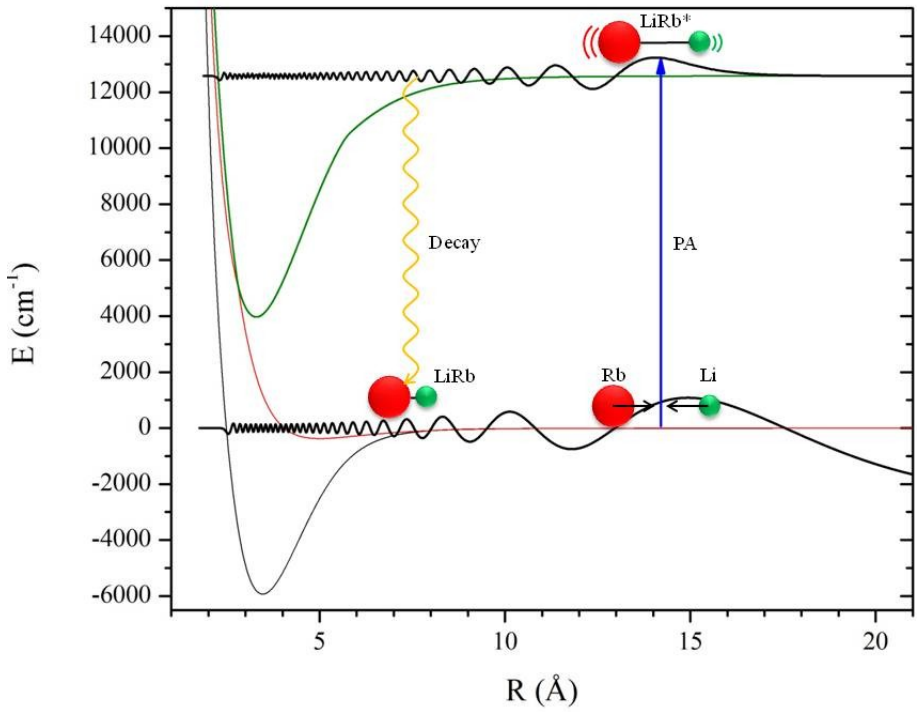

Figure 3.2. Overlap between the initial scattering-state wavefunction of Li and Rb atoms, and the final bound state wavefunction of LiRb*. PA molecules are created at large internuclear distances and undergo spontaneous emission to populate high-lying vibrational levels of the ground electronic states. Wavefunction calculations courtesy of Jesús Pérez-Ríos.

The Spectra-Physics PDL-2 is pumped by the second harmonic of a pulsed Nd:YAG laser which fires ~7 ns pulses at a 10 Hz repetition rate. We use Rhodamine 590 dye for the PA spectroscopy presented in this chapter, with a maximum energy of ~ 4 mJ per pulse. R590 is a high-gain, long lifetime dye that lases between 554 nm (~18050 cm^{-1}) and 580 nm (~17250 cm^{-1}).

Our data acquisition hardware does not differentiate between the different ion species, which is required to count only $LiRb^+$ (for details of acquiring the ion signal, see Chapter 2). Instead, we use Labview to detect $LiRb^+$ within a user-specified gated time window. The rising edge of the software gate is synchronized with an external clock signal that also triggers the YAG pulses. A

Labview data acquisition program counts the total number of ions arriving in a time-gated window for a specified number of ionization pulses. The program also changes the PA laser frequency in discrete, user-defined frequency steps, also in synchrony with the clock signal. For PA spectroscopy presented in this chapter, we count the total number of $LiRb^+$ ions for 100 pulses, and step the Ti:S frequency in discrete ~20 MHz steps. The PDL wavelength is held constant throughout the scan, while the Ti:S frequency is monitored using a Bristol 621A wavemeter. With these experimental parameters, we record the PA spectra shown in the next section.

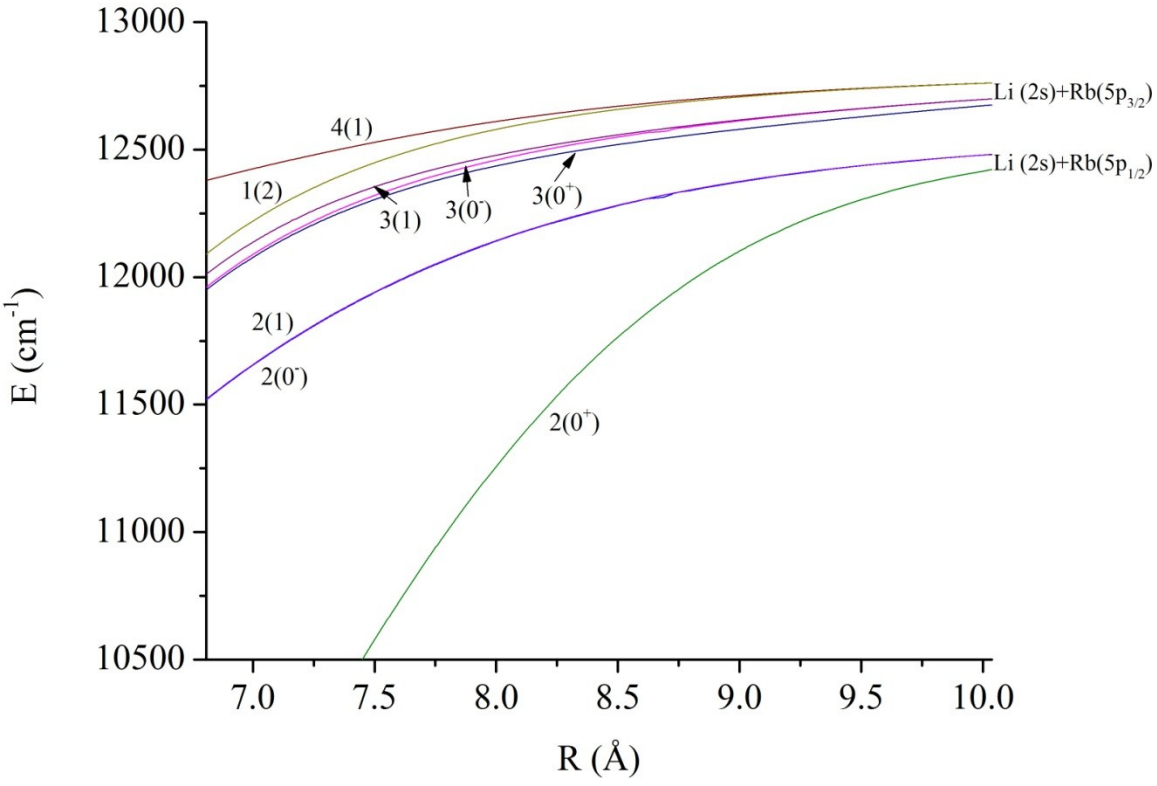

Figure 3.3. LiRb Hund's case (c) potentials involved in PA spectroscopy [50]. The $2(0^-)$ and 2(1) states are indistinguishable from each other on this scale.

3.3 LiRb PA

In this section we present results of PA spectroscopy using ionization detection and compare these results with earlier trap-loss spectroscopy, including PA line positions and features. We also

identify new lines detected using ionization spectroscopy. Based on the additional PA resonances, we determine that the long-range C_6 dispersion is valid for extrapolating PA line positions at the largest observed detuning $\Delta_{PA} \sim$ -62 cm^{-1} below Li(2s) + Rb($5p_{1/2}$), which suggests that we are still probing long-range excited state vibrational levels.

3.3.1 Trap-loss spectroscopy

Heteronuclear PA of $^7Li^{85}Rb$ was first observed in our lab using trap-loss spectroscopy [56]. With this detection method, we have observed $3(0^+)$ $v = 3 – 5$, $4(1)$ $v = 2 – 6$ and $1(2)$ $v = 2 – 4$ levels. These electronic states are asymptotic to Li(2s) + Rb($5p_{3/2}$). For the $2(0^+)$, $2(0^-)$ and $2(1)$ states asymptotic to Li(2s) + Rb($5p_{1/2}$), trap loss spectroscopy has revealed $v = 2 – 4$, $3 – 5$ and $3 – 5$ levels, respectively. Note that in this thesis, PA vibrational level labeling starts at $v = 1$ for levels closest to the dissociation limit, and the numbering increases for more deeply bound levels. All other ground and excited state vibrational level numbering starts from $v = 0$ for the deepest bound level.

3.3.2 $LiRb^+$ detection

Trap-loss spectroscopy can help identify PA levels close to the dissociation limit. However, as the PA laser is scanned towards more deeply bound vibrational levels, the trap-loss signal decreases and we cannot distinguish PA resonances from the background MOT fluorescence. In contrast, ionization detection records events arising out of a (near) zero background and can identify weaker signal that cannot be observed with trap-loss. For a suitably chosen ionization pathway, ion counting can readily identify PA resonances at large binding energies of tens to hundreds of cm^{-1}.

Whereas PA trap-loss spectroscopy has one adjustable parameter in the form of the PA laser frequency, PA ionization detection is a ‘two-dimensional’ search, i.e. we need to know a PDL wavelength at which LiRb molecules can be resonantly ionized, and we must also scan the PA laser in search of a free-bound transition. To simplify the initial search for $LiRb^+$, we started by fixing the PA laser at the strongest observed trap-loss transition, the $3(0^+)$ $v = 3$ at a binding energy $\Delta_{PA} = –15.08$ GHz from the Li(2s) + Rb($5p_{3/2}$) asymptote. We scanned the PDL for the entire dye lasing range, but were unable to detect $LiRb^+$ signal. We noted that the MCP assembly detected Rb^+, which led us to conclude that the ion detection was operating normally. Due to reasons mentioned later in this chapter, it turned out that our choice of PA resonance was an ill-

advised one. Our next attempt was more successful with the PA laser fixed on the 4(1) $v = 3$ resonance. Next, we optimized MOT parameters to maximize $LiRb^+$ counts. These are listed in Table 3.1. We also saw a significant improvement in signal by carefully positioning a set of permanent magnets on the outer wall of the field-free region to steer the ions towards the MCP assembly.

With the ion signal optimized, we proceeded to record PA spectra.

Table 3.1 List of MOT parameters that optimize ion detection.

	detuning δ (MHz)	Intensity (mW/cm^2)
Rb trap beam	-19	32
Rb repump beams	+12	8
Li cooling and repump beam	-25	14
Li Zeeman slower beam	-80	7

3.4 PA ionization spectroscopy below Li(2s) + Rb($5p_{3/2}$)

Figure 3.4 shows PA spectra observed via ionization detection while tuning the PA laser below the Li(2s, $F = 2$) + Rb ($5p_{3/2}$, $F = 2$) asymptote at $v_{3/2}$ = 384232.157 GHz. In this section, the binding energy Δ_{PA} is defined as the PA line position (in GHz) below $v_{3/2}$. We compare Δ_{PA} with previous trap-loss spectra to corroborate the line assignment. We have labeled the lines in Figure 3.4 as belonging to either the 4(1) or 1(2) states, with the vibrational level numbering beginning with $v = 1$ for the least bound level. The 4(1) PA resonances show the $J = 1$ and 2 rotational levels, whereas for the 1(2) level, we observe only one rotational line, which is assigned as $J = 2$ [68]. For PA detuning less than ~8 GHz below dissociation, the Rb MOT is significantly perturbed and we do not detect PA lines beyond this detuning. The list of Δ_{PA} is given in Table 3.2, and the individual resonances are shown in Figure 3.5. Here we label the PA levels of the different electronic states, as well as multiple rotational lines of the 4(1) state. All of the 1(2) lines are $J = 2$. Note that not all the spectra are recorded for the same PDL wavelength. The ionization pathways are not identical for all lines for two reasons: i) the wavefunction overlap between the PA level and ground vibrational levels varies as we scan farther below $v_{3/2}$, which influences the ground state population distribution and hence the ion signal, ii) based on selection rules, PA levels can populate either the ground singlet or triplet state. From this singlet or triplet state,

selection rules also govern which excited state can be accessed for the resonantly enhanced multiphoton ionization (REMPI) process. This may require adjusting the REMPI wavelength from one PA resonance to the next. These arguments also apply in the next section to PA spectra for states asymptotic to Li(2s) + Rb($5p_{1/2}$). We list the REMPI wavelengths for each PA line in Figure 3.5.

Table 3.2. Binding energies Δ_{PA} (in GHz) for the observed PA levels below Li(2s) + Rb($5p_{3/2}$), measured with respect to $v_{3/2}$. The 4(1) v = 5 lines are only observed with ionization detection.

v	4(1) J = 1	4(1) J = 2	1(2) J = 2
2	-10.74	-9.61	-7.93
3	-42.36	-40.70	-36.08
4	-107.53	-105.40	-97.62
5	-217.81	-214.90	-205.54
6			-373.06

Once we confirmed the PA line assignments obtained by ionization detection with earlier trap-loss results, we started a systematic search for PA resonances that could not be observed with trap-loss. When searching for new lines, one approach is to fix the PDL wavelength while continuously scanning the PA laser. Assuming all components of the experiment run smoothly, this approach generates continuous spectra spanning tens to hundreds of GHz (see, for example [35]. Unfortunately, for reasons explained earlier, we cannot run our system uninterrupted for more than an hour. To make the most efficient use of the apparatus, we follow a different route. We calculate the C_6 coefficient using the known PA lines for a particular electronic state and extrapolate the position of the next PA line in the series to within ~10 GHz (details of C_6 calculations are explained below). Upon observing the next level in the progression, we recalculate the C_6 coefficient and extrapolate the position of the next line, and so on. We focused our search using this method and discovered the v = 5, J = 1 and J = 2 levels of the 4(1) state[1] (Figure 3.5).

[1] This extrapolation method will become less accurate for larger binding energies as the vibrational level spacing deviates from the prediction based on the long-range C_6 coefficient. For all of the PA resonances reported in this chapter, however, this method predicts line positions fairly well.

3.4.1 Comparison between ionization and trap-loss spectra

Except for the 4(1) $v = 5$ lines, the PA resonances shown in Figure 3.5 have been previously observed with trap-loss spectroscopy. We note that the line positions in ion detection are similar to the trap-loss lines to within ~40 MHz. As mentioned in Section 3.2, the Bristol wavemeter used to measure the PA laser linewidth is accurate to ~60 MHz. In addition, the hyperfine structure seen in both detection schemes is qualitatively similar. We do not attempt to compare signal strength because the ion signal is dependent on ionization efficiency of ground state molecules via the intermediate excited state. By contrast, trap-loss spectroscopy measures change in MOT fluorescence as trapped atoms are lost via PA.

Comparison of ion detection with trap-loss spectra reveals a further important difference. Several vibrational levels belonging to the $3(0^+)$ state were observed with trap-loss, but they are all absent from the ionization spectra. The reason these lines are absent in the ionization spectrum is most likely due to predissociation of the $3(0^+)$ state. Korek et.al. have reported an avoided crossing between the $2(0^+)$ and $3(0^+)$ states that correlate at short range to the $A^1\Sigma^+$ and the $b^3\Pi$ states [50]. Molecules that photoassociate to a $3(0^+)$ level may predissociate via the lower energy Li(2s) + Rb($5p_{1/2}$) asymptote and decay to Li and Rb atoms instead of forming ground state molecules. Since trap-loss spectroscopy cannot differentiate between excited state molecules decaying to two free atoms or bound ground state molecules, either process results in a decrease in MOT fluorescence, and we detect the $3(0^+)$ lines. The initial state for ionization detection, however, is the molecular ground state, which in this case seems to be thinly populated and explains the absence of ion signal.

In the next section, we discuss PA spectroscopy for electronic states that are asymptotic to the Li(2s) + Rb ($5p_{1/2}$) level.

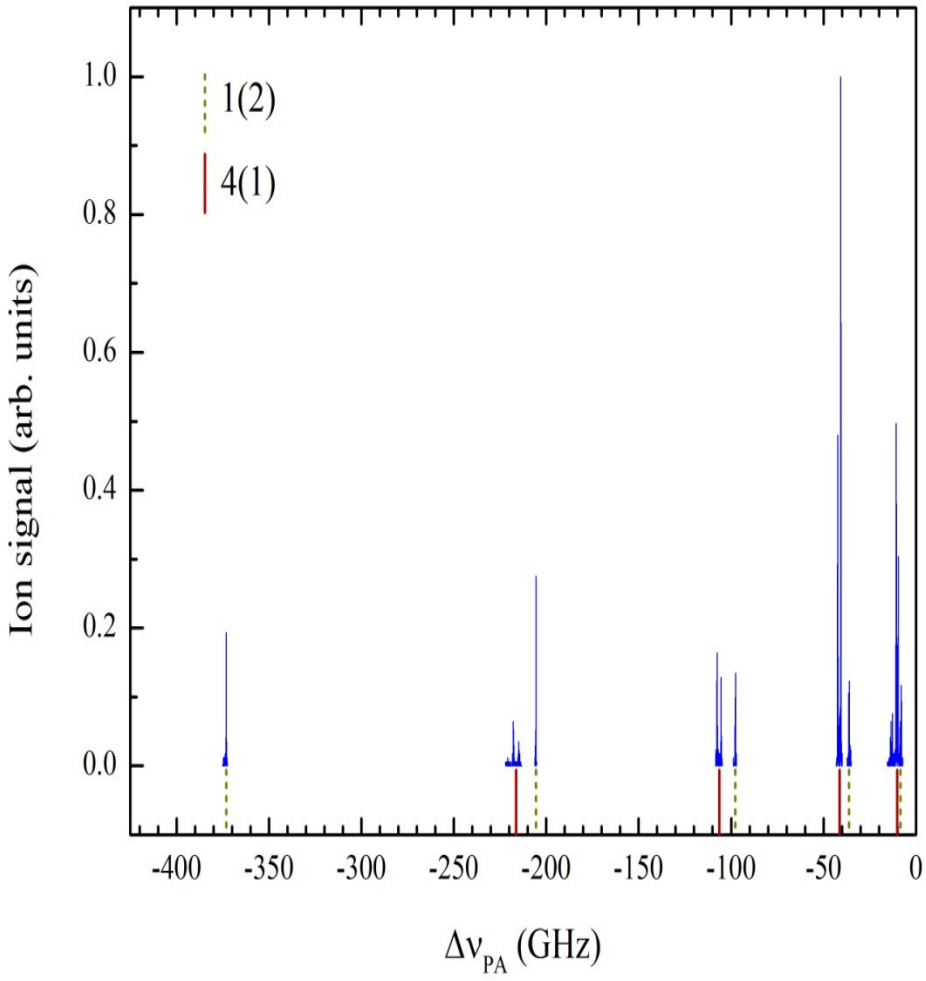

Figure 3.4. Global view of PA resonances observed below Li(2s) + Rb($5p_{3/2}$) with ionization spectroscopy.

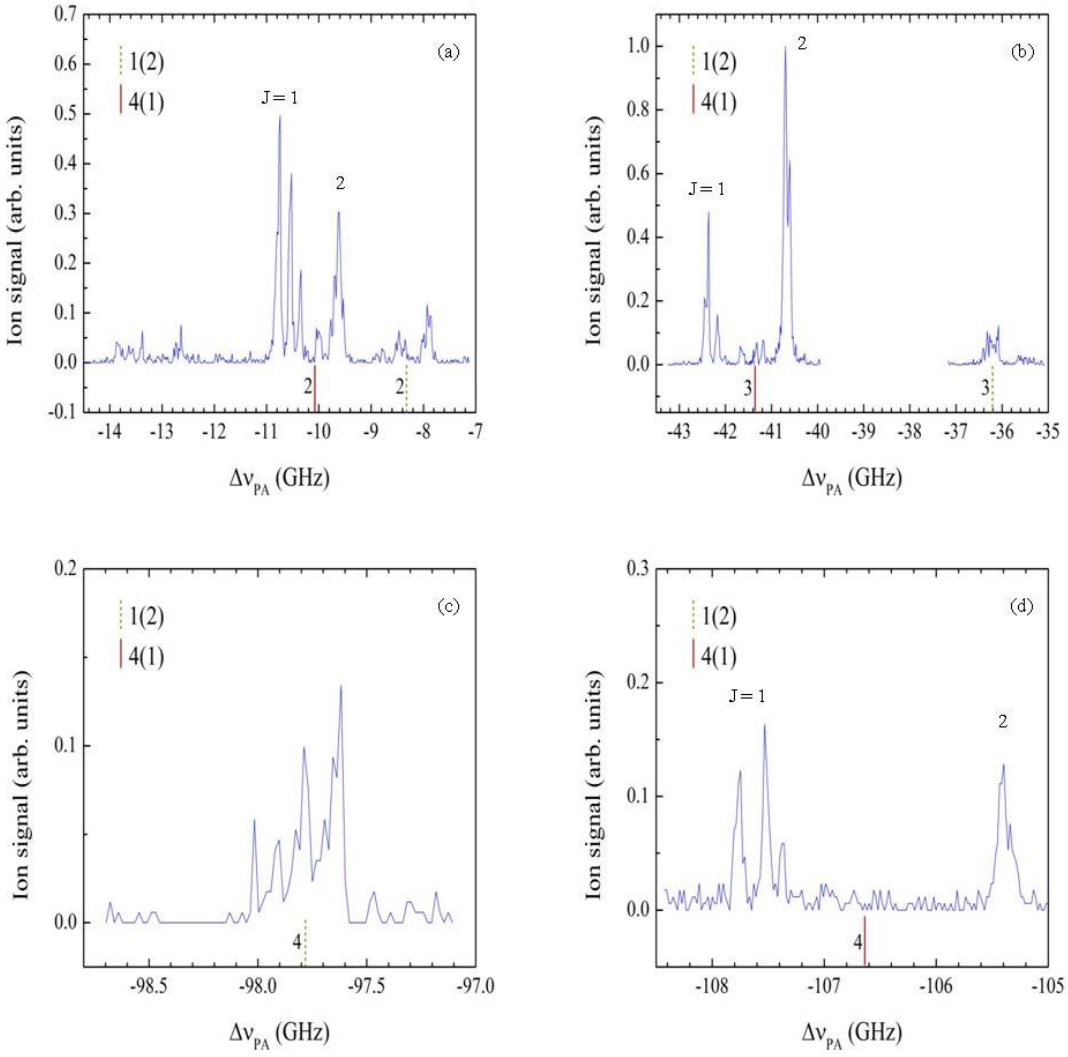
(a)
1(2)
4(1)
J = 1
2
2
2
Ion signal (arb. units)
Δν_PA (GHz)
(b)
1(2)
4(1)
J = 1
2
3
3
Ion signal (arb. units)
Δν_PA (GHz)
(c)
1(2)
4(1)
4
Ion signal (arb. units)
Δν_PA (GHz)
(d)
1(2)
4(1)
J = 1
2
4
Ion signal (arb. units)
Δν_PA (GHz)

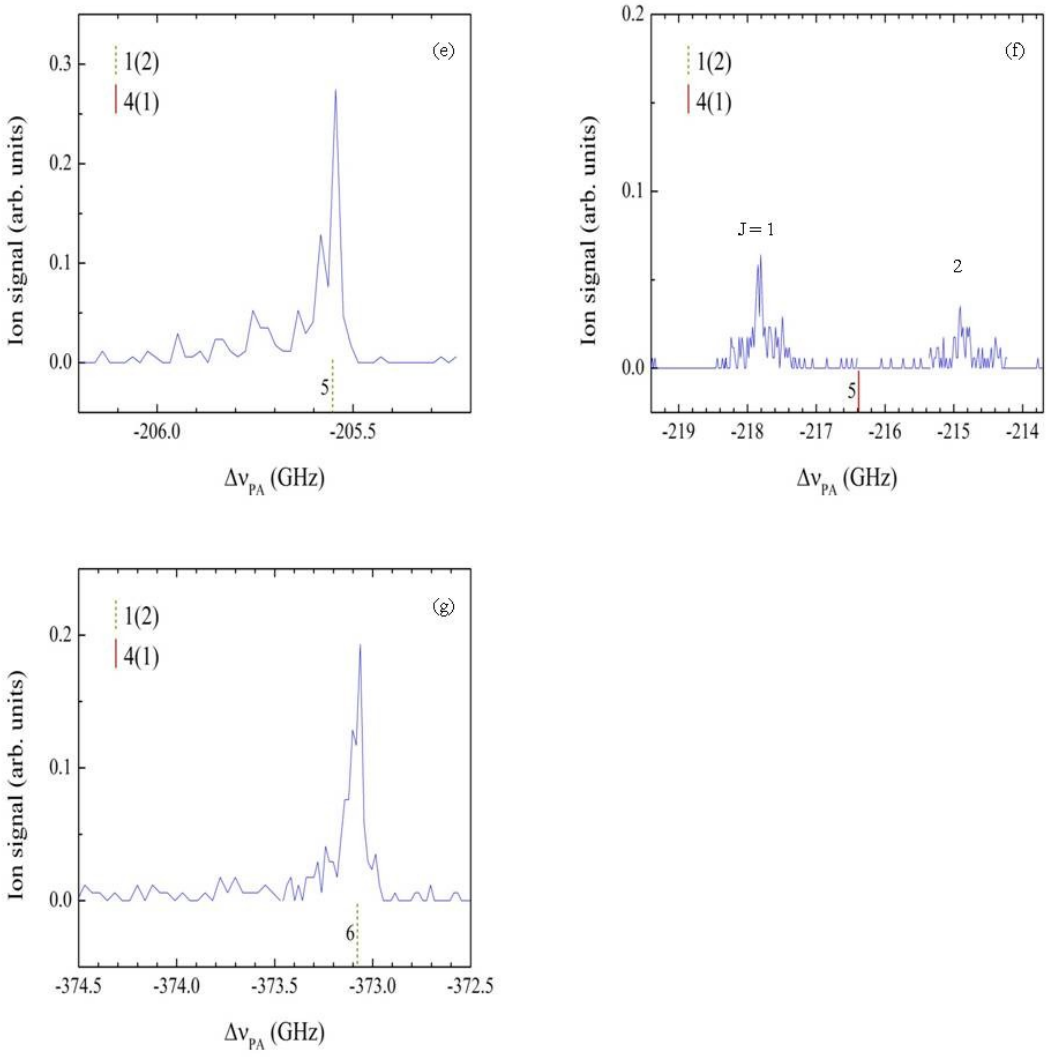

Figure 3.5. (a-d) (Previous page) and (e-g) show the individual PA resonances for the 4(1) and 1(2) states. The number next to the vertical solid and dashed line below PA lines denotes the PA vibrational level of the 4(1) and 1(2) states, respectively (legend shown in each panel). The smaller features in each figure are due to the molecular hyperfine energy. Multiple rotational levels are labeled where observed. The ionization laser wavelengths are as follows: (a) and (b) 17826.8 cm^{-1}, (c) and (e) 17605.5 cm^{-1}, (d) and (f) 17633.1 cm^{-1}, and (g) 17782.1 cm^{-1}. The 4(1) $v = 5$ $J = 1$ and 2 lines have only been observed with ionization spectroscopy.

3.5 PA spectroscopy below Li(2s) + Rb ($5p_{1/2}$)

The procedure is similar to that followed in the previous section, except we now scan the PA laser below the ^{85}Rb $5p_{1/2}$ asymptote. All the PA line positions Δ_{PA} in this section are measured as detuned from the ^{85}Rb (2s, $F = 2$) – ^{85}Rb ($5p_{1/2}$, $F = 2$) transition at $\nu_{1/2}$ = 377108.946 GHz. Li and Rb MOT parameters are also identical for both sets of PA scans. Figure 3.6 shows all of the observed PA resonances, with individual lines shown in Figure 3.7. Unlike the search for PA lines below Li(2s) + Rb($5p_{3/2}$), we observe and assign resonances to all three electronic states [$2(0^+)$, $2(0^-)$ and 2(1)] asymptotic to this level. For $\Delta_{PA} \sim 8$ GHz or less below dissociation, the Rb MOT is disrupted similar to the behavior below Li(2s) + Rb($5p_{3/2}$), and we do not observe PA resonances in this range. As with trap-loss spectroscopy, we only observe one rotational level for most of the PA resonances and assign these as $J = 1$ based on similar arguments as for the rotational level assignments in trap-loss spectra [69]. REMPI wavelengths used to acquire these spectra are given in Figure 3.7.

In trap-loss spectroscopy we observed $v = 2 – 4$ of $2(0^+)$ and $v = 3 – 5$ of $2(0^-)$ and 2(1). In addition to detecting these lines with ion detection, we also show $v = 5$ of $2(0^+)$, $v = 8$, 9 and 11 of $2(0^-)$ and $v = 6$, 7 and 10 of 2(1) (details of peak assignment are given in the next section). For peaks that appear in both detection schemes, we again note that the line positions in trap-loss spectra are within ~40 MHz of the line positions in ion detection. We also observe similar hyperfine structure in both sets of spectra.

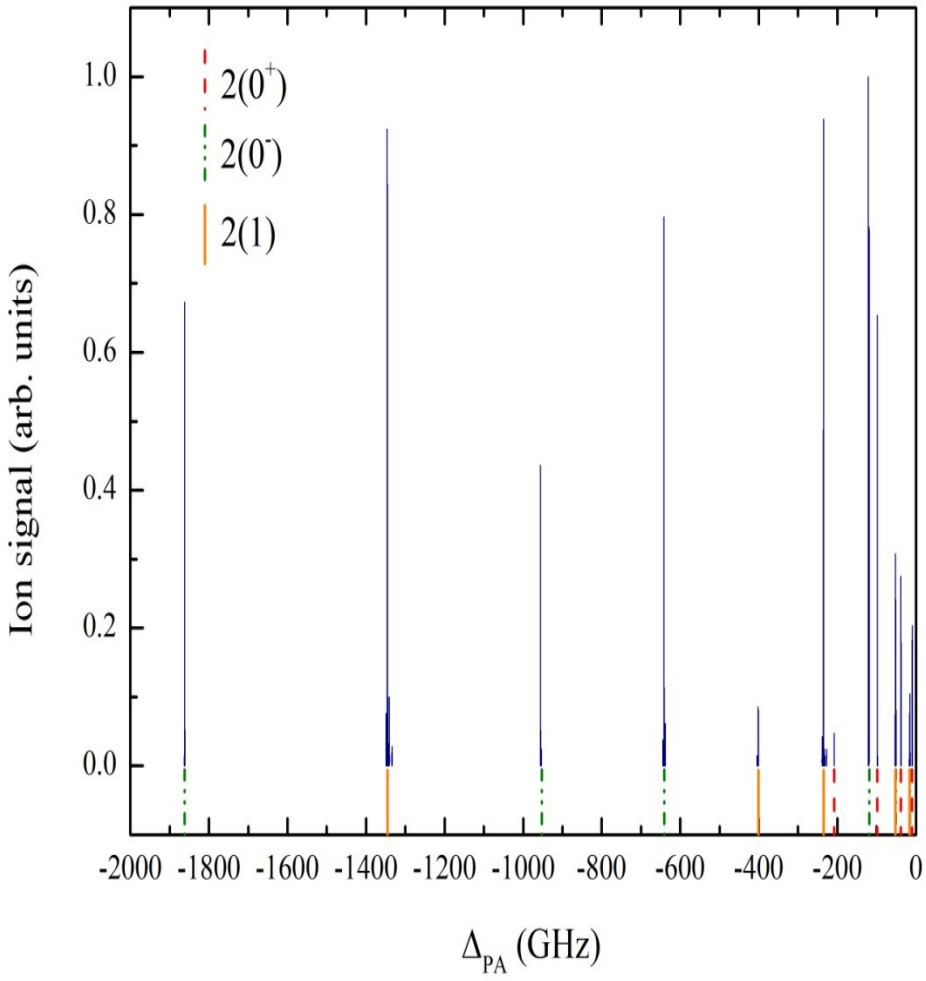

Figure 3.6. Global view of PA resonances observed below Li(2s) + Rb($5p_{1/2}$) with ionization spectroscopy.

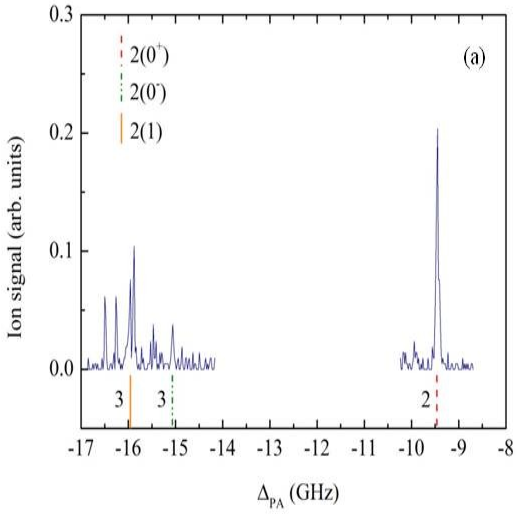
(a)
2(0+)
2(0-)
2(1)
Ion signal (arb. units)
0.3
0.2
0.1
0.0
3
3
2
-17 -16 -15 -14 -13 -12 -11 -10 -9 -8
ΔPA (GHz)

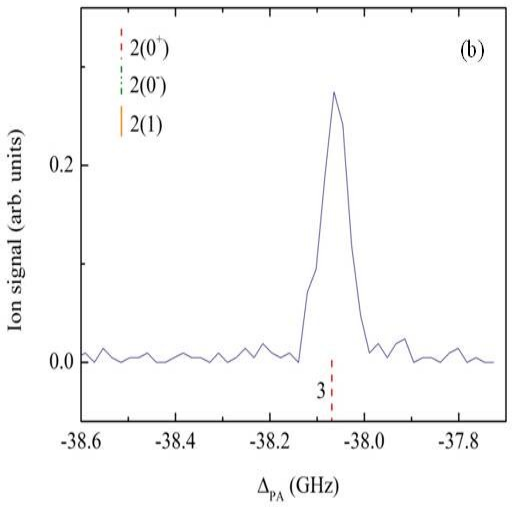
(b)
2(0+)
2(0-)
2(1)
Ion signal (arb. units)
0.2
0.0
3
-38.6 -38.4 -38.2 -38.0 -37.8
ΔPA (GHz)

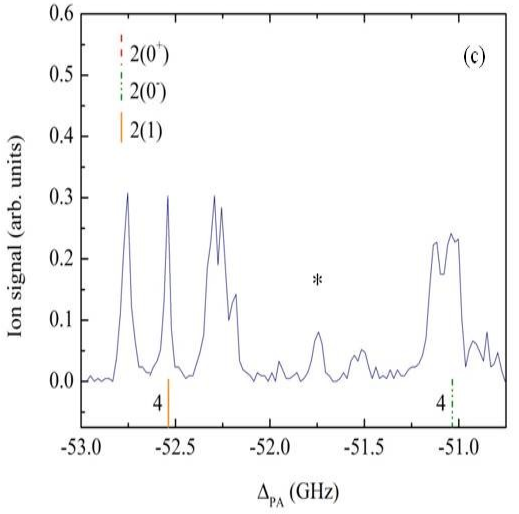
(c)
2(0+)
2(0-)
2(1)
Ion signal (arb. units)
0.6
0.5
0.4
0.3
0.2
0.1
0.0
*
4
4
-53.0 -52.5 -52.0 -51.5 -51.0
ΔPA (GHz)

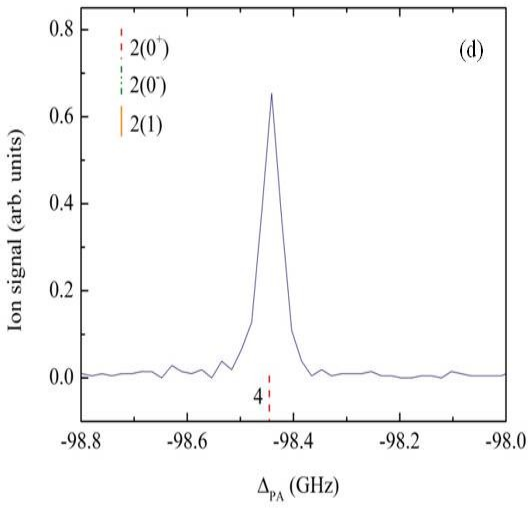
(d)
2(0+)
2(0-)
2(1)
Ion signal (arb. units)
0.8
0.6
0.4
0.2
0.0
4
-98.8 -98.6 -98.4 -98.2 -98.0
ΔPA (GHz)

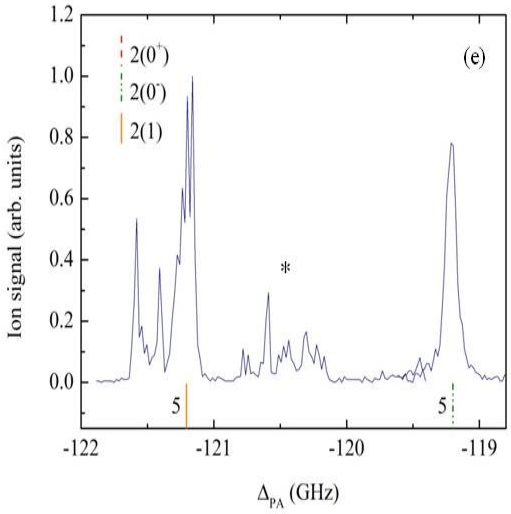
(e)
2(0+)
2(0-)
2(1)
*
5
5
Ion signal (arb. units)
ΔPA (GHz)

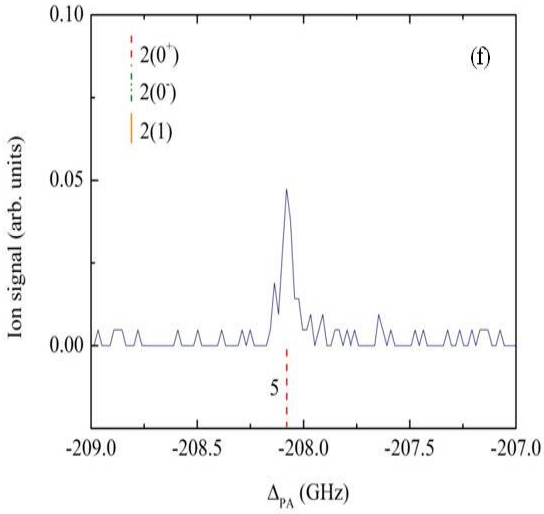
(f)
2(0+)
2(0-)
2(1)
5
Ion signal (arb. units)
ΔPA (GHz)

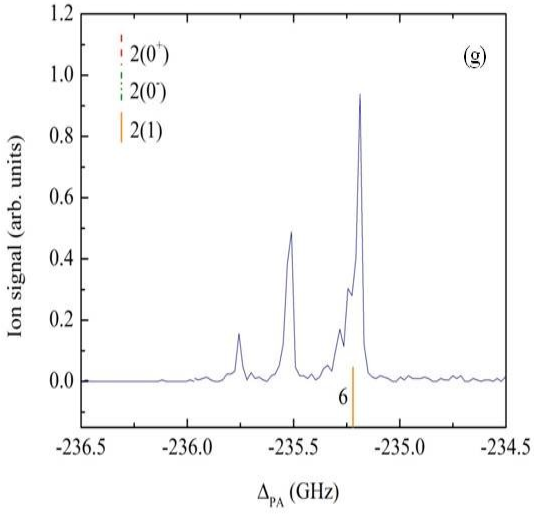
(g)
2(0+)
2(0-)
2(1)
6
Ion signal (arb. units)
ΔPA (GHz)

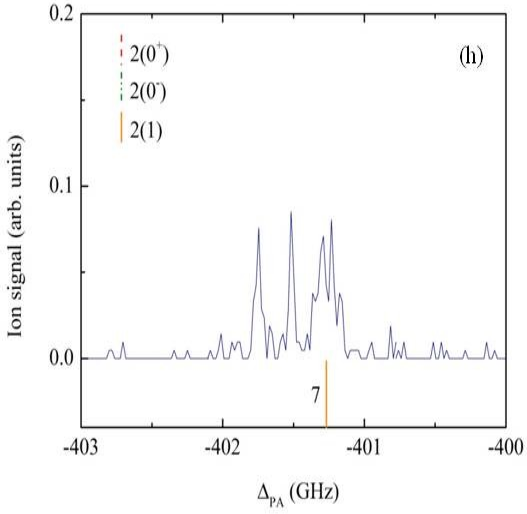
(h)
2(0+)
2(0-)
2(1)
7
Ion signal (arb. units)
ΔPA (GHz)

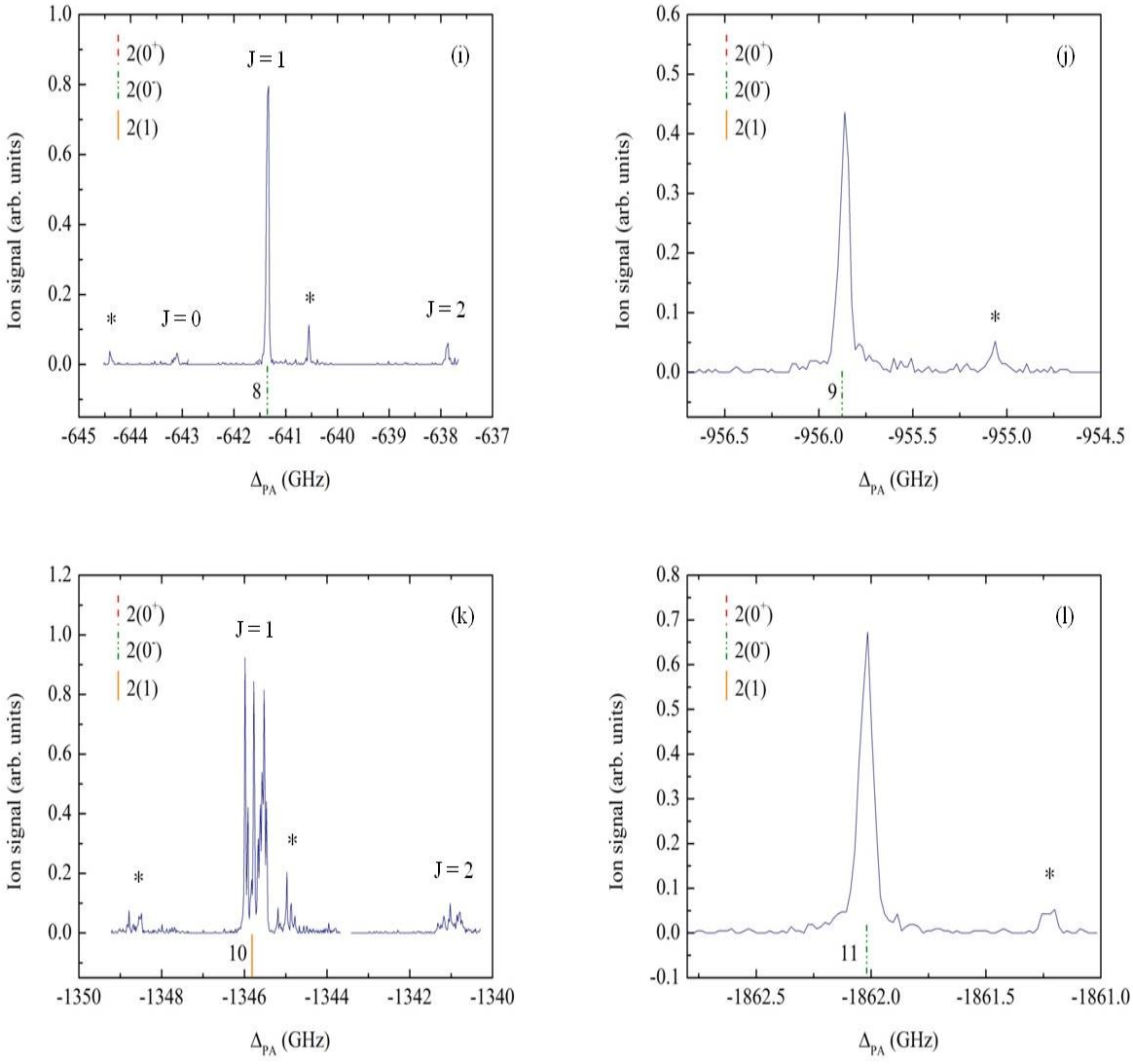

Figure 3.7. (a-h) (previous two pages) and (i-l) show the individual PA resonances for the $2(0^+)$, $2(0^-)$ and 2(1) states. Each PA vibrational level v is labeled below the respective resonance. Line features in panels (a), (c), (e), (g), (h) and (k) are due to molecular hyperfine energy. Multiple rotational levels are labeled where observed. Note that the $\Omega = 0$ lines show no hyperfine structure as expected. The asterisks (*) label hyperfine ghosts originating from population in the Rb(5s, $F = 3$) and Li(2s, $F = 1$) states. The ionization laser wavelengths are: (a) – (h) 17742.4 cm^{-1}, (i) – (k) 17602.5 cm^{-1} and (l) 17612.7 cm^{-1}.

3.5.1 Peak assignment

We assign electronic states to the PA levels by looking for patterns in the structure of the PA resonances. The hyperfine energy, E_{hfs}, goes as $E_{hfs} \sim \Omega/J(J+1)$ [39, 70]. Hence, $\Omega = 0$ lines have no internal structure to first order but $\Omega \geq 1$ lines show hyperfine structure. This pattern recognition procedure was used for the initial line assignment using trap-loss spectroscopy, and applies to ionization detection as well. Figure 3.7 shows the sets of peaks assigned to each of the three electronic states.

In contrast to the weak ion signal at larger detuning below the Li(2s) + Rb ($5p_{3/2}$) asymptote, we have good ion counts to detect PA resonances with a binding energy of up to $\Delta_{PA} \sim$ -62 cm^{-1} (~1862 GHz below $\nu_{1/2}$). Table 3.2 lists the observed PA lines for the $J = 1$ line of each vibrational level. As with PA spectra below Li(2s) + Rb($5p_{3/2}$), we do not observe sufficient rotational lines to determine B_v. The one exception is the $2(0^-)$ $v = 8$ level, where we observe $J =$ 0, 1 and 2 lines. We will return to the observed rotational structure later in the chapter.

The distinction between $\Omega = 0^{\pm}$ and $\Omega = 1$ peaks is clear. To differentiate between $\Omega = 0^+$ and $\Omega = 0^-$ lines, we compare the C_6 dispersion coefficients for each line progression. Experimental C_6 values are obtained using the LeRoy-Bernstein formula that describes the long-range potential of diatomic molecules where PA occurs [71]:

$$(D - E_v) = \left(\frac{2\sqrt{2}\pi\hbar}{B\left(\frac{2}{3},\frac{1}{2}\right)\sqrt{\mu}} \right)^3 \left(\frac{1}{\sqrt{C_6}} \right) (v - v_D)^3 \qquad (3.1)$$

μ is the reduced mass of $^7Li^{85}Rb$, $B(2/3,1/2)$ is the Beta function (= 2.5871), and $0 < v_D < 1$, determined experimentally. D is the dissociation energy, E_v is the energy of a PA vibrational level, and $(D - E_v) = -h\Delta_{PA} + E_{rot}$, where $E_{rot} = B_v[J(J+1) - \Omega^2]$ is the rotational energy for vibrational level v. J is the rotational level and B_v is the rotational constant. We plot $(D - E_v)^{1/3}$ against v, and use the slope to calculate C_6. Since we observe a single rotational level for the majority of PA levels, we use the scheme outlined in [68] to include estimates of E_{rot} in our calculation. However, as shown in the next section, the $2(0^-)$ $v = 8$ level shows multiple rotational lines from which we can calculate B_v and E_{rot}. This information is incorporated here to improve the $2(0^-)$ C_6 calculation. Figure 3.8 shows plots of $(D - E_v)^{1/3}$ versus v for all observed PA

resonances in our study, while Table 3.3 lists our calculated C_6 coefficients, along with earlier calculations based on trap-loss measurements [68, 69] and theory [72, 73]. The $2(0^+)$ and $2(0^-)$ states have significantly different C_6 values (also seen in Figure 3.8) that we can assign lines belonging to each state.

PA resonances up to $v = 5$ for all three electronic states were previously observed in trap-loss spectroscopy. We discovered the remaining peaks using the approach outlined in the previous section, i.e. we used the experimental C_6 values to extrapolate the position of the next PA line in each progression. This includes the PA level with the largest binding energy, $\Delta_{PA} \sim -62$ cm^{-1}, belonging to the $2(0^-)$ state, and indicates that the long-range behavior described by the van der Waals interaction is valid at this energy.

Having identified all observed PA resonances using ionization detection, we focus on the rotational structure of the $2(0^-)$ $v = 8$ line in the next section.

Table 3.2. Binding energies Δ_{PA} (in GHz) for the observed PA levels below Li(2s) + Rb($5p_{1/2}$), measured from $v_{1/2}$.

v	$2(0^+)$	$2(0^-)$	2(1)
2	-9.45		
3	-38.06	-15.48	-16.26
4	-98.44	-51.04	-52.54
5	-208.08	-119.21	-121.41
6			-235.51
7			-401.52
8		-641.33	
9		-955.86	
10			-1345.77
11		-1862.02	

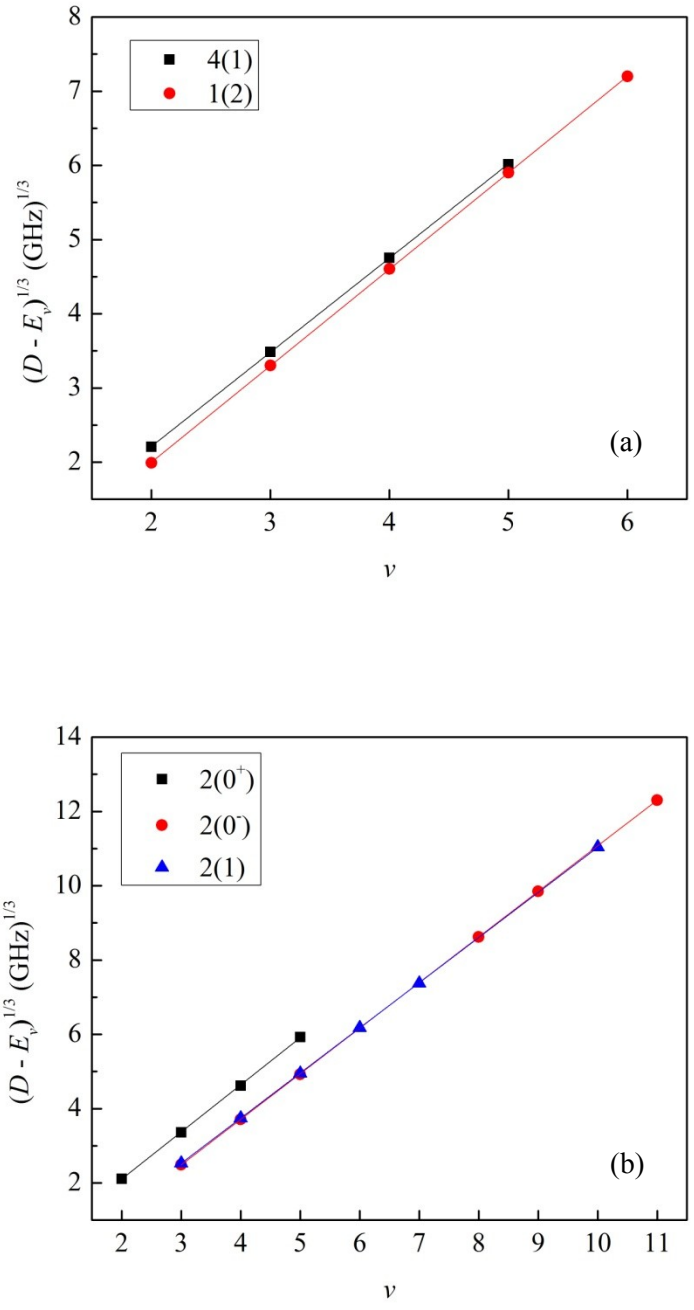

Figure 3.8. Plot of $(D - E_v)^{1/3}$ versus PA vibrational level v. (a) Black and red lines are fits of 4(1) and 1(2) levels to Eq. (3.1), respectively. (b) Black, red and blue lines are fits of the 2(0^+), 2(0^-) and 2(1) levels to Eq. (3.1), respectively.

Table 3.3. C_6 coefficients calculated from the fit of Eq. (3.1) to experimentally observed PA lines. These values are compared with earlier calculations based on trap-loss spectra, and also with two theory calculations. Uncertainties are given in parentheses, and all values are in a.u.

Electronic state	C_6 (this work)	C_6 (trap-loss [68, 69])	C_6 (theory [72])	C_6 (theory [73])
$2(0^+)$	10120 (450)	11335(+600, –300)	13900	16072
$2(0^-)$	12410 (180)	13470 (+540, –270)	13900	16071
2(1)	13130 (330)	13730 (+535, –270)	13900	16071
4(1)	8750 (500)	9235 (490)	9205	11308
1(2)	10070 (590)	10190 (420)	9205	11308

3.6. Rotational structure of $2(0^-)$ $v = 8$ PA resonance

LiRb PA is estimated to occur at internuclear spacing $R_C \sim 9.5 – 23.6$ Å (18 – 44.6 a_0) [56]. To get to R_C, the colliding atoms encounter the centrifugal barrier of the long-range potential due to rotational angular momentum l. The height of these barriers can be calculated using $C_6 = 2500$ a.u. for the Li(2s) + Rb(5s) collision channel [73]:

$$V(R) = -\frac{C_6}{R^6} + \frac{\hbar^2}{2\mu}\frac{l(l+1)}{R^2} \tag{3.2}$$

Figure 3.9 shows plots of Eq. (3.2) for *s*-, *p*- and *d*-waves. The *s*-wave collisions are barrier-less, but for higher partial wave collisions, the atoms need to have sufficient energy to overcome the centrifugal barriers to reach R_C. Based on MOT temperature estimates (next section), the collision energy of the Li and Rb atoms is ~1.1 mK. From the theoretical C_6 and Eq. (3.2), we calculate the *p*-wave barrier height to be 1.9 mK, and it occurs at ~51 Å (~100 a_0). As the atomic collision energy is insufficient to cross the *p*-wave barrier to reach R_C, the ultracold collisions are mainly *s*-wave in character.

Since we are dealing with a one-photon free-bound PA transition, the selection rules for electric-dipole allowed transitions dictate that J for the PA molecules will be at most 2, and the allowed transitions for spontaneous decay to the ground state will be to $J \leq 3$. Our PA laser linewidth of ~1 MHz is narrow enough to resolve the rotational structure. With ionization detection, we

observe $J = 1$ and 2 levels for all of the 4(1) PA resonances, and for 2(1) $v = 10$. However, with only two rotational levels, we cannot reliably calculate B_v, the rotational constant for vibrational level v. On the other hand, we observe three rotational lines for the $2(0^-)$ $v = 8$ level, which we assign as $J = 0$, 1 and 2 in Figure 3.10. We assign the strongest line as $J = 1$ because, according to the selection rules presented in Table 1.3 of Section 1.2.6, there are more allowed transitions from the initial scattering state to $J = 1$ compared to $J = 0$ or 2 [56]. We calculate B_v from the rotational energy $F_v(J)$: $F_v(J) = B_v[J(J+1) - \Omega^2]$. In Figure 3.11 we plot E_{rot} (= $F_v(J)$) versus $J(J+1)$, and determine $B_v = 870(90)$ MHz from the slope of the plot.

Once we determine B_v, we use the rigid rotor model for a diatomic molecule to calculate the classical outer turning point R of our PA level: $B_v = \hbar^2/2\mu R^2$. For $2(0^-)$ $v = 8$, we obtain $R = 9.5(0.5)$ Å, which lies in the range of internuclear spacing for which PA can occur in LiRb, as discussed earlier in the chapter.

Since the $2(0^-)$ $v = 8$, $J = 1$ rotational level is well resolved, we use it in the next section to estimate the maximum collision energy – and hence temperature – of our trapped atoms.

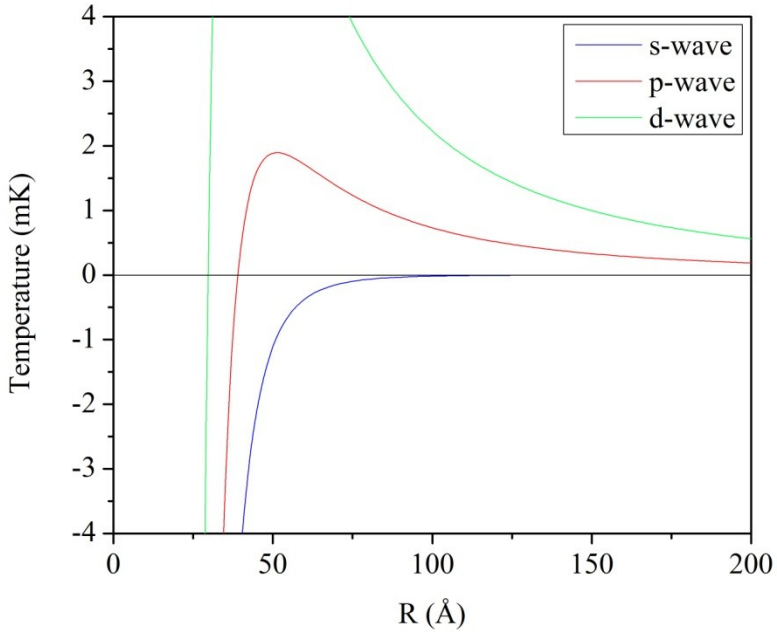

Figure 3.9. Plots of centrifugal barrier heights (in mK) versus internuclear separation (in Å) calculated from Eq. (3.2). In our system, Li and Rb atoms can undergo *s*-wave collisions, but they do not have sufficient energy (~1.1 mK) to overcome the *p*- , *d*- and higher partial wave barriers.

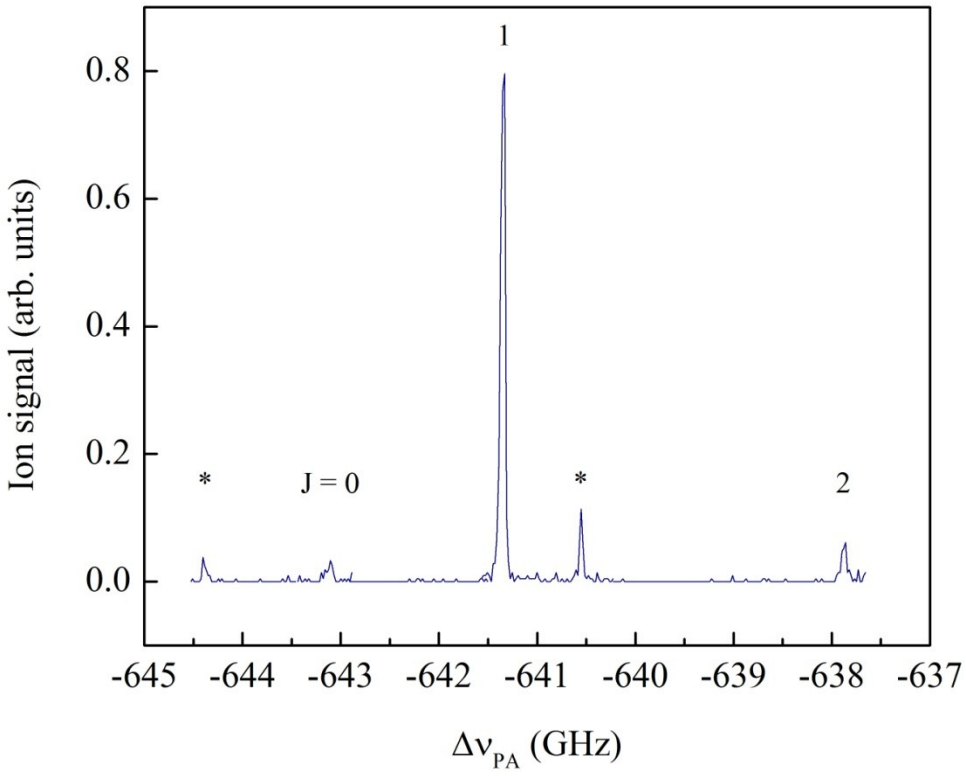

Figure 3.10. Resolved rotational structure of the $2(0^-)$ v = 8 level. The peaks marked with an asterisk (*) are hyperfine ghosts.

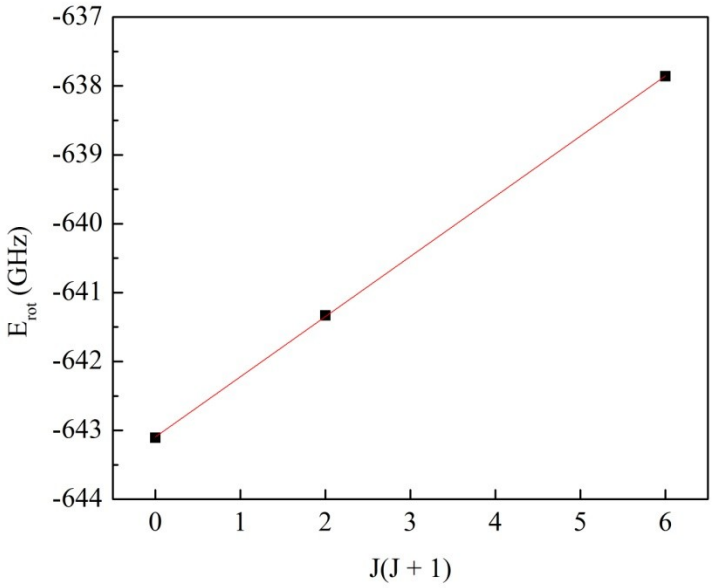

Figure 3.11. Plot of rotational energy E_{rot} versus J(J + 1) for the $2(0^-)$ $v = 8$ level. E_{rot} is measured from the $v_{1/2}$ asymptote. From this fit, we calculate $B_v = 870(90)$ MHz.

3.7 PA lineshape

Li and Rb atoms have a distribution of collision energies in the initial scattering state. If we consider discrete collision energies ε, the PA lineshape due to one particular energy $h\varepsilon$ would be a Lorentzian (in this section the collision energy ε is represented in frequency units). The combined effect of multiple collision energies and their magnitudes affects the overall PA lineshape, and the convolution of individual Lorentzians corresponding to discrete collision energies deviates from a pure Lorentzian. Jones et.al. [74] have developed a model for determining PA lineshapes based on Wigner's threshold law [75]. For low collision energies typically found in ultracold systems, the amplitude of the ground state scattering wavefunction goes as $\varepsilon^{(l+1/2)/2}$, where l is the partial wave angular momentum. The distribution of collision energies is given by the Boltzmann distribution, $e^{-h\varepsilon/(k_B T)}$. Together, the PA lineshape for a continuum of collision energies is given by [67]:

$$W_l(f, f_0) = K \int_0^\infty e^{-\varepsilon/T} \varepsilon^{l+1/2} L_\gamma(f, f_0 - \varepsilon)\, d\varepsilon \tag{3.3}$$

where $L_\gamma(f, f_0 - \varepsilon)$ is a Lorentzian:

$$L_\gamma(f, f_0 - \varepsilon) = \frac{1}{[f - (f_0 - \varepsilon)]^2 + \left(\frac{\gamma}{2}\right)^2} \tag{3.4}$$

γ is the natural linewidth (full width at half maximum, or FWHM) of the excited PA state and the Lorentzian is centered at $(f_0 - \varepsilon)$. f_0 is the threshold energy for PA to occur and $T' = k_B T/h$ is the temperature. K adjusts the amplitude of the calculated lineshape to match the experimental observations.

As PA lineshape reflects the distribution of collision energies, we can use the lineshape calculations from Eq. (3.3) and determine the temperature T of the colliding atoms in the scattering state. Since the $2(0^-)$ $v = 8$ is rotationally well-resolved, we model the $J = 1$ line based on Eq. (3.3). Figure 3.12 shows the experimental $2(0^-)$ $v = 8$ $J = 1$ resonance (dots), along with the calculated overall fit to the lineshape for *s*-wave ($l = 0$) collisions. From the calculated fit, we obtain $T = 1.05(0.1)$ mK and $\gamma = 6(2)$ MHz. This calculation also reinforces our earlier statement that the atoms primarily undergo *s*-wave scattering because the MOT temperature is not high enough for significant *p*- or higher partial wave scattering.

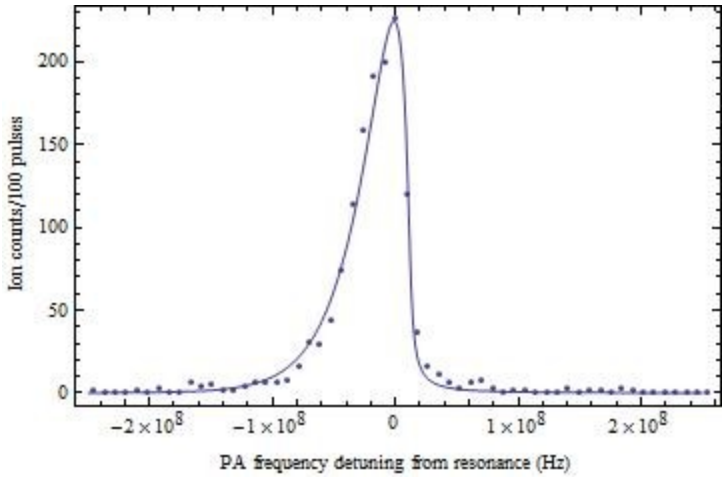

Figure 3.12. PA lineshape fit to the $2(0^-)$ $v = 8$, $J = 1$ PA resonanace (blue dots) using Eq. (3.3). The calculations estimate the MOT temperature to be T = 1.05(0.1) mK.

3.8 Decay to ground triplet state

According to the selection rules for one-photon electric dipole-allowed transitions, the 1(2) and $2(0^-)$ states decay to the $1(0^-)$ and 1(1) states, which correlate to $a^3\Sigma^+$. The 4(1), $2(0^+)$ and 2(1) states can decay to $a^3\Sigma^+$ and $X^1\Sigma^+$ ($1(0^+)$ for Hund's case (c)). In the next chapter we present excited state ionization spectroscopy based on PA lines of the $2(0^-)$ state, and as a prelude we discuss here molecular decay from the $2(0^-)$ $v = 5$ level to the ground electronic state.

Molecules in the ground singlet state have zero magnetic moment, which means they are not affected by a magnetic field. Triplet molecules, on the other hand, have net non-zero spin and interact with a magnetic field [35]. We have observed such an interaction in the form of magnetic trapping of triplet molecules in the MOT magnetic field (~10.6 Gauss/cm) and shown in Figure 3.13[2]. Our investigation proceeds as follows: we introduce a variable delay t between turning off the PA laser and firing the ionization laser pulses. A hard drive read head is used as the variable delay shutter. If the PA beam is continuously on and we fire the ionizing laser, the number of molecules being ionized does not change significantly. This is because molecules escaping the

[2] We cannot run a similar experiment on singlet ground state molecules because, based on selection rules, there is no electronic Hund's case (c) electronic state that decays exclusively to the singlet ground state, i.e. all allowed transitions have an allowed decay channel to the triplet ground state.

magnetic confinement region are replaced by additional molecules that undergo spontaneous emission to the triplet state. Let us assume the excited state lifetime is ~20 ns based on the Rb($5p_{3/2}$) excited state linewidth. For a 4 mm diameter ionizing beam and a MOT temperature of ~1 mK, the molecule transit time through the beam is ~9 ms. As we increase t, the ion signal starts to decrease, seen in Figure 3.13. We notice that the ion signal is present for $t > 9$ ms. In the absence of molecular confinement in the MOT magnetic field, the ion signal should be negligible as the delay t exceeds the molecular transit time. This is because without confinement, there is sufficient time between the PA light being turned off and the arrival of the ionization pulse that PA molecules can escape the ionization volume. The fact that the ion signal is present for $t > 9$ ms suggests that triplet molecules are being trapped in the MOT magnetic field.

In the next section, we use the same $2(0^-)$ $v = 5$ level to estimate the rate of PA molecular formation.

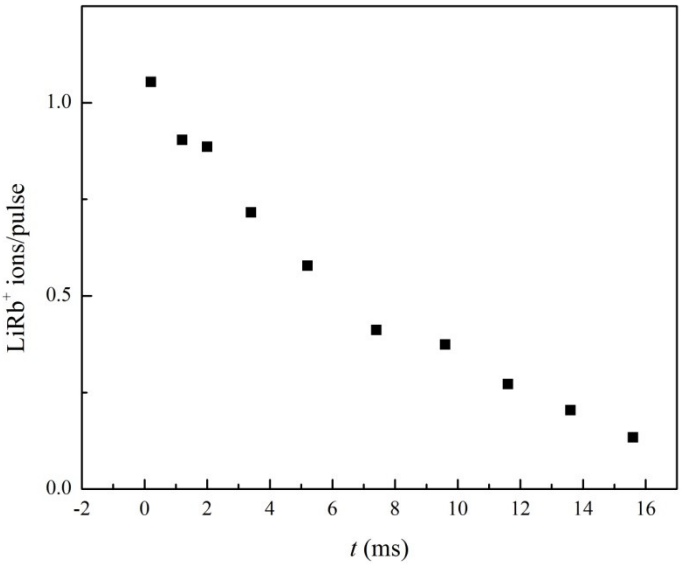

Figure 3.13. Magnetic trapping of ground triplet state molecules. As the delay t between the PA laser shutter and the ion pulse arrival is increased, the ion signal is seen to decrease. Presence of ion signal beyond the ~9 ms transit time of molecules in the ionization beam suggests that we are trapping triplet ground state molecules.

3.9 Molecule formation rate via PA

In this section, we estimate the photoassociation rate, R_{PA}, of molecule formation using ionization detection and compare this with PA formation rate obtained from trap-loss spectroscopy. One of the future goals of our program is to create molecules in the rovibronic ground state, which will subsequently be detected by multiphoton ionization. As some transfer schemes to deeply bound $X^1\Sigma^+$ rovibrational levels may not be very efficient [56], it is important to estimate the initial rate of creation of LiRb molecules given by R_{PA}.

In earlier trap-loss studies, we observed a molecule formation rate of ~3.5 $\times 10^7$ s^{-1} for the $3(0^+)$ v = 3 level. However, since we do not observe $3(0^+)$ vibrational levels with ion detection, we use data for the $2(0^-)$ v = 5 level to estimate R_{PA}. The following calculation, based on [44], takes into account molecular creation, ionization and detection efficiencies that will be relevant to ionization detection of ground state molecules as well.

The number of ions detected per ionization pulse, N_{ion}, depends on i) N_a, the number of ground (triplet) state molecules, ii) the probability, p_{ion}, of ionizing molecules per ion pulse, and iii) the detection efficiency e_d. In other words,

$$N_{ion} = N_a p_{ion} e_d \tag{3.5}$$

For the $2(0^-)$ v = 11 level, we record a strong ion signal N_{ion} ~ 2 ions/pulse. The ionization probability is calculated as [44]:

$$p_{ion} = 1 - e^{-\sigma E\lambda/hc\pi\omega^2} \tag{3.6}$$

σ is the photoionization cross-section, which we estimate for LiRb to be between 10^{-23} and 10^{-24} m^2 based on estimates for Li and Rb [76]. With pulse energy E ~ 3 mJ, ionizing laser wavelength λ = 565 nm and the pulse beam diameter, 2ω = 4 mm, we obtain from Eq. (3.6) p_{ion} ~ 7×10^{-3} – 7×10^{-4}. Estimating the detection efficiency e_d is difficult as it is related to the MCP detector efficiency and also the probability that an ion generated by the ionization laser strikes the MCP. Here, we estimate e_d between 0.1 and 0.8. Using the values for p_{ion} and e_d along with N_{ion}, we calculate from Eq. (3.5) an estimate for the number of molecules in the ground triplet state: N_a ~ 5×10^2 – 3×10^4/pulse.

Once we know the initial number of ground state molecules, we can calculate the photoassociation rate, R_{PA}, from [44]:

$$N_a = \frac{R_{PA}(FCF)t}{1 + t/\tau} \tag{3.7}$$

where τ is the transit time of the molecules in the ionizing beam volume. For a 4 mm beam diameter and molecules with kinetic energy ~1 mK, $\tau \sim 9$ ms. *FCF* is the Franck-Condon factor (FCF) for decay from the PA level to a vibrational level of the ground state. For our calculations, we choose the $v'' = 9$ level of $a^3\Sigma^+$ which has good wavefunction overlap with the chosen PA level and hence a large FCF of 0.1. The FCF is calculated from *ab initio* LiRb PECs [50] using the LEVEL 8.0 program [77]. Substituting the FCF, transit time τ and N_a into Eq. (3.7), we calculate the LiRb PA molecule formation rate to be $R_{PA} = 10^5 - 10^7$ s^{-1}. Considering the uncertainty in the photoionization cross-section σ and detector efficiency e_d, this estimate compares favorably with the PA rate calculated from our LiRb trap-loss measurements (~3.5×10^7 s^{-1}), which is one of the largest among heteronuclear molecules [68].

3.10 Conclusion

We have presented PA spectroscopy using ionization detection, and, where possible, compared our results with earlier trap-loss measurements. In addition we observe new, more deeply bound PA lines that expand our knowledge of excited state potentials. From these new lines, we refine the long-range C_6 dispersion coefficients that can be used to further extrapolate new PA line positions at larger binding energies. We also resolve rotational structure of the $2(0^-)$ $v = 8$ level with ion detection, and use this information to calculate the outer turning point. This calculation is useful to determine classical turning points of vibrational levels, which in turn give an indication of ground and excited state wavefunction overlap. From the PA lineshape of the $2(0^-)$ $v = 8$, $J = 1$ resonance and comparison with the theoretical model of [67], we calculate the maximum MOT temperature as ~1.1 mK. We demonstrate trapping of ground triplet molecules in the MOT magnetic field, and also calculate PA molecule formation rate R_{PA} using ion detection parameters. The results presented in this chapter provide important information related to the MOT operation, ion detection system, and, most importantly, the energy level structure of LiRb molecules, which will be important for future identification of schemes to create LiRb molecules in the ground rovibronic state. Finally, some of the newly discovered PA lines are used to record

resonantly enhanced multiphoton ionization spectroscopy (REMPI) of ground and excited electronic states. REMPI spectroscopy is the subject of the next chapter.

4. LIRB EXCITED STATE IONIZATION SPECTROSCOPY

Having presented PA spectroscopy of several high-lying vibrational levels near the Li(2s) + Rb($5p_{1/2}$) and Li(2s) + Rb($5p_{3/2}$) asymptotes, we now investigate the ground triplet state and excited electronic states using REMPI spectroscopy. Our goal in undertaking this experiment is two-fold: first, we would like to gain more insight into the energy level structure of LiRb molecules. Very few studies involving LiRb have been undertaken, whether in hot vapor or ultracold systems. REMPI spectroscopy can start to shed light on some of the as-yet unknown electronic states. In line with exploring these energy levels is our eventual goal of transferring ultracold LiRb molecules into the rovibronic ground state. As we mentioned in Chapter 1, rovibronic ground state molecules possess a large electric dipole moment that figures into applications involving quantum computation and ultracold chemistry, among others. Transferring molecules to the ground state is a challenging prospect because PA molecules are formed in vibrational levels that do not have a good wavefunction overlap with deeply bound ground state molecules. With REMPI spectroscopy, we wish to explore excited state levels to find possible transition pathways to the rovibronic ground state.

This chapter presents our spectroscopic studies of excited electronic states of LiRb using ionization detection. We use REMPI spectroscopy to map out vibrational levels of the $(3)^3\Pi$ and $(4)^3\Sigma^+$ states. In the process, we also determine vibrational levels of the ground $a^3\Sigma^+$ state.

We begin this chapter by explaining further the need to perform these spectroscopic studies. Details of the experimental setup are presented next, followed by the REMPI spectra and interpretation of observed spectra features. Our analysis is aided by LiRb *ab initio* calculations, and we explain our spectroscopic observations by referring to these calculations.

4.1 Motivation

In the discussion so far, we have seen how to create ultracold LiRb molecules in excited electronic states using PA. These molecules undergo spontaneous emission and decay to vibrational levels of the $a^3\Sigma^+$ and $X^1\Sigma^+$ states. However, we cannot entirely rely on spontaneous decay to populate the absolute ground rovibronic state ($X(v = 0, J = 0)$, or $X(0, 0)$). Spontaneous decay is governed by the overlap between the excited state (PA) wavefunction and the wavefunction of the ground rovibrational levels, which is also reflected in the calculated Franck-Condon factors between the two states. Based on this overlap, PA molecules predominantly decay to high-lying ground state vibrational levels, with very weak (if nonzero) FCF for decay to the absolute ground state. Hence, producing molecules in the ground rovibronic level in a single step – PA followed by spontaneous decay – may be inefficient at best, producing an insufficient number of molecules for further study.

Instead of relying on spontaneous decay, we can excite molecules to known levels in excited states that have a more favorable wavefunction overlap with the absolute ground state, and use stimulated emission to drive population to $X(0, 0)$. For this scheme to work, we need to know the excited state energy levels. Conventional excited state spectroscopy is performed in a thermal vapor in which the molecules are excited from deeply bound ground state vibrational levels. In ultracold systems, we can use multiphoton ionization to map out these levels. PA molecules that decay to the high-lying vibrational levels of the ground electronic states can be ionized using REMPI, with the resonant intermediate state being the subject of our study. Performing excited state spectroscopy is therefore relevant for exploring possible pathways to transfer loosely bound PA molecules to the absolute ground state.

Multiphoton ionization spectroscopy is applicable to diatomic and polyatomic molecules. In ultracold physics in particular, REMPI spectroscopy has been instrumental in exploring and identifying structure at short and intermediate internuclear spacing in both homonuclear and heteronuclear molecules (for example, compare [37], [78] and [79]). Different combinations of alkali molecules produce a rich and diverse set of spectra. For example, one-photon electric-dipole selection rules differ slightly between homonuclear and heteronuclear molecules, which in turn impose different restrictions on allowed transitions for the two classes of molecules. Interpretation of excited state spectra therefore takes into account selection rules to explain the observed structures.

Among alkali heteronuclear molecules, LiRb is one of the least studied systems. Heat pipe spectroscopy of the $X\,^1\Sigma^+$, $B^1\Pi$ and $D^1\Pi$ levels has recently become available (see Chapter 1), but the vast majority of LiRb electronic states remain unknown. Theoretical support has been available mainly in the form of [50, 54, 55]. Based on these *ab initio* calculations, particularly from Korek et.al. [50], and with the REMPI spectroscopy data presented in this chapter, we have managed to shed light on some of these unexplored electronic states with the aim to better understand the LiRb molecular structure. Eventually, this information may be useful as a stepping stone for suitable transition pathways to efficiently populate the ground rovibronic level.

4.2 Experimental setup

The MOT parameters are the same as those used for PA spectroscopy in Chapter 3. For REMPI spectroscopy, since the Ti:S frequency is fixed on a chosen PA resonance, we also monitor the frequency drift. Through a joint collaboration with Dr. Andrew Weiner, we have access to a Menlo Systems frequency comb (FC1500-250-WG) that is used for this purpose. A photonic crystal fiber (PCF) produces light in the 530-900 nm range and adjacent teeth in the frequency comb are spaced by 250 MHz. The output is fiber coupled and transported to our lab, where we generate a heterodyne beat signal between the Ti:S and the tooth of the frequency comb that is closest in frequency to the Ti:S (in 250 MHz steps). Both beams are combined on a PBS and copropagate towards a fast photodiode which is connected to an rf spectrum analyzer for beat signal measurement. The linewidth of the beat signal is ~2 MHz. During normal operation, the beat signal may drift by ~5 MHz over a period of 30-45 minutes, which is the typical length of time we acquire data. This drift is less than the typical linewidth of our PA resonances (~10s of MHz) and does not affect our REMPI spectra.

The PDL-2 laser used for PA ionization spectroscopy is also used here with R590 dye. This laser has a linewidth of ~0.3 cm^{-1}. Typical pulse energy for REMPI spectroscopy is 2-3 mJ, with a ~4 mm beam diameter at the MOT. The PDL wavelength is measured with a Coherent WaveMaster wavemeter, with an accuracy of ~0.2 cm^{-1}. The ion detection hardware operates under the same conditions as described in earlier chapters. A Labview program counts and records the number of $LiRb^+$ ion strikes. The program also controls the wavelength of the PDL, so that after acquiring x number of shots at λ_{PDL}, it changes the PDL diffraction grating angle via a stepper motor control to output a new wavelength $\lambda_{PDL} \pm \Delta\lambda$. The sign and magnitude of the change of wavelength $\Delta\lambda$ are adjustable parameters through the program. The spectra presented in this chapter are acquired

with $\Delta\lambda \sim 0.3$ cm^{-1}. Over a 30-45 minute period and during normal system operation, we typically acquire between 30 and 35 cm^{-1} of continuous spectra.

4.3 REMPI spectra

Figure 4.1 shows a schematic of the REMPI process. LiRb molecules created by PA spontaneously decay to the ground electronic states. A pulsed laser ionizes the ground state molecules via an intermediate electronic state using two identical photons. The spectroscopic data presented in this chapter are acquired by fixing the PA laser frequency at three PA resonances: v_{PA} = 5, 9 and 11, all belonging to the $2(0^-)$ electronic states. Spectra for v_{PA} = 5 and 11 are recorded for PDL wavelengths between 17280 cm^{-1} and 18050 cm^{-1} (~578.7 and 554.0 nm, respectively), and between 17589 cm^{-1} (~568.5 nm) and 17821 cm^{-1} (~561.1 nm) for v_{PA} = 9. These are shown in Figures 4.2 – 4.4. From one-photon electric-dipole selection rules $\Delta\Omega = 0, \pm 1$ except $0^{\pm} \nleftrightarrow 0^{\mp}$, molecules from the $2(0^-)$ state decay to $1(0^-)$ and 1(1), which correlate to the $a^3\Sigma^+$ state. For the stated PDL wavelength range, LiRb molecules ionize through intermediate electronic states that are asymptotic to the Li(2s) + Rb(4d$_j$) states (j = 3/2 and 5/2). In the experimental line assignments presented below, the uncertainty in the transition energies (in cm^{-1}) is estimated to be ~0.5 cm^{-1} mainly due to the PDL linewidth and uncertainty in the wavemeter reading.

4.3.1 Analysis of spectra

Figures 4.5 (a) – (e) show combined REMPI spectra for v_{PA} = 5 (orange), v_{PA} = 9 (green) and v_{PA} = 11 (blue) PA resonances. Note that the label E for the horizontal axis denotes the PDL wavelength in cm^{-1}. We have identified and labeled transitions originating from $a^3\Sigma^+$ v'' = 7 – 13 to v' = 0 – 10 of the three observed spin-orbit components Ω = 0, 1 and 2 of the $(3)^3\Pi$ excited state. For brevity, we include the spin-orbit component of this state as a subscript: $(3)^3\Pi_\Omega$. We have also identified v' = 0 – 5 of the $(4)^3\Sigma^+$ excited state. Based on our analysis, we do not observe spin-orbit splitting of this state. In the rest of this chapter, we distinguish vibrational levels of $(3)^3\Pi$ from those of $(4)^3\Sigma^+$ by using the notation v_Π' and v_Σ', respectively. In Figure 4.5 (c), the peaks outlined by the black box and labeled with an asterisk (*) originate from Rb one- and two-photon transitions $5p_{3/2}$ – 9s and 5s – 9s, respectively. This is consistent with the Rb MOT operation, where atoms are subjected to the 5s – $5p_{3/2}$ cycling transition which ensures there is population in both levels. As the PDL scans through the Rb transitions, excessive Rb^+ ions are

produced. We believe that due to the increased charge density in the MOT region, Coulomb repulsion becomes significant and affects the Rb^+ TOF such that Rb^+ ions starts leaking into the $LiRb^+$ detection window. Aside from the inconvenience of an unwanted signal, the Rb one- and two-photon lines serve as a useful wavelength marker for all three spectra.

In the discussion below, we focus on the features corresponding to $a^3\Sigma^+ v'' - (3)^3\Pi_\Omega v_\Pi'$ ($\Omega = 0$, 1 and 2). Later in the chapter, we discuss features associated with $a^3\Sigma^+ v'' - (4)^3\Sigma^+ v_\Sigma'$ transitions.

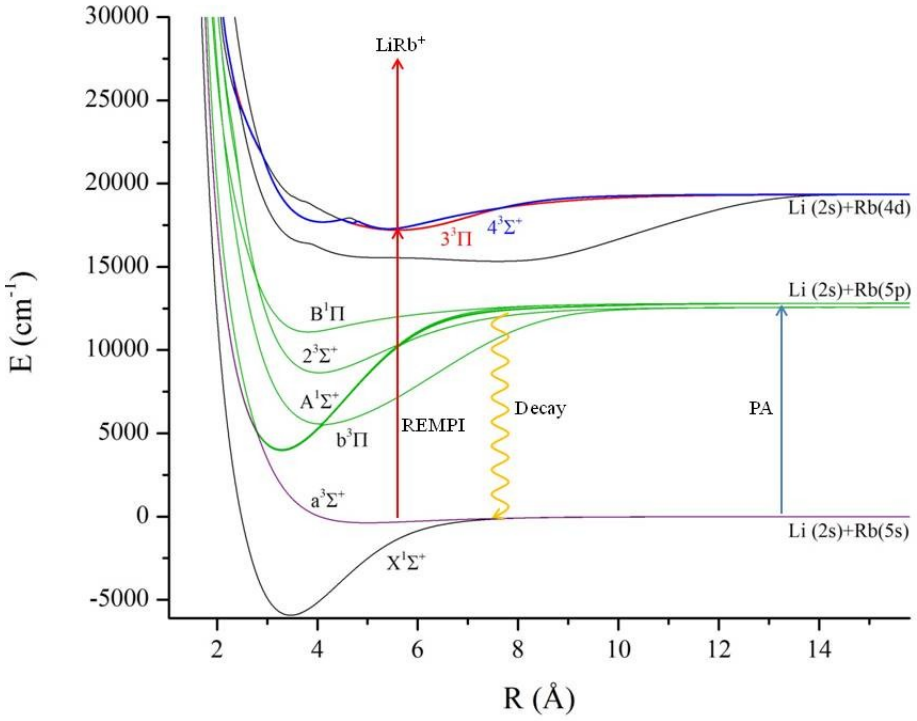

Figure 4.1. Schematic of the REMPI process. PA molecules decay to the ground state and are resonantly ionized by a pulsed laser through an intermediate electronic state.

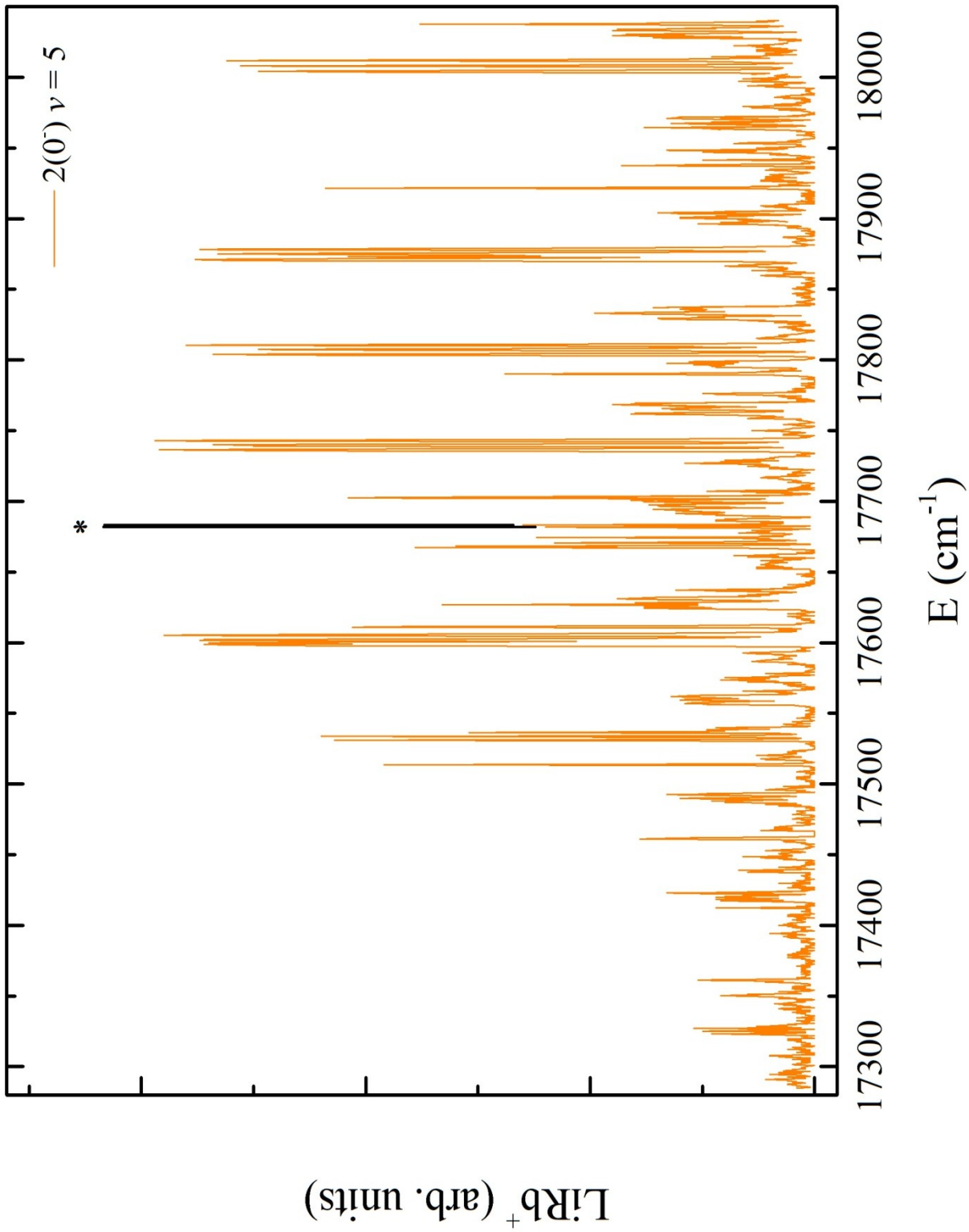

Figure 4.2. REMPI spectrum recorded for the $2(0^-)$ $v_{PA} = 5$ PA resonance. The asterisk (*) denotes Rb one- and two-photon resonances.

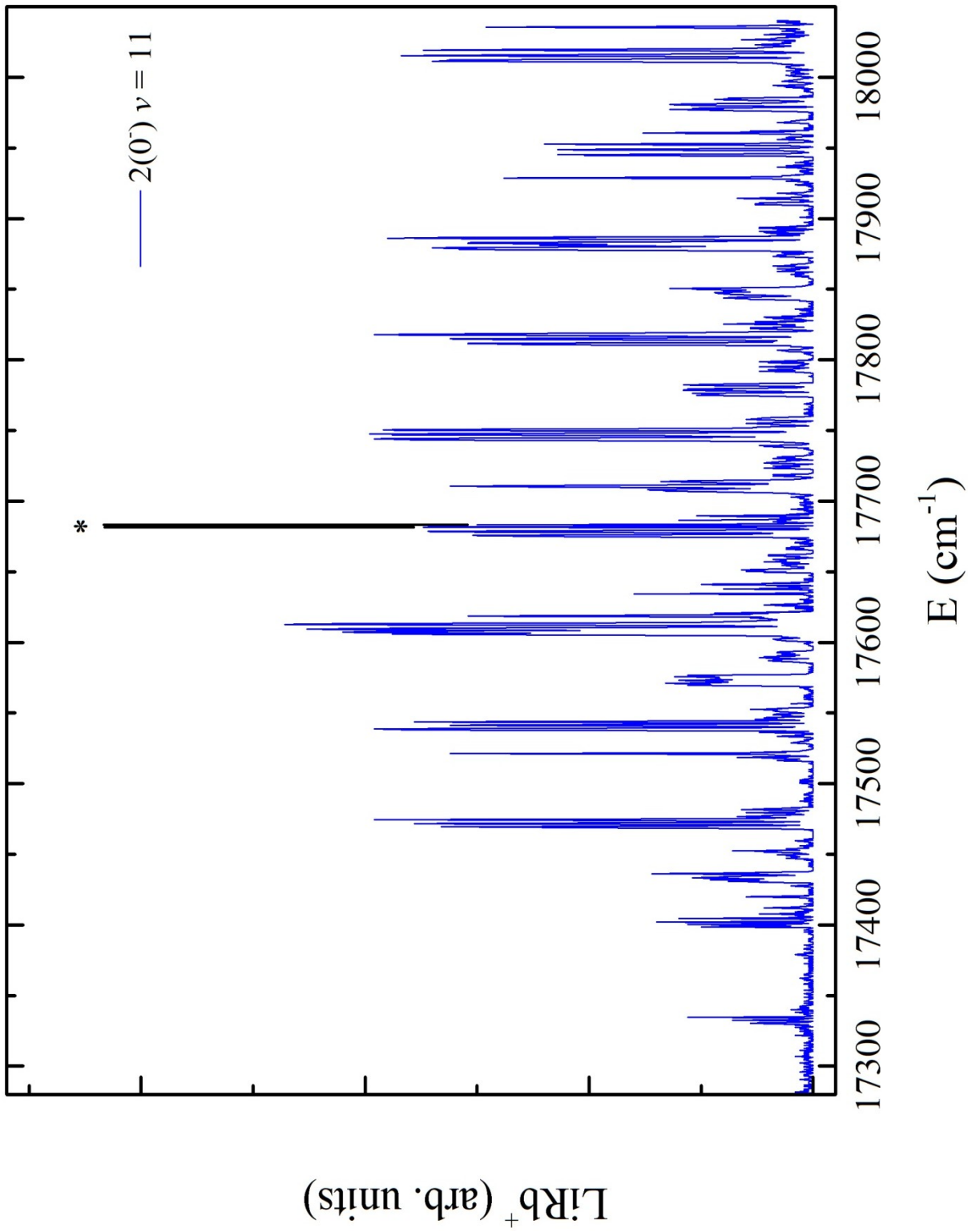

Figure 4.3. REMPI spectrum recorded for the $2(0^-)$ v = 11 PA resonance. The asterisk (*) denotes Rb one- and two-photon transitions.

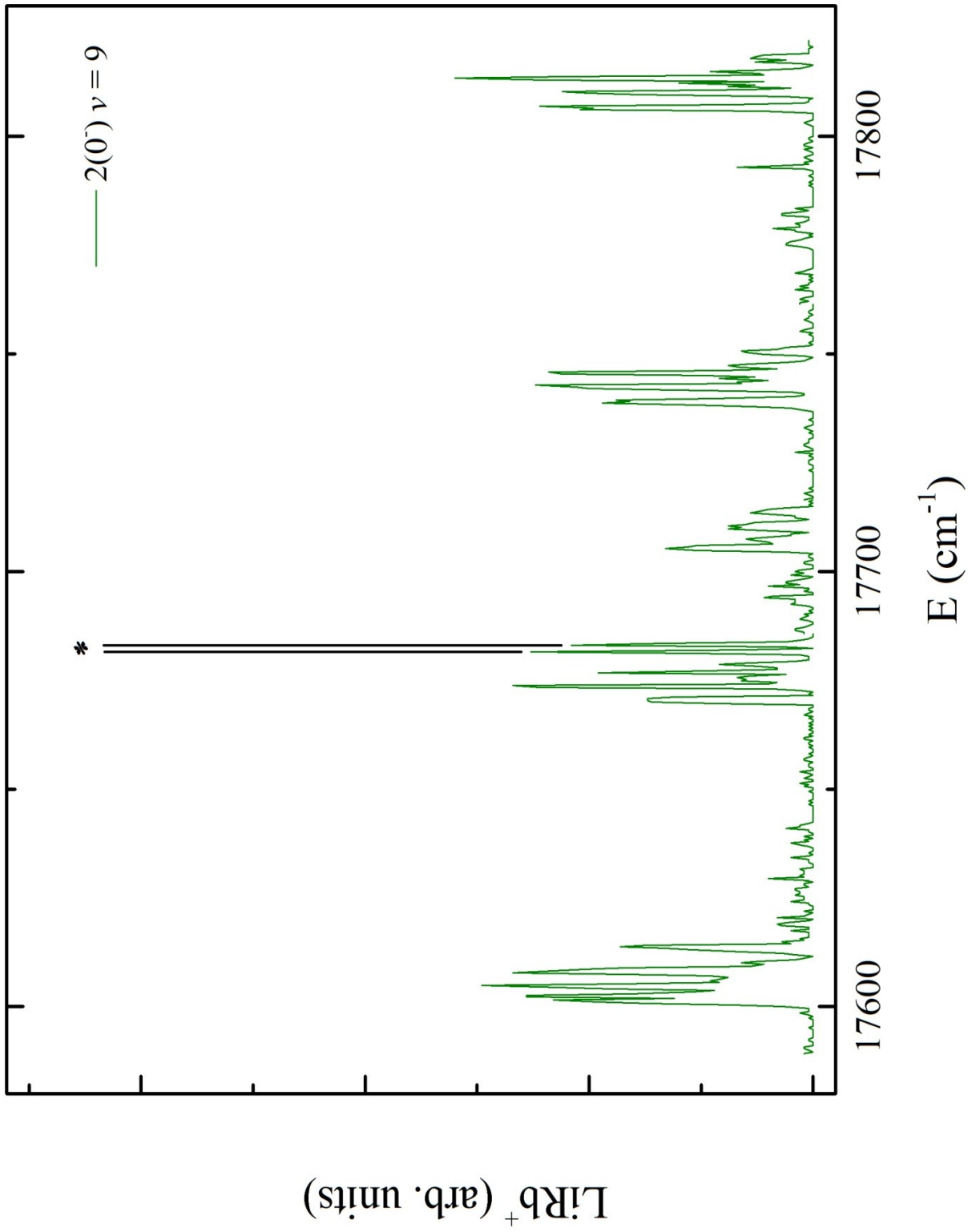

Figure 4.4. REMPI spectrum recorded for the $2(0^-)$ v = 9 PA resonance. The asterisk (*) denotes Rb one- and two-photon transitions

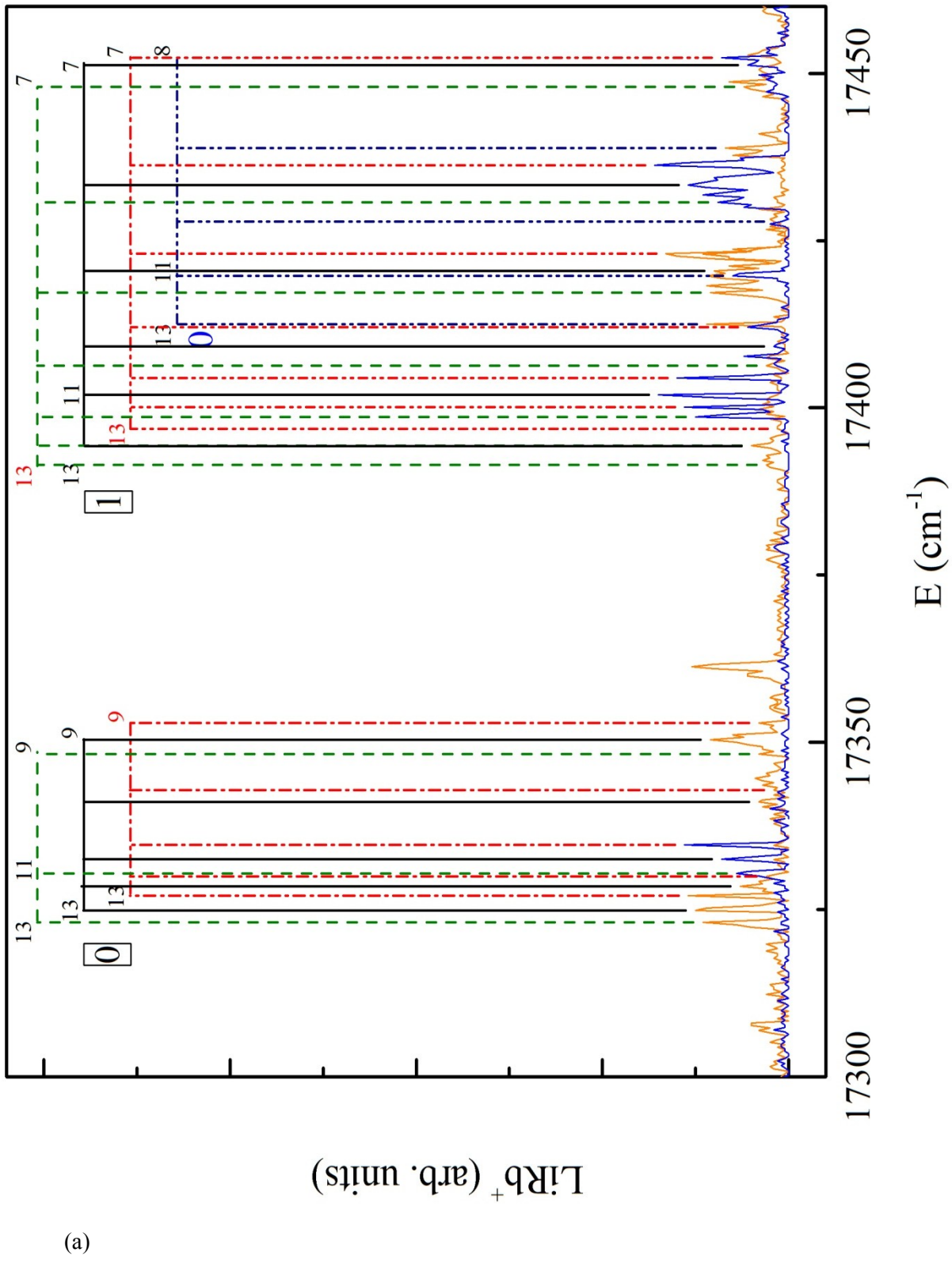

(a)

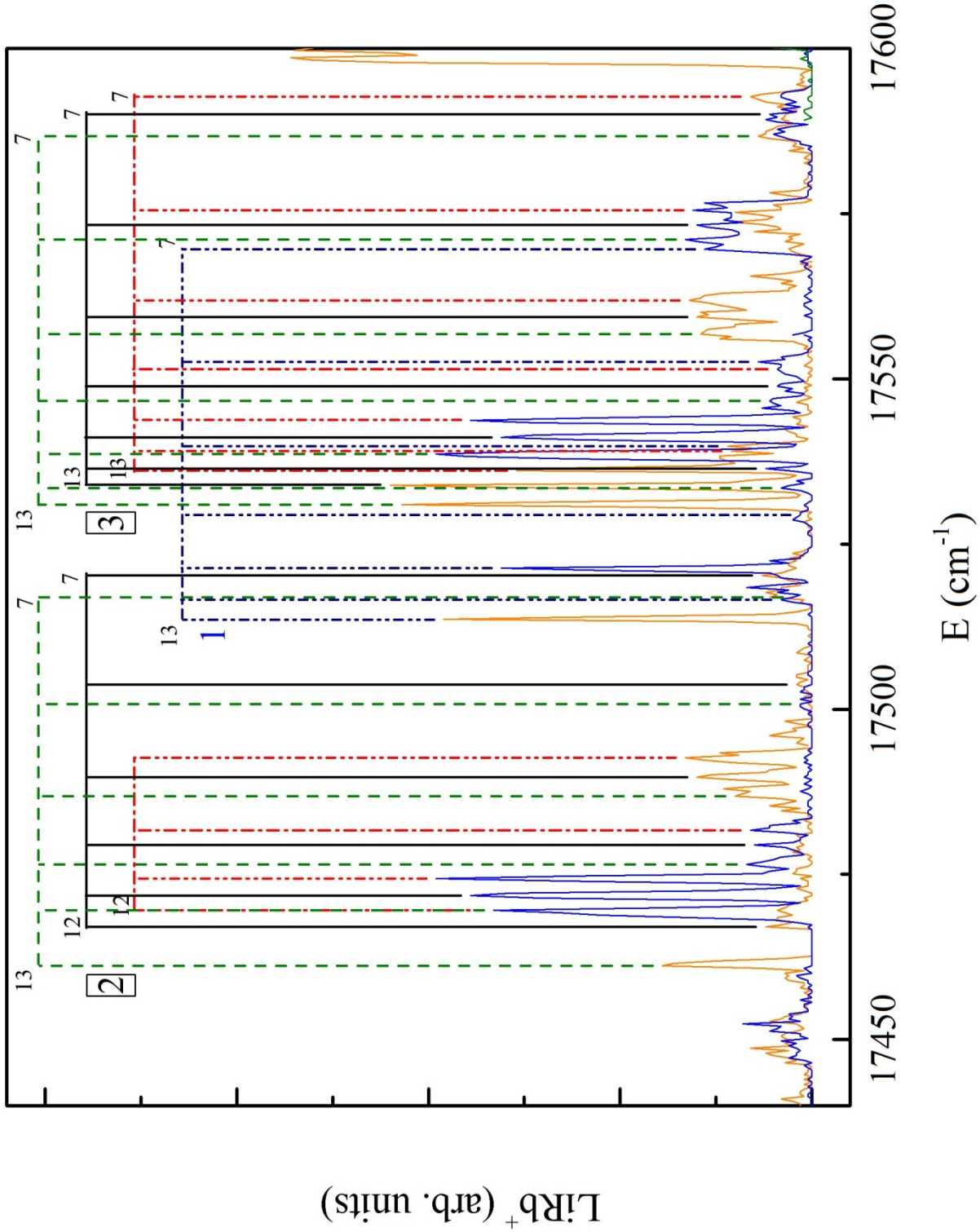

(b)

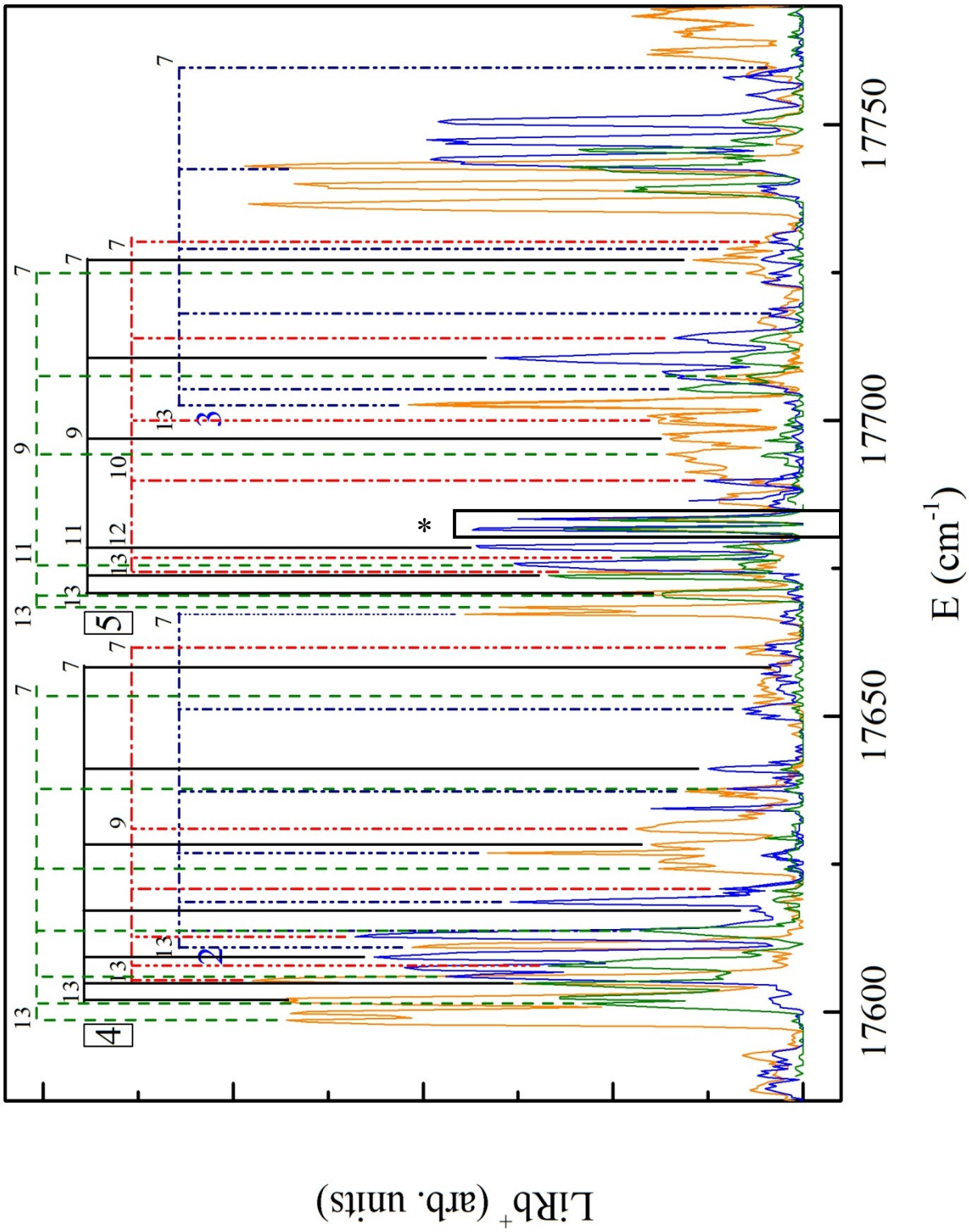

(c)

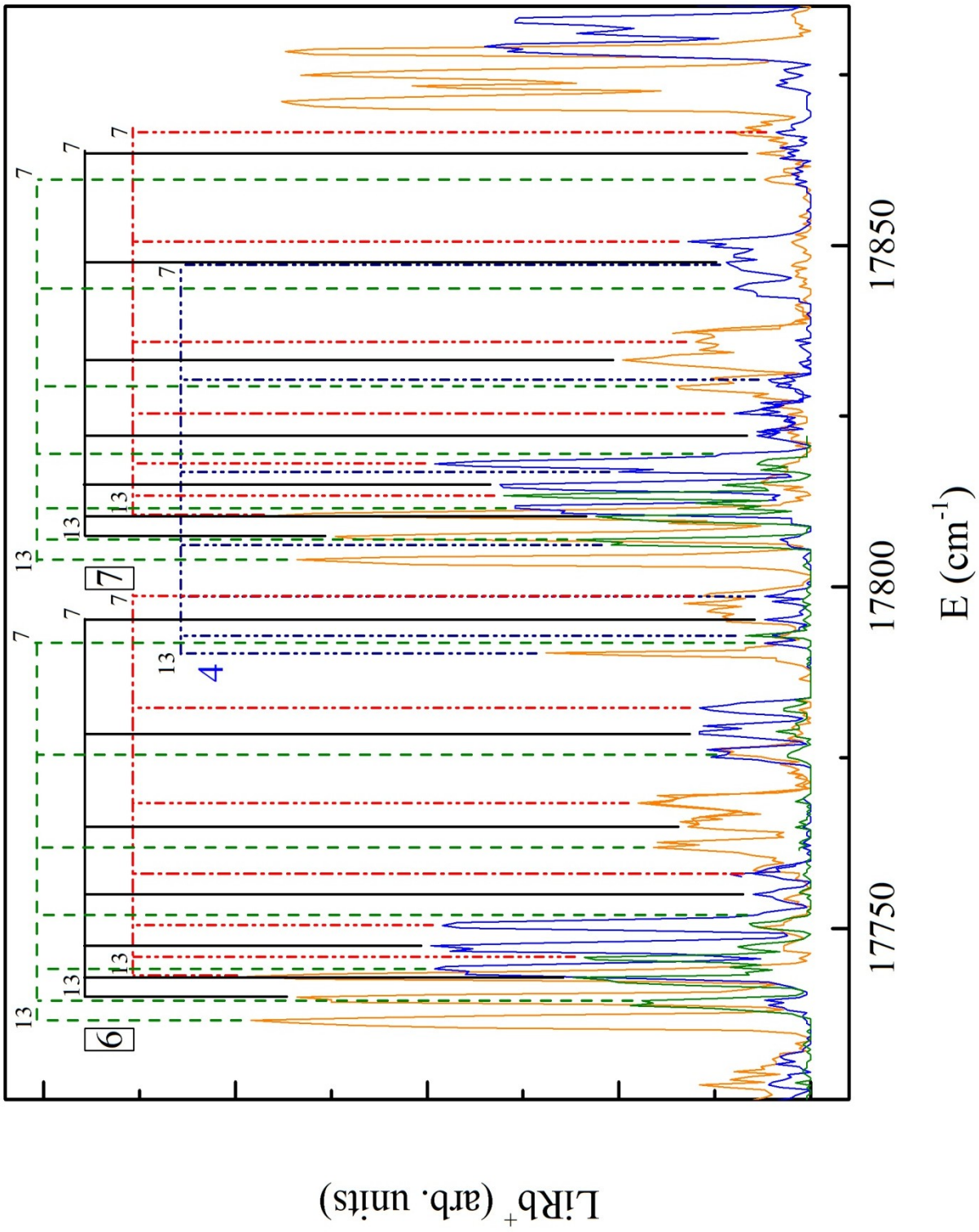

(d)

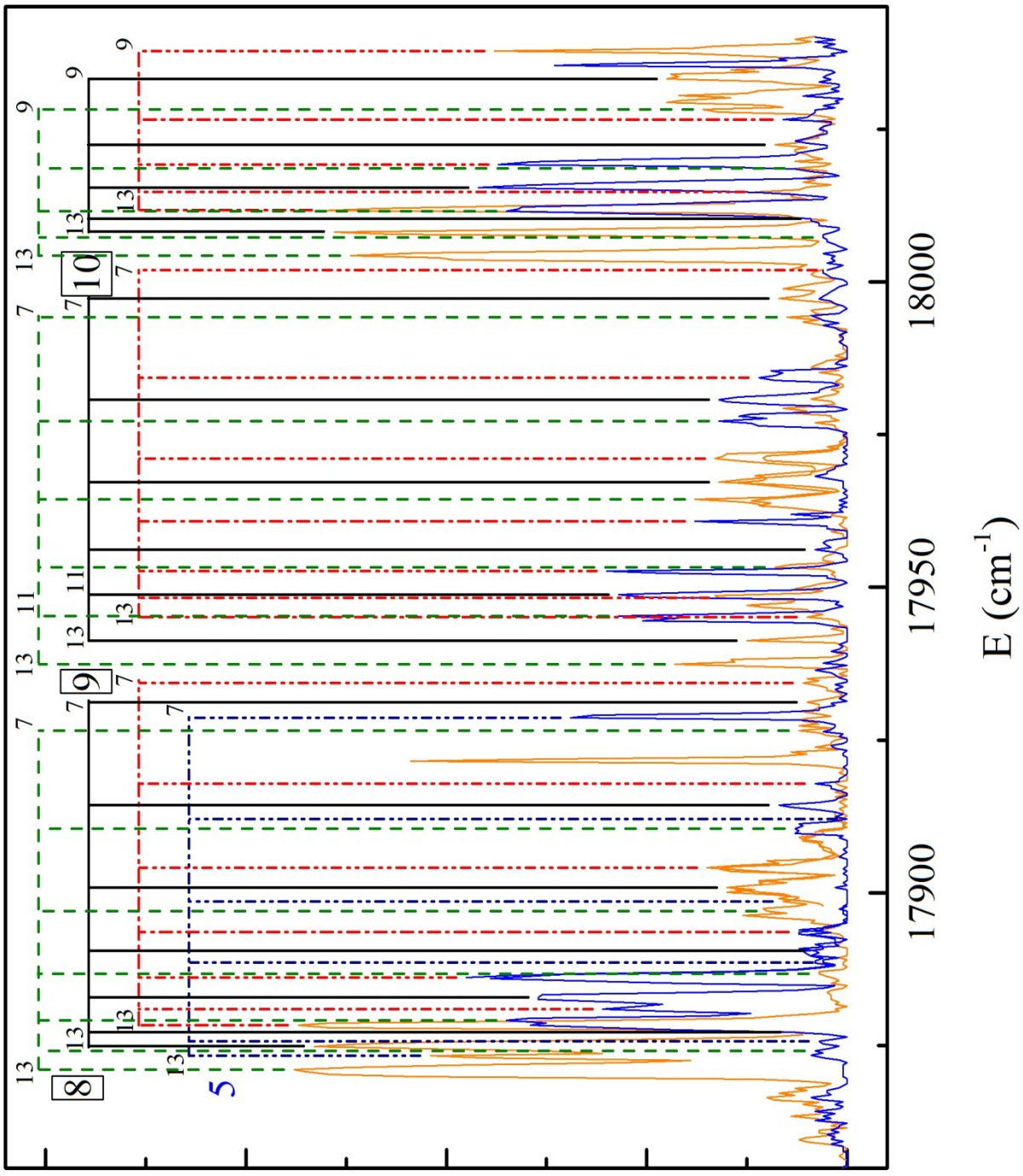

(e)

Figure 4.5. (a) – (e). Labeled REMPI spectra for $2(0^-)$ v = 5, 9 and 11. The labeling scheme is: $(3)^3\Pi$ Ω-components are labeled by the green dashed (Ω = 0), black solid (Ω = 1) and red dash-dot (Ω = 2) lines, and the $(4)^3\Sigma^+$ lines are labeled by the blue dash-dot-dot lines. The numbers on top of the horizontal lines label $a^3\Sigma^+$ v'', while the numbers on the side of the vertical lines are $v_\Pi{}'$ for $(3)^3\Pi$ (black boxed numbers) and v'_Σ for $(4)^3\Sigma^+$ (blue unboxed). The boxed peaks in (c) and labeled with an asterisk are Rb^+ one- and two-photon resonances.

4.3.2 Features associated with $a^3\Sigma^+$ v" – $(3)^3\Pi_\Omega$ v_Π' transitions

In Figure 4.6, we show a section of the REMPI spectrum between 17725 and 17825 cm^{-1} to highlight several distinct features. To avoid congestion and to convey our argument, we have not labeled all of the assigned peaks. In the figure, we observe structure on three different scales. On the largest energy scale, we observe recurring features spaced by ~70 cm^{-1}. These are seen as a grouping of triplets around 17740 cm^{-1} and around 17810 cm^{-1}, and occur in the REMPI spectra of each of the v_{PA} = 5, 9 and 11 PA lines. We assign these features separated by ~70 cm^{-1} as $(3)^3\Pi_\Omega$ vibrational levels v'_Π.

Each v'_Π line also has a characteristic triplet substructure. Adjacent 'teeth' within each triplet are regularly spaced by ~3 cm^{-1}. In addition, we observe that each tooth within a triplet shows almost equal signal strength. This is seen in each of the three sets of v_{PA} REMPI spectra. We assign these triplets – from lowest to highest wavelength (in cm^{-1}) – as the Ω = 0, 1 and 2 spin-orbit components of $(3)^3\Pi$.

The $a^3\Sigma^+$ vibrational levels v" are observed as the increasing spacing of the triplet set of peaks as we go towards higher wavelength (in cm^{-1}). Transitions from high-lying vibrational levels v" near the dissociation limit appear stronger than transitions from more deeply bound (lower v") levels.

Having identified line positions and features corresponding to $a^3\Sigma^+$ v" – $(3)^3\Pi_\Omega$ v_Π' transitions, we now present details of vibrational level assignment of the $(3)^3\Pi_\Omega$ states.

4.4 $(3)^3\Pi_\Omega$ vibrational levels and spin-orbit components

In order to assign the line positions to vibrational levels of an excited electronic state, we make use of *ab initio* calculations of LiRb PECs by Korek et.al., which include spin-orbit interactions [50]. For calculations of $a^3\Sigma^+$ v", we employ the potential curve calculated by Ivanova et.al. [42]. Throughout this chapter, we use LEVEL 8.0 [77] to calculate electronic state vibrational levels and Franck-Condon factors.

The *ab initio* potentials with spin-orbit interactions show numerous avoided crossings. For these adiabatic potentials, we assume separation of nuclear and electronic motion based on the Born-Oppenheimer approximation, which gives rise to avoided crossings between electronic states of the same symmetry. However, the relativistic wavefunction in the vicinity of these avoided

crossings changes rapidly and results in non-adiabatic effects [79]. If the nuclei move fast enough that the electronic and nuclear motion cannot be decoupled, curves that previously avoided crossing each other may do so and result in diabatic PECs. The probability P of such a diabatic crossing to occur is given by the Landau-Zener formula [81, 82]. P depends on the interaction matrix H_{12} between states $|1\rangle$ and $|2\rangle$ and the rate of change of energies E_1 and E_2 of the two states:

$$P = e^{-2\pi\Gamma} \tag{4.1}$$

where $\Gamma = |H_{12}|^2 / \left|\frac{\partial}{\partial t}(E_2 - E_1)\right|$. For a derivation of the Landau-Zener formula, see [83]. We modify the *ab initio* PECs asymptotic to Li(2s) + Rb(4d$_j$) and Li(2s) + Rb(6s) by using diabatic crossings and recalculate the PECs. The modified diabatic PECs are shown in Figure 4.7, where we highlight the relevant $(3)^3\Pi$ and $(4)^3\Sigma^+$ curves.

The $(3)^3\Pi$ state consists of four spin-orbit components: Ω = 0^-, 0^+, 1 and 2. From LEVEL calculations of the diabatic PECs, we calculate and show the spin-orbit components in Figure 4.8. At the equilibrium internuclear separation R_e ~5.6 Å, the calculated energy splitting between Ω components is given in Table 4.1, which shows that the ΔE_Ω are not equal. The REMPI spectra reveal a slightly different picture: we observe only three out of four spin-orbit components, and ΔE_Ω appears to be equal between the teeth of the triplet structures. This comparison between theory and experiment may help to develop a better model for the $(3)^3\Pi$ state. We note that degeneracy of the 0^+ and 0^- components, as well as roughly equal spacing between Ω = 0 and 1, and Ω = 1 and 2 has also been observed in REMPI spectroscopy performed in KRb [78].

In Table 4.2 we list the calculated vibrational levels of the $(3)^3\Pi_\Omega$ components and their spacing ΔG_{th}. We compare these values with our experimental results, listing transition energies for $a^3\Sigma^+$ (v'' = 11) – $(3)^3\Pi_\Omega$ v_Π' lines. We assign v_Π' starting with 0 because for both sets of REMPI spectra, we do not observe structure at wavelengths below ~17323 cm^{-1}. This could indicate that we have reached the bottom of the $(3)^3\Pi$ potential well. In addition, we identify lines corresponding to $(4)^3\Sigma^+$ v_Σ' (presented later in the chapter) and compare the relative line positions of $(3)^3\Pi$ and $(4)^3\Sigma^+$ levels. The spacing between $(3)^3\Pi_{\Omega=0}$ (v_Π' = 0) and $(4)^3\Sigma^+$ (v_Σ' = 0) levels is experimentally determined to be ~89.4 cm^{-1}. Theoretical calculations of the same vibrational level energy difference give ~85.5 cm^{-1}, which compares favorably with our experimental spacing.

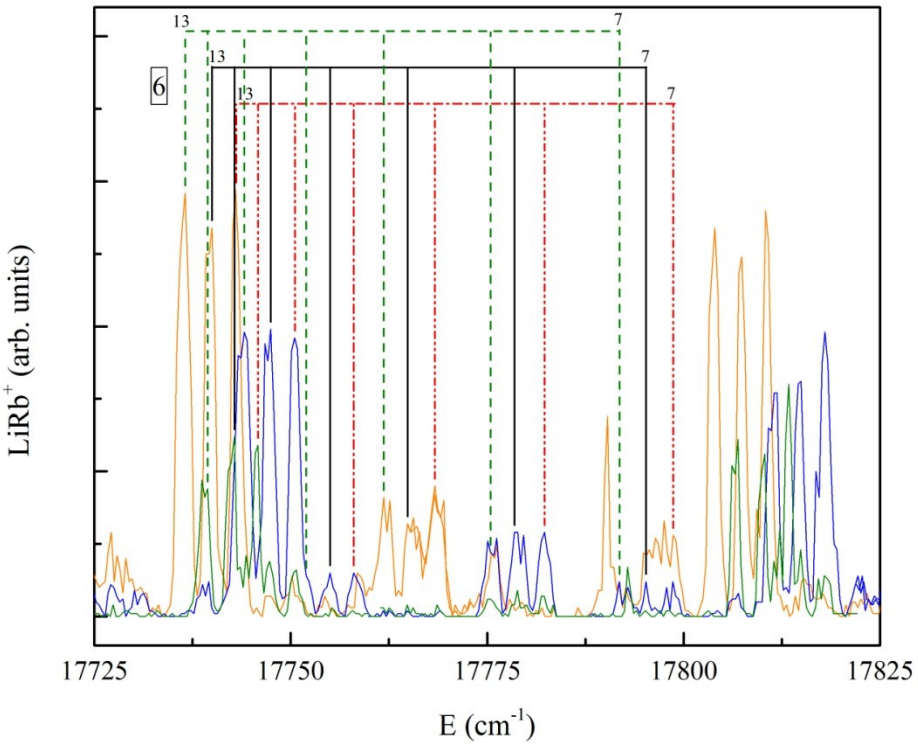

Figure 4.6. Short section of the REMPI spectrum, showing features and patterns originating from $(3)^3\Pi\ v'_{\Pi}$, $(4)^3\Sigma^+\ v'_{\Sigma}$ and $a^3\Sigma^+\ v''$. To avoid congestion, we label only selected lines assigned to $a^3\Sigma^+\ v'' - (3)^3\Pi_{\Omega}\ v_{\Pi}'$ transitions. We will address $a^3\Sigma^+\ v'' - (4)^3\Sigma^+\ v_{\Sigma}'$ later in the chapter.

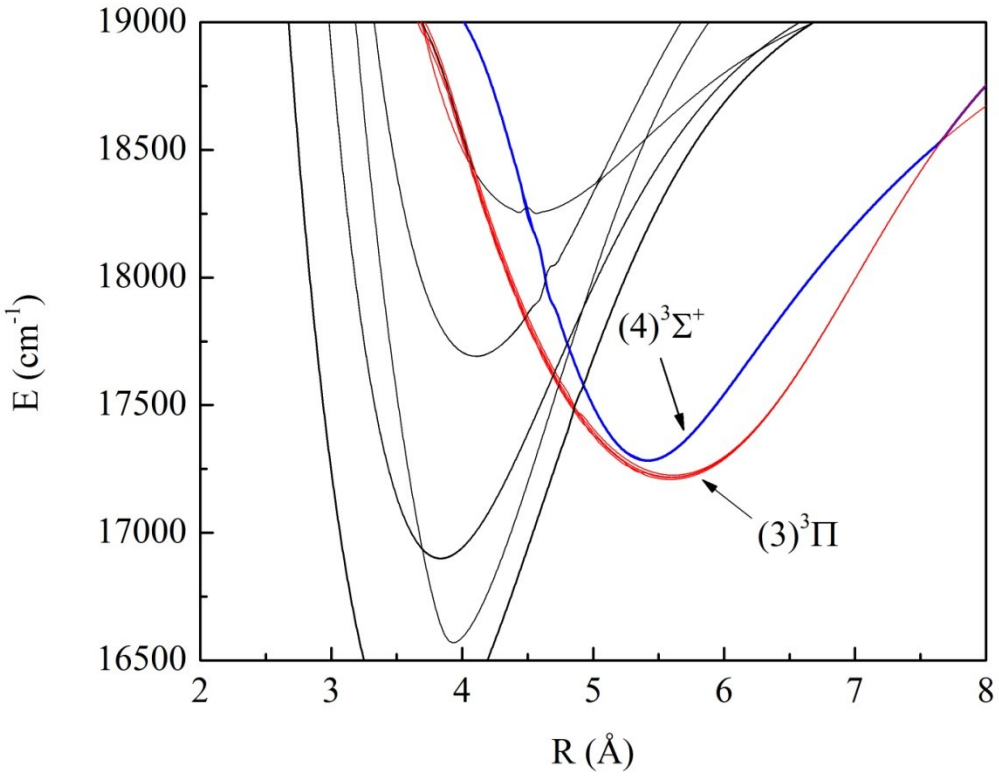

Figure 4.7. Plots of the recalculated diabatic PECs. In our studies, we identify excited state vibrational level progressions associated with the $(3)^3\Pi$ (red) and $(4)^3\Sigma^+$ states (blue).

For each vibrational level in Table 4.2, the calculated energies appear on average approximately 62-66 cm^{-1} lower than the experimental energies. However, the calculated ΔG_{th} are in good agreement with experiment, and in our final analysis, we shift the calculated vibrational energies by adding the average of $(E_{exp} - E_{th})$. Finally, we would like to mention that we list the $\Omega = 0^+$ calculated energies only and not both 0^+ and 0^- for comparison with observed $\Omega = 0$ transitions. We have calculated the difference ΔG_{th} $(\Omega = 0^+) - \Delta G_{th}$ $(\Omega = 0^-)$ which is at most ~1.5%. When compared with a difference of ~4% between theory and experiment, our use of only one $\Omega = 0$ component is valid.

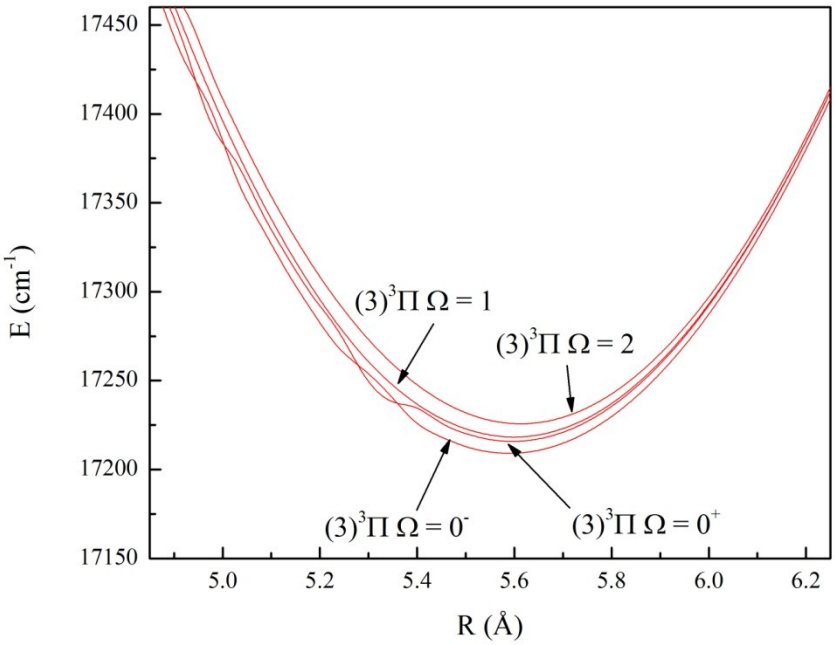

Figure 4.8. Close-up view of the $(3)^3\Pi$ state showing the $(3)^3\Pi$ spin-orbit splitting.

Table 4.1. Calculated energy of the $(3)^3\Pi$ Ω components and the energy difference ΔE_Ω at the equilibrium internuclear spacing R_e = 5.6 Å.

Ω	E_{min} (cm^{-1})	ΔE_Ω (cm^{-1})
0^-	17209.2	6.7
0^+	17215.9	2.4
1	17218.3	7.7
2	17226.0	

Table 4.2 Comparison between theoretical and experimental ΔG for $(3)^3\Pi$ spin-orbit components. E_{exp} are listed for ($v'' = 13$) – v_Π' transitions. The line position corresponding to $\Omega = 2$, $v = 5$ falls close to the Rb^+ line, and is labeled as such.

$\Omega = 0$ $v_\Pi' \downarrow$	Theory E_{th} (cm^{-1})	ΔG_{th} (cm^{-1})	Exp. E_{exp} (cm^{-1})	ΔG_{exp} (cm^{-1})
0	17250.4	69.7	17330.3	68.4
1	17320.1	70.8	17398.7	70.9
2	17390.9	69.9	17469.6	69.0
3	17460.8	69.2	17538.6	67.4
4	17530.0	70.1	17606.0	69.5
5	17600.1	69.1	17675.5	68.6
6	17669.2	68.3	17744.1	67.4
7	17737.5	68.1	17811.5	67.6
8	17805.6	67.3	17879.1	66.2
9	17872.9	67.1	17945.3	66.2
10	17940.0		18011.5	
$\Omega = 1$				
0	17253.3	70.3	17332.5	69.4
1	17323.6	70.6	17401.9	69.9
2	17394.2	70.3	17471.8	69.4
3	17464.5	69.9	17541.2	68.1
4	17534.4	69.5	17609.3	69.2
5	17603.9	69.1	17678.5	69.0
6	17673.1	68.7	17747.5	67.5
7	17741.8	68.3	17815.0	67.9
8	17810.1	67.8	17882.9	65.9
9	17878.0	67.3	17948.8	66.6
10	17945.2		18015.4	
$\Omega = 2$				
0	17261.1	70.6	17334.7	69.7
1	17331.7	70.3	17404.4	69.9
2	17402.0	69.9	17474.3	69.4
3	17471.9	69.5	17543.7	69.0
4	17541.5	69.4	17612.7	
5	17610.9	69.5	Rb^+	
6	17680.4	69.3	17750.5	67.5
7	17749.7	68.3	17818.0	68.2
8	17818.0	67.4	17886.2	66.5
9	17885.4	67.2	17952.7	66.5
10	17952.6		18019.2	

4.5 $a^3\Sigma^+$ vibrational structure

We assign $a^3\Sigma^+$ v'' levels by examining line positions in v_{PA} = 5, 9 and 11 REMPI spectra and comparing our observations with $\Delta G_{v''}$ calculated from the analytic $a^3\Sigma^+$ PEC of Ivanova et.al. [42]. Experimental $\Delta G_{v''}$ most closely match calculated $\Delta G_{v''}$ for v'' = 7 – 13. In Table 4.3 we compare the calculated vibrational energy spacing $\Delta G_{v''}$ with observation. Entries in the column titled $\Delta G_{v''}$ (Exp.) are the average of observed vibrational spacing for all three $(3)^3\Pi_\Omega$ spin-orbit components. From comparison of the three sets of REMPI spectra, transitions to $(3)^3\Pi$ from v'' = 13 and 9 are stronger for v_{PA} = 5 spectra, whereas v'' = 11 and 8 are stronger for v_{PA} = 11 spectra. v_{PA} = 9 shows good signal for v'' = 12 transitions. $a^3\Sigma^+$ (v'' = 7) – $(3)^3\Pi$ v_Π' features are weaker than the abovementioned transitions for all three spectra. We observe that many v'' = 10 transitions are partially obscured by the overlap with stronger v'' = 11 lines. These transitions are most clearly observed in the 17440 – 17600 cm^{-1} range and labeled in Figure 4.5 (b).

Table 4.3. $a^3\Sigma^+$ vibrational levels and energies (measured from the Li(2s) + Rb(5s) asymptote: E_d) calculated from the analytic PEC of [42]. The calculated vibrational spacing ($\Delta G_{v''}$ (Th.)) is compared with experimental results ($\Delta G_{v''}$ (Exp.)) and shows very good agreement.

v''	$(E_{v''} - E_d)$ (cm^{-1})	$\Delta G_{v''}$ (Th.)	$\Delta G_{v''}$ (Exp.)	$\Delta G_{v''}$ (Th.) – $\Delta G_{v''}$ (Exp.)
7	-57.0	16.7	16.6	0.1
8	-40.3	13.6	13.7	-0.1
9	-26.7	10.4	10.4	0.0
10	-16.3	7.5	7.7	-0.2
11	-8.8	5.0	4.7	0.3
12	-3.8	2.6	2.8	-0.2
13	-1.1	1.0	--	--
14	-0.1	--	--	--

Transitions from v'' = 13, 12 and 11, are strongest in REMPI spectra from v_{PA} = 5, 9 and 11, respectively. This strongly suggests the underlying reason for the different line strengths as the varying wavefunction overlap between the v_{PA} levels and v''. The strength of these v_{PA} – v'' transitions can be qualitatively explained by Franck-Condon factors (FCF) for transitions from the initial PA vibrational levels to the ground triplet state v''. These FCFs are calculated using the $2(0^-)$ *ab initio* potential from Korek et.al. and the $a^3\Sigma^+$ potential from Ivanova et.al. Figure 4.9

shows FCFs from v_{PA} = 5, 9 and 11 to $a^3\Sigma^+$ *v"*. We can clearly see that the FCFs for deeper PA levels are larger for more deeply bound ground state vibrational levels, and conclude that for v_{PA} with increasing binding energy have a better wavefunction overlap with more deeply bound *v"*. We should mention here that the FCF calculations are fairly sensitive to the shape of involved potential energy curves and the strength of an observed transition will not necessarily be reflected in the calculated FCF values [78, 79]. Nevertheless, these calculations provide a reasonable qualitative explanation for our observations.

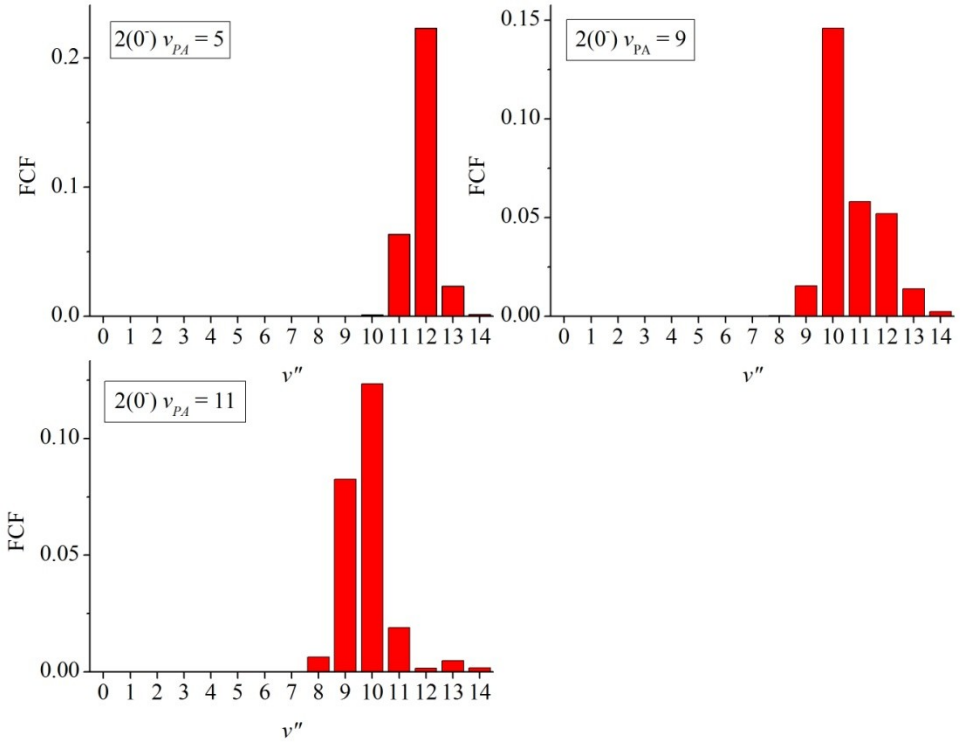

Figure 4.9. Calculated Franck-Condon factors (FCF) for transition from the three PA levels to $a^3\Sigma^+$ vibrational levels. For PA resonances with large binding energies, FCF is larger for decay to lower (deeper bound) *v"* levels.

Table 4.4 lists assigned transitions from v'' = 7 – 13 to v_Π' = 0 – 10 for Ω = 0, 1 and 2. Transitions marked in red denote weak REMPI signal. For a more general comparison between experimental line assignments and theoretical prediction, we recalculate the v'' – v_Π' transition energies with reference to the Li(2s) + Rb(5s) asymptote, and calculate the average vibrational spacing $\Delta G_{v'}$ for each spin-orbit component Ω = 0, 1 and 2. These results are presented in Tables 4.5 – 4.7. Also shown in these tables are the differences between theoretical and experimental ΔG. Entries in the columns labeled E_{th} (theoretical vibrational energies) are calculated as follows: we shift up the vibrational energies calculated from LEVEL by adding to them the average of $(E_{exp} - E_{th})$ for each spin-orbit component. We graphically compare ΔG_{th} and $\Delta G_{v'}$ as a function of energy (in cm^{-1}) in Figure 4.10 and remark that the comparison between observed and calculated vibrational level spacing is very good.

This concludes our presentation of observed $a^3\Sigma^+$ v'' – $(3)^3\Pi_\Omega$ v_Π' transitions. Based on our observations, we have assigned REMPI spectral lines from $a^3\Sigma^+$ v'' = 7 – 13 to $(3)^3\Pi_\Omega$ v_Π' = 0 – 10, where Ω = 0, 1 and 2. Comparison of our results with theory shows good agreement of the vibrational line spacing ΔG for both $a^3\Sigma^+$ and $(3)^3\Pi_\Omega$ states.

In the next section, we discuss most of the REMPI lines that are not assigned to $a^3\Sigma^+$ v'' – $(3)^3\Pi_\Omega$ v_Π' transitions and compare our line assignment with theoretical calculations.

Table 4.4. List of observed $a^3\Sigma^+ v''$ – $(3)^3\Pi_\Omega v_\Pi'$ transitions. All wavelengths and level spacing are in units of cm^{-1}. Transitions in red denote weak REMPI signal.

$\Omega \rightarrow$ $a^3\Sigma^+ v'' \rightarrow$ $v' \downarrow$	0 13 E_{exp}	$\Delta G_{v'}$	1 13 E_{exp}	$\Delta G_{v'}$	2 13 E_{exp}	$\Delta G_{v'}$
0	17323.1	68.3	17324.9	69.4	17327.0	69.9
1	17391.4	70.1	17394.3		17396.9	
2	17461.5	69.5				
3	17531.0	67.6	17533.9	68.1	17536.1	69.2
4	17598.6	69.8	17602.0	68.6	17605.3	69.1
5	17668.4	68.2	17670.6	69.4	17674.4	68.6
6	17736.6	67.4	17740.0	67.4	17743.0	67.4
7	17804.0	67.1	17807.4	67.5	17810.4	67.9
8	17871.1	66.3	17874.9	66.4	17878.3	67.0
9	17937.4	66.9	17941.3	66.9	17945.3	66.3
10	18004.3		18008.2		18011.6	
	12	$\Delta G_{v'}$	12	$\Delta G_{v'}$	12	$\Delta G_{v'}$
0			17328.5		17329.9	70.2
1	17394.3				17400.1	69.5
2			17467.0	69.4	17469.6	69.5
3	17533.8	67.7	17536.4	68.4	17539.1	68.7
4	17601.5	68.9	17604.8	69.0	17607.8	68.9
5	17670.4	69.0	17673.8	69.0	17676.7	69.1
6	17739.4	67.5	17742.8	67.5	17745.8	67.6
7	17806.9	67.3	17810.3	67.3	17813.4	67.6
8	17874.2		17877.6		17881.0	67.3
9					17948.3	66.4
10	18006.9		18010.4		18014.7	
	11	$\Delta G_{v'}$	11	$\Delta G_{v'}$	11	$\Delta G_{v'}$
0	17330.3	68.4	17332.5	69.4	17334.7	69.7
1	17398.7	70.9	17401.9	69.9	17404.4	69.9
2	17469.6	69.0	17471.8	69.4	17474.3	69.4
3	17538.6	67.4	17541.2	68.1	17543.7	69.0
4	17606.0	69.5	17609.3	69.2	17612.7	
5	17675.5	68.6	17678.5	69.0	Rb^+	
6	17744.1	67.4	17747.5	67.5	17750.5	67.5
7	17811.5	67.6	17815.0	67.9	17818.0	68.2
8	17879.1	66.2	17882.9	65.9	17886.2	66.5
9	17945.3	66.2	17948.8	66.6	17952.7	66.5
10	18011.5		18015.4		18019.2	

Table 4.4 cotinued

	10	$\Delta G_{v'}$	10	$\Delta G_{v'}$	10	$\Delta G_{v'}$
0			17341.1	68.1	17342.8	69.7
1	17406.3	70.2	17409.2	70.3	17412.5	69.2
2	17476.5	70.2	17479.5	69.4	17481.7	69.8
3	17546.7	67.1	17548.9	68.2	17551.5	69.3
4	17613.8		17617.1		17620.8	69.0
5	Rb^+		Rb^+		17689.8	68.2
6	17752.0	67.5	17755.0	67.2	17758.0	67.4
7	17819.5	67.2	17822.2	68.4	17825.4	68.5
8	17886.7	66.6	17890.6	65.5	17893.9	66.9
9	17953.3	65.2	17956.1	66.3	17960.8	65.7
10	18018.5		18022.4		18026.5	
	9	$\Delta G_{v'}$	9	$\Delta G_{v'}$	9	$\Delta G_{v'}$
0	17348.2	69.0	17350.4	70.1	17352.9	70.2
1	17417.2	69.6	17420.5	69.2	17423.1	69.6
2	17486.8	69.9	17489.7	69.6	17492.7	69.2
3	17556.7	67.5	17559.3	69.0	17561.9	69.0
4	17624.2	70.1	17628.3	68.6	17630.9	68.7
5	17694.3	67.6	17696.9	68.0	17699.6	68.7
6	17761.9	67.5	17764.9	68.3	17768.3	67.6
7	17829.4	67.7	17833.2	67.7	17835.9	68.2
8	17897.1	67.3	17900.9	66.2	17904.1	66.9
9	17964.4	63.8	17967.1	66.1	17971.0	66.8
10	18028.2		18033.2		18037.8	
	8	$\Delta G_{v'}$	8	$\Delta G_{v'}$	8	$\Delta G_{v'}$
0						
1	17430.7	70.1	17433.3	70.4	17436.2	
2	17500.8	70.3	17503.7	69.6		
3	17571.1	66.6	17573.3	67.8	17575.5	
4	17637.7	70.2	17641.1	69.4		
5	17707.9	67.6	17710.5	68.0	17713.9	68.4
6	17775.5	68.2	17778.5	69.0	17782.3	68.3
7	17843.7	66.8	17847.5	66.9	17850.6	67.3
8	17910.5	66.7	17914.4	66.3	17917.9	66.4
9	17977.2		17980.7		17984.3	
10						

Table 4.4 continued

	7	$\Delta G_{v'}$	7	$\Delta G_{v'}$	7	$\Delta G_{v'}$
0						
1	17448.0	69.0	17451.3	69.0	17452.4	
2	17517.0	70.1	17520.3	69.7		
3	17587.1	66.3	17590.0	68.2	17592.7	68.9
4	17653.4	71.5	17658.2	68.9	17661.6	68.6
5	17724.9	67.0	17727.1	68.1	17730.2	68.5
6	17791.9	67.7	17795.2	68.3	17798.7	67.8
7	17859.6	67.0	17863.5	67.7	17866.5	67.8
8	17926.6	67.6	17931.2	66.1	17934.3	66.9
9	17994.2		17997.3		18001.2	
10						

Table 4.5. Comparison between theoretical (ΔG_{th}) and experimental (ΔG_{exp}) vibrational spacing for $(3)^3\Pi$ $\Omega = 0$. E_{th} energies are shifted up by the average of ($E_{th} - E_{exp}$) for $v_\Pi' = 0 - 10$. E_{exp} are referenced to the Li(2s) + Rb (5s) asymptote. All energies and vibrational spacing are in cm^{-1}.

v_Π'	E_{th}	ΔG_{th}	E_{exp}	ΔG_{exp}	ΔG_{th} - ΔG_{exp}
0	17317.5	69.7	17321.9	68.5	1.2
1	17387.2	70.8	17390.4	70.0	0.9
2	17458.0	69.9	17460.3	69.8	0.1
3	17527.9	69.2	17530.2	67.2	2.0
4	17597.0	70.1	17597.3	70.0	0.2
5	17667.2	69.1	17667.3	68.1	1.0
6	17736.3	68.3	17735.4	67.6	0.7
7	17804.6	68.1	17803.0	67.2	0.9
8	17872.7	67.3	17870.2	66.7	0.5
9	17940.0	67.1	17936.9	65.6	1.5
10	18007.1		18002.6		

Table 4.6. Comparison between theoretical (ΔG_{th}) and experimental (ΔG_{exp}) vibrational spacing for $(3)^3\Pi\ \Omega = 1$. E_{th} energies are shifted up by the average of ($E_{th} - E_{exp}$) for $v_\Pi' = 0 - 10$. E_{exp} are referenced to the Li(2s) + Rb (5s) asymptote. All energies and vibrational spacing are in cm^{-1}.

v'	E_{th}	ΔG_{th}	E_{exp}	ΔG_{exp}	$\Delta G_{th} - \Delta G_{exp}$
0	17319.5	70.3	17324.2	69.2	1.1
1	17389.8	70.6	17393.4	69.8	0.8
2	17460.4	70.3	17463.2	69.5	0.8
3	17530.7	69.9	17532.7	68.3	1.6
4	17600.6	69.5	17601.0	69.0	0.6
5	17670.1	69.1	17670.0	68.6	0.5
6	17739.3	68.7	17738.6	67.9	0.8
7	17808.0	68.3	17806.5	67.6	0.7
8	17876.3	67.8	17874.1	66.1	1.7
9	17944.2	67.3	17940.2	66.4	0.9
10	18011.4		18006.6		

Table 4.7. Comparison between theoretical (ΔG_{th}) and experimental (ΔG_{exp}) vibrational spacing for $(3)^3\Pi\ \Omega = 2$. E_{th} energies are shifted up by the average of ($E_{th} - E_{exp}$) for $v_\Pi' = 0 - 10$. E_{exp} are referenced to the Li(2s) + Rb (5s) asymptote. All energies and vibrational spacing are in cm^{-1}.

v'	E_{th}	ΔG_{th}	E_{exp}	ΔG_{exp}	$\Delta G_{th} - \Delta G_{exp}$
0	17322.8	70.6	17326.1	69.8	0.8
1	17393.4	70.3	17396.0	69.9	0.4
2	17463.7	69.9	17465.9	69.3	0.6
3	17533.6	69.5	17535.2	69.1	0.5
4	17603.2	69.4	17604.3	69.0	0.5
5	17672.6	69.5	17673.2	68.6	0.9
6	17742.1	69.3	17741.8	67.7	1.6
7	17811.4	68.3	17809.5	67.9	0.4
8	17879.7	67.4	17877.4	66.8	0.6
9	17947.1	67.2	17944.2	66.4	0.8
10	18014.4		18010.6		

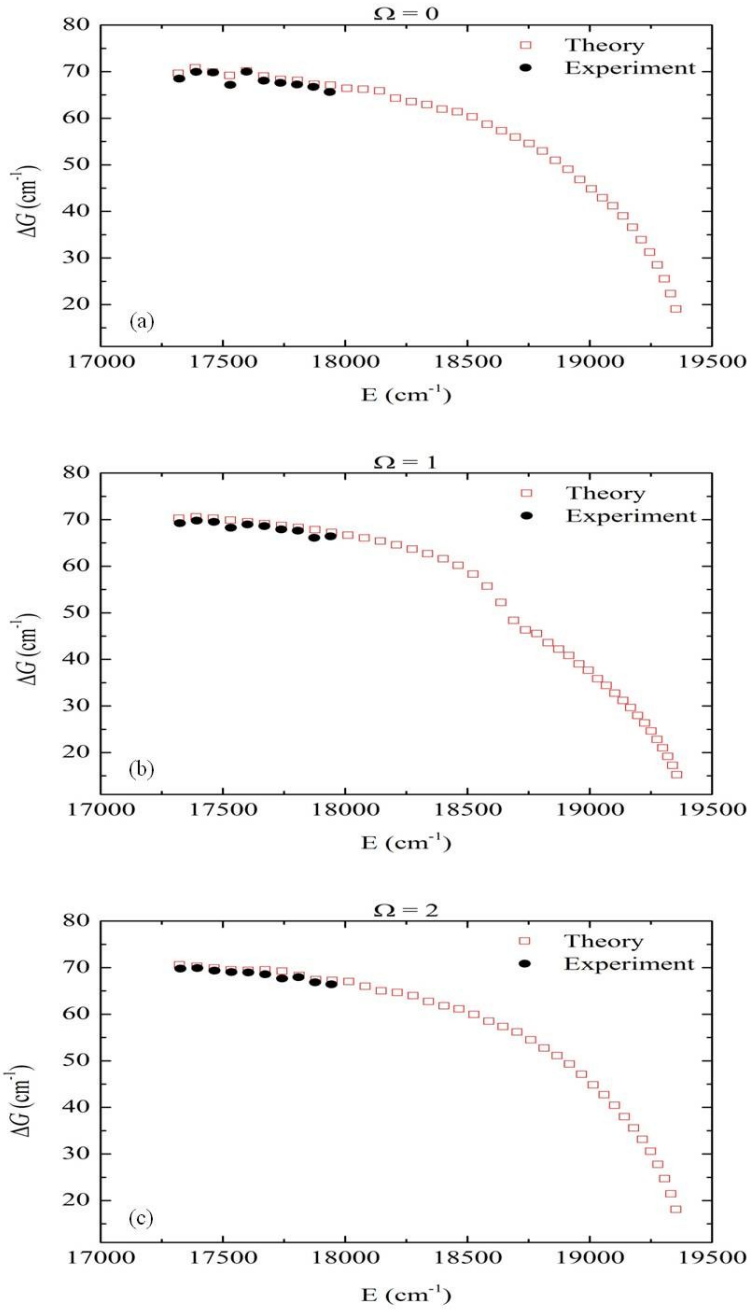

Figure 4.10. Comparison between calculated and observed (3)$^3\Pi$ $\Delta G_{v'}$ for (a) Ω = 0, (b) Ω = 1 and (c) Ω = 2. Theoretical calculations (red open squares) are based on the diabatic PECs and calculated using LEVEL. The experimental data points (black closed circles) are each plots of ΔG_{exp} for Ω = 0, 1 and 2 from Tables 4.5, 4.6 and 4.7, respectively.

4.6 Assignment of $(4)^3\Sigma^+$ vibrational levels

In addition to the $(3)^3\Pi_\Omega$ vibrational levels, we also observe and assign $v_\Sigma' = 0 - 5$ vibrational levels of the $(4)^3\Sigma^+$ state (see Figure 4.5). The $(4)^3\Sigma^+$ diabatic PEC is shown as the blue curve in Figure 4.7. Unlike the triplet structure originating from spin-orbit splitting of the $(3)^3\Pi$ state, we do not observe the $\Omega = 0^-$ and 1 components for $(4)^3\Sigma^+$. The calculated spin-orbit splitting for this state is also smaller: at the equilibrium internuclear spacing $R_e \sim 5.4$ Å, the two spin-orbit states are split by less than 1 cm^{-1}.

In Table 4.8, we list all of the observed $a^3\Sigma^+ v'' - (4)^3\Sigma^+ v_\Sigma'$ transitions. In addition, we compare the calculated $(4)^3\Sigma^+$ vibrational spacing with experiment in Table 4.9. The calculated vibrational level energies are shifted up by the average of $(E_{th} - E_{exp})$. Entries listed under ΔG_{exp} are calculated by determining the v_Σ' energies for all v'' with respect to the Li(2s) + Rb(5s) asymptote and taking the average. Again, the agreement between experimental line spacing and calculated line spacing is good. This comparison between theory and experiment is shown graphically in Figure 4.11.

4.7 Conclusion

In this chapter, we have presented results of REMPI spectroscopy performed in ultracold LiRb molecules. We have compared spectra recorded by fixing the PA laser at three different resonances, $2(0^-)$ $v = 5$, 9 and 11. We have labeled transitions from $a^3\Sigma^+$ ($v'' = 7 - 13$) to $(3)^3\Pi$ ($v_\Pi' = 0 - 10$). Furthermore, we have also identified lines corresponding to $a^3\Sigma^+$ ($v'' = 7 - 13$) – $(4)^3\Sigma^+$ ($v_\Sigma' = 0 - 5$) transitions. Overall, we have identified ~94% of the lines experimentally observed in our REMPI spectra.

At this point, we do not have sufficient information to explain the origin of the unassigned lines. However, we would like to point out that there are several electronic states – besides the two we have studied – that may be accessible by our REMPI laser, as seen in Figure 4.7. For our goal of populating the rovibronic ground state, the $(5)^1\Sigma^+$ state seems to be the most promising, as its equilibrium internuclear spacing R_e of ~3.9 Å (7.4 a_0) is near $R_e \sim 3.5$ Å (6.6 a_0) of the $X^1\Sigma^+$ ground state. From Korek et. al. [50], this state is predicted to cross the $(3)^3\Pi$ state, although in our studies, we have not observed influence of the $(5)^1\Sigma^+$ state on the observed $(3)^3\Pi$ levels. If there is an interaction observed between the two states, possible singlet-triplet mixing could lead

to a pathway to create deeply bound ground singlet state molecules. Further investigation in this direction may be warranted.

Table 4.8. List of $a^3\Sigma^+$ v'' – $(4)^3\Sigma^+$ v_Σ' transitions. All wavelengths and level spacing are in units of cm^{-1}. Transition energies in red denote weak signal.

$a^3\Sigma^+$ $v''\rightarrow$ $(4)^3\Sigma^+$ $v_\Sigma'\downarrow$	13	$\Delta G_{v'}$	12	$\Delta G_{v'}$	11	$\Delta G_{v'}$	10	$\Delta G_{v'}$
0	17412.5	101.2			17419.8	101.5	17427.8	101.6
1	17513.7	97.2	17516.6	97.1	17521.3	97.3	17529.4	97.4
2	17610.9	91.7	17613.7	91.5	17618.6	91.9	17626.8	91.3
3	17702.6	87.7	17705.2	87.7	17710.5	88.1	17718.1	88.1
4	17790.3	83.1	17792.9	82.8	17798.6	82.4	17806.2	82.5
5	17873.4		17875.7		17881.0		17888.7	
	9	$\Delta G_{v'}$	8	$\Delta G_{v'}$	7	$\Delta G_{v'}$		
	17438.8	101.0	17452.4	100.2	17469.6	100.0		
	17539.8	97.4	17552.6	98.6	17569.6	97.7		
	17637.2	91.8	17651.2	91.8	17667.3	92.3		
	17729.0	87.9	17743.0	87.4	17759.6	87.5		
	17816.9	81.7	17830.4	81.7	17847.1	81.6		
	17898.6		17912.1		17928.7			

Table 4.9. Comparison between theoretical (ΔG_{th}) and experimental (ΔG_{exp}) vibrational spacing for $(4)^3\Sigma^+$. E_{th} energies are shifted up by the average of (E_{th} – E_{exp}) for $v_\Sigma' = 0 - 5$. E_{exp} are referenced to the Li(2s) + Rb (5s) asymptote. All energies and vibrational spacing are in cm^{-1}.

v_Σ'	E_{th}	ΔG_{th}	E_{exp}	ΔG_{exp}	ΔG_{th} - ΔG_{exp}
0	17407.4	103.0	17411.8	100.9	2.0
1	17510.4	98.0	17512.7	97.5	0.5
2	17608.4	94.2	17610.3	91.8	2.4
3	17702.6	89.5	17702.0	87.8	1.7
4	17792.1	85.7	17789.8	82.3	3.4
5	17877.7		17872.0		

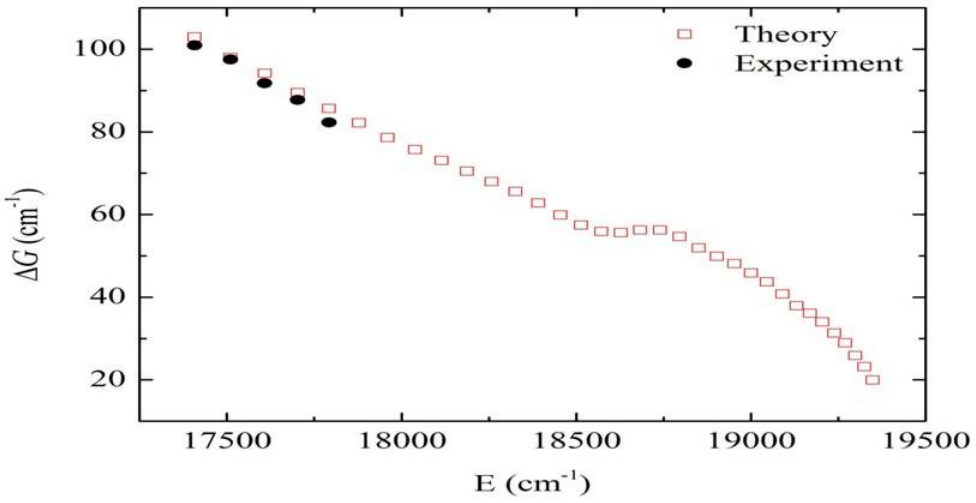

Figure 4.11. Comparison between calculated and observed $(4)^3\Sigma^+$ $\Delta G_{v'}$. Theoretical calculations (red open squares) are based on the diabatic PECs and calculated using LEVEL. The experimental data points (black closed circles) are taken from ΔG_{exp} in Table 4.9.

5. CONCLUSION AND OUTLOOK

We have presented the first set of experiments on ultracold LiRb with ionization spectroscopy as the primary detection mechanism. We have demonstrated the utility of this approach in discovering PA resonances at large binding energy that could not be detected by trap-loss spectroscopy. Ion detection has also proven immensely useful in our efforts to not only explore excited electronic states of LiRb, but also to identify ground electronic vibrational levels. In this chapter, we discuss our goals for the ultracold LiRb project, and also discuss technical improvements that may prove beneficial for future projects.

5.1 Resolving ground and excited state rotational structure

Acquiring knowledge of rotational structure in the ground and excited electronic states is required for our planned experiments involving superposition of rotational states. While REMPI spectroscopy works well to detect vibrational levels of the ground and excited electronic states, the laser linewidth prohibits rotational structure from being resolved. Wang et.al. [84] demonstrated the technique of cw depletion spectroscopy to resolve rotational structure in both ground and excited state vibrational levels. The technique works as follows: the PA laser is fixed on a known resonance, and the REMPI laser ionizes the formed LiRb molecules from the initial *v"*, *J"* ground level, via an intermediate *v'*, *J'* level. An additional cw laser is applied to the molecules to transfer molecules from the *v", J"* level to a different excited level *v'''*, *J'''*. Because the cw laser is transferring molecules out of *v", J"* and into *v'''*, *J'''*, the ground *v"*, *J"* population is depleted and causes a decreases in the REMPI ion signal.

Since we are already performing REMPI experiments on our setup, we only need an additional cw laser for depletion spectroscopy. Fortunately, we have at our disposal a homemade tunable cw ring dye laser (lasing between 555 and 610 nm, ~30 mW output power) that was earlier used to perform LiRb heat pipe spectroscopy of the $B^1\Pi$ state [43]. This state is also expected to have an avoided crossing with the $(2)^3\Sigma^+$ state [50], which would introduce triplet character to the *B* state

(and vice versa) and result in an allowed $a - B$ transition. We have identified rotational and vibrational structure in the B state from this study and we can tune the cw dye laser to a particular $B^1\Pi$ rovibrational level and identify the $a^3\Sigma^+$ v', J' level. A schematic of this scheme is shown in Figure 5.1. Rotational level information gleaned from depletion spectroscopy will also be useful for experiments involving rotational superposition states of the $a^3\Sigma^+$ state, as discussed next.

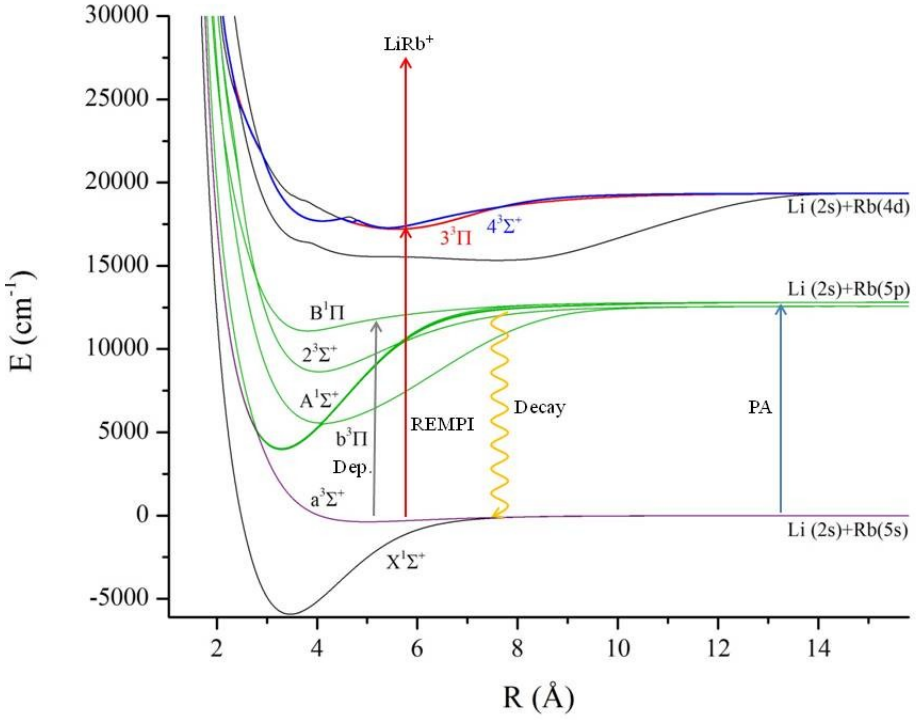

Figure 5.1. Schematic for depletion spectroscopy to resolve ground state rotational structure. A cw depletion laser (dep., gray arrow) is resonant between the a and B states due to $(2)^3\Sigma^+ - B^1\Pi$ singlet-triplet mixing, and reduces the REMPI ion signal in the process. The PA and REMPI steps are unchanged from the discussion in Chapter 4.

5.2 Coherent control of polar LiRb molecules

Over the last two decades, our lab has become proficient at coherent control experiments involving atomic systems [85, 86]. We are interested in applying coherent control towards ultracold polar molecules to create a superposition of rotational levels and study their time evolution. If we have molecules in two rotational levels $|J=0\rangle$ and $|J=1\rangle$, the superposition of

these two states can be written as $|\Psi\rangle = a|0\rangle + be^{-i\Delta Et/\hbar}|1\rangle$, where a and b are probability amplitudes, and $\Delta E = 2B_v$ is the energy splitting between $|0\rangle$ and $|1\rangle$ with rotational constant B_v. $|\Psi\rangle$ now evolves over a period $1/(2B_v)$. This superposition state can be created by coupling the two rotational levels with phase coherent light fields, as shown in Figure 5.2.

For practical implementation of this proposal, we can couple rotational levels of $a^3\Sigma^+$ $v'' = 11$, for example. To do this, we use a two-photon Raman transition to the $(1)^3\Pi$ v', $J' = 2$ level. $(1)^3\Pi$ corresponds to the 1(2) state in Hund's case (c) notation, and has been identified in our PA spectroscopy. The $a^3\Sigma^+ - b^3\Pi$ transition wavelength is ~780 nm, which is equivalent to two ~1560 nm photons. We have an ECDL seeded fiber amplifier that operates in the 1545 – 1565 nm range that would provide the ω light. The 2ω light can easily be generated using one of our homemade 780 nm ECDLs.

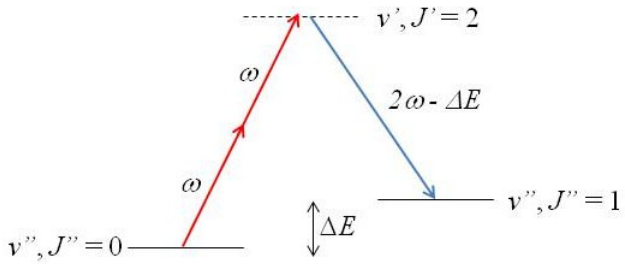

Figure 5.2. Schematic showing coupling between the $|0\rangle$ and $|1\rangle$ rotational levels using phase-coherent one- and two-photon light fields.

In order to create the superposition state, phase coherence between the ω and 2ω lasers is critical. One approach is shown in Figure 5.3. The 780 nm (ω) ECDL is modulated at $2B_v$ using well known microwave modulation techniques. At the same time, part of the 1560 nm (2ω) fiber amplifier output is frequency doubled and injection locked to the lower sideband of the 780 nm laser, creating phase coherence and hence rotational superposition states. We have already demonstrated frequency doubling of the 1560 nm laser (see Chapter 2).

Once the molecules are created in the superposition state, we need a probe to observe the time evolution of the superposition. Since the rotational frequencies are on the order of a few hundred MHz, the pulse width of the ionizing probe laser has to be much less than a few ns, on the order

of picoseconds or less. Thanks to Dr. Andrew Weiner and Dr. Daniel Leaird, we have acquired and assembled a femtosecond (fs) mode-locked Ti:Sapphire laser that is ideally suited for our needs. The laser generates ~100 fs pulses and currently operates at a 93 MHz repetition rate, as shown in Figure 5.4. The repetition rate can be adjusted to a multiple of $\Delta E = 2B_v$ by changing the position of the output coupler. Finer adjustments can be made by attaching a PZT to the output coupler mirror mount.

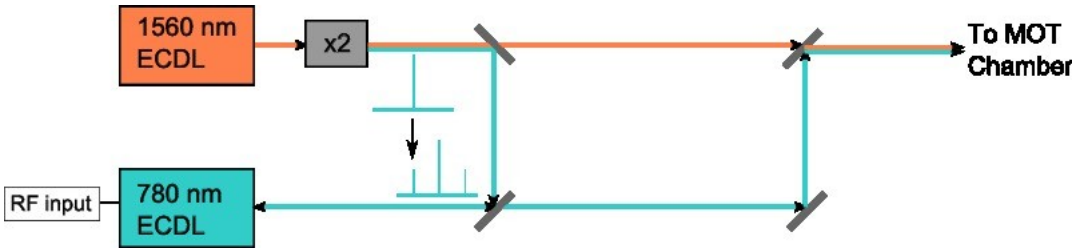

Figure 5.3. Proposal for creating phase coherence between the ω and 2ω fields. The frequency double output of the 1562 nm ECDL is injection locked to the rf generated lower sideband at $2B_v$.

Once we fix the repetition rate, pulses from the fs Ti:S will ionize the molecules at the same instance of the evolution of the superposition state, and create Li^+ and Rb^+ ions. Our MCP assembly includes a phosphor screen that can image the spatial distribution of incident ion species. Without superposition, the Li^+ and Rb^+ images would be circularly symmetric images, and distinguishable from each other based on the image size: lighter Li^+ ions will have the higher velocity compared to Rb^+ and strike the phosphor screen farther off center than Rb^+ ions. Evidence of rotational superposition states will be indicated by an asymmetry in the circular pattern. Eventually, we would like to create the rotational superposition states in deeply bound vibrational levels of the ground $X^1\Sigma^+$ in hope of implementing a scheme similar to the one proposed by DeMille [4].

Next, we will discuss possible improvements and additions to the apparatus that can improve future experiments.

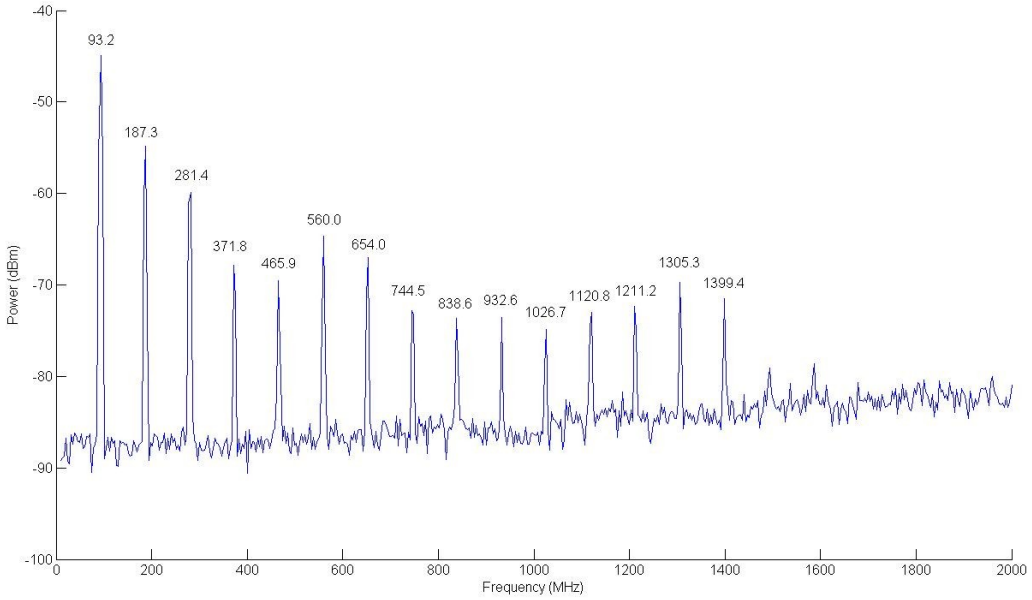

Figure 5.4. Rf spectrum analyzer output showing the 93.2 MHz repetition rate of the fs Ti:S and its harmonics. This spectrum was recorded with a fast (~GHz bandwidth) photodetector connected to the spectrum analyzer. We can adjust the repetition rate by changing the position of the output coupler. A PZT attached to the output coupler can provide finer adjustments to the repetition rate.

5.3 Modifications to MOT apparatus

Since the first observation of $LiRb^+$, we have spent considerable time and effort to improve our signal detection, with room for further improvement. Steering ions towards the MCP assembly by using permanent magnets was a simple yet effective means to increase signal. We roughly positioned the magnets in the location where the $LiRb^+$ signal was maximized. A more systematic means of steering the ions may be to use a set of frame mounted electromagnets that can be more conveniently adjusted. Another advantage of using electromagnets would be the fine tuning available to adjust the magnetic field for maximum ion counts.

To generate the cooling and repump frequencies for the Li MOT, we use a nonresonant EOM that requires a 6 W rf amplifier. We have noticed that the heated crystal can distort the beam shape to

the extent that the PM fiber coupling efficiency drops by ~20% or more. This in turn reduces the Li MOT number and density and can weaken our signal. To alleviate this problem, we can replace the current EOM with a resonant LC circuit EOM that requires significantly lower power for similar modulation depth (~1 W or less).

Another upgrade that would boost the ionization signal would be higher PA power. The PA rate depends, among other things, on the PA laser intensity. Currently, we get a maximum of ~450 – 500 mW of PA power on (very few) good days. The Ti:S pump laser has a maximum output of 8 W. Upgrading to a higher power pump laser would provide a significant boost to PA power. Combined with improved ion steering and a more stable EOM, the increased PA power should aid the search for new, more deeply bound PA resonances.

LIST OF REFERENCES

LIST OF REFERENCES

1. Krems, R. V. Cold controlled chemistry. *Phys. Chem. Chem. Phys.* **10**, 4079 (2008).
2. Moore, M. G. & Vardi, A. Bose-Enhanced Chemistry: Amplification of Selectivity in the Dissociation of Molecular Bose-Einstein Condensates. *Phys. Rev. Lett.* **88**, 160402 (2002).
3. Ni, K. –K. *et. al.* Dipolar collisions of polar molecules in the quantum regime. *Nature* **464**, 1324 (2010).
4. DeMille, D. Quantum Computation with Trapped Polar Molecules. *Phys. Rev. Lett.* **88**, 067901 (2002).
5. Zadoyan, R. *et. al.* The manipulation of massive ro-vibronic superpositions using time-frequency-resolved coherent anti-Stokes Raman scattering (TFRCARS): from quantum control to quantum computing. *Chem. Phys.* **266**, 323 (2001).
6. Nielsen, M. A. & Chuang, I. L. *Quantum Computation and Quantum Information*. (Cambridge University Press, 2004).
7. Sachdev, S. *Quantum Phase Transitions*. (Cambridge University Press, 1999).
8. Greiner, M. *et. al.* Quantum phase transition from a superfluid to a Mott insulator in a gas of ultracold atoms. *Nature* **415**, 39 (2002).
9. Góral, K., Santos, L. & Lewenstein, M. Quantum Phases of Dipolar Bosons in Optical Lattices. *Phys. Rev. Lett.* **88**, 170406 (2002).
10. Pe'er, A. *et. al.* Precise Control of Molecular Dynamics with a Femtosecond Frequency Comb. *Phys. Rev. Lett.* **98**, 113004 (2007).
11. Shapiro, M. & Brumer, P. W. *Principles of the Quantum Control of Molecular Processes*. (Wiley-Interscience, 2007).
12. Jing, H., Cheng, J. & Meystre, P. Coherent generation of triatomic molecules from ultracold atoms. *Phys. Rev. A.* **77**, 043614 (2008).
13. Hudson, J. J. *et. al.* Measurement of the Electron Electric Dipole Moment Using YbF Molecules. *Phys. Rev. Lett.* **89**, 023003 (2002).

14. Hudson, E. R. *et. al.* Cold Molecule Spectroscopy for Constraining the Evolution of the Fine Structure Constant. *Phys. Rev. Lett.* **96**, 143004 (2006).
15. Chin, C., Flambaum, V. V. & Kozlov, M. G. Ultracold molecules: new probes on the variation of fundamental constants. *New J. Phys.* **11**, 055048 (2009).
16. Micheli, A., Brennen, G. K. & Zoller, P. A toolbox for lattice-spin models with polar molecules. *Nature Phys.* **2**, 341 (2006).
17. Krems, R. *et. al. Cold Molecules: Theory, Experiment, Applications.* (CRC Press, 2009).
18. Weiner, J. *et. al.* Experiments and theory in cold and ultracold collisions. *Rev. Mod. Phys.* **71**, 1 (1999).
19. Walter, J. M. & Barratt, S. The Existence of Intermetallic Compounds in the Vapour State. The Spectra of the Alkali Metals, and of their Alloys with each other. *Proc. R. Soc. Lond. A* **119**, 257 (1928).
20. Stwalley, W. & Wang, H. Photoassociation of Ultracold Atoms: A New Spectroscopic Technique. *J. Mol. Spec.* **195**, 194 (1999).
21. Lett, P. D., Julienne, P. S. & Phillips, W. D. Photoassociative spectroscopy of laser-cooled atoms. *Annu. Rev. Phys. Chem.* **46**, 423 (1995).
22. Hänsch, T. W. & Schawlow, A. L. Cooling of gases by laser radiation. *Opt. Comm.* **13**, 68 (1975).
23. Phillips, W. D. & Metcalf, H. Laser Deceleration of an Atomic Beam. *Phys. Rev. Lett.* **48**, 596 (1982).
24. Chu, S. *et. al.* Three-dimensional viscous confinement and cooling of atoms by resonance radiation pressure. *Phys. Rev. Lett.* **55**, 48 (1985).
25. Raab, E. L. *et. al.* Trapping of Neutral Sodium Atoms with Radiation Pressure. *Phys. Rev. Lett.* **59**, 2631 (1987).
26. Monroe, C. *et. al.* Very cold trapped atoms in a vapor cell. *Phys. Rev. Lett.* **65**, 1571 (1990).
27. Thorsheim H. R., Weiner, J. & Julienne, P. S. Laser-induced photoassociation of ultracold sodium atoms. *Phys. Rev. Lett.* **58**, 2420 (1987).
28. Miller, J. D., Cline, R. A. & Heinzen, D. J. Photoassociation spectrum of ultracold Rb atoms. *Phys. Rev. Lett.* **71**, 2204 (1993).
29. Cline, R. A., Miller, J. D. & Heinzen, D. J. Study of Rb_2 Long-Range States by High-Resolution Photoassociation Spectroscopy. *Phys. Rev. Lett.* **73**, 632 (1994).

30. Wang, H., Gould, P. L. & Stwalley, W. C. Photoassociative spectroscopy of ultracold ^{39}K atoms in a high-density vapor-cell magneto-optical trap. *Phys. Rev. A.* **53**, R1216 (1996).
31. Wang, H., Gould, P. L. & Stwalley, W. C. Long-range interaction of the $^{39}K(4s)$ + $^{39}K(4p)$ asymptote by photoassociative spectroscopy. I. The 0_g^- pure long-range state and the long-range potential constants. *J. Chem. Phys.* **106**, 7899 (1997).
32. Abraham, E. R. I. *et. al.* Photoassociative spectroscopy of long-range states of ultracold $^6Li_2$ and $^7Li_2$. *J. Chem. Phys.* **103**, 7773 (1995).
33. Jones, K. M. *et. al.* Direct measurement of the ground-state dissociation energy of Na_2. *Phys. Rev. A.* **54**, R1006 (1996).
34. Fioretti, A. *et. al.* Formation of Cold Cs_2 Molecules through Photoassociation. *Phys. Rev. Lett.* **80**, 4402 (1998).
35. Wang, D. *et. al.* Photoassociative Production and Trapping of Ultracold KRb Molecules. *Phys. Rev. Lett.* **93**, 243005 (2004).
36. Kerman A. J. *et. al.* Production of Ultracold, Polar RbCs* Molecules via Photoassociation. *Phys. Rev. Lett.* **92**, 033004 (2004).
37. Deiglmayr, J. *et. al.* Formation of Ultracold Polar Molecules in the Rovibrational Ground State. *Phys. Rev. Lett.* **101**, 133004 (2008).
38. Haimberger, C. *et. al.* Formation of ultracold, highly polar $X^1\Sigma^+$ NaCs molecules. *New J. Phys.* **11**, 055042 (2009).
39. Ridinger, A. *et. al.* Photoassociative creation of ultracold heteronuclear 6Li40K* molecules. *EPL* (*Europhysics Lett.*) **96**, 33001 (2011).
40. Ni, K. –K. *et. al.* A High Phase-Space-Density Gas of Polar Molecules. *Science* **322**, 231 (2008).
41. Jones, K. M. *et. al.* Ultracold photoassociation spectroscopy: Long-range molecules and atomic scattering. *Rev. Mod. Phys.* **78**, 483 (2006).
42. Ivanova, M. *et. al.* The $X^1\Sigma^+$ state of LiRb studied by Fourier-transform spectroscopy. *J. Chem. Phys.* **134**, 024321 (2011).
43. Dutta, S. *et. al.* Laser spectroscopy of the $X^1\Sigma^+$ and $B^1\Pi$ states of the LiRb molecule. *Chem. Phys. Lett.* **511**, 7 (2011).
44. Bellos, M. A. *et. al.* Formation of ultracold Rb_2 molecules in the v'' = 0 level of the $a^3\Sigma_u^+$ state *via* blue-detuned photoassociation to the $1^3\Pi_g$ state. *Phys. Chem. Chem. Phys.* **13**, 18880 (2011).

45. Menegatti, C. R. *et. al.* Trap loss in a rubidium crossed dipole trap by short-range photoassociation. *Phys. Rev. A.* **87**, 053404 (2013).
46. Herzberg, G. *Molecular Spectra and Molecular Structure. I. Spectra of Diatomic Molecules*. (D. Van Nostrand Company, Inc., 1950).
47. Lefebvre-Brion, H. & Field, R. W. *The Spectra and Dynamics of Diatomic Molecules.* (Elsevier Academic Press, 2004).
48. Bernath, P. F. *Spectra of Atoms and Molecules.* (Oxford University Press, Inc. 2005).
49. Sherrill, D. C. The Born-Oppenheimer Approximation (2005). Available at *http://vergil.chemistry.gatech.edu/notes/bo/bo.pdf*
50. Korek, M., Younes, G. & Al-Shawa, S. Theoretical calculation of the electronic structure of the molecule LiRb including the spin-orbit interaction. *J. Mol. Spec: THEOCHEM* **899**, 25 (2009).
51. Koperski, J. Study of diatomic van der Waals complexes in supersonic beams. *Phys. Reports* **369**, 177 (2002).
52. Somoza, M. M. Depiction of Franck Condon principle in absorption and fluorescence. (2006). Available at *http://en.wikipedia.org/wiki/File:Franck-Condon-diagram.png*.
53. Aymar, M. & Dulieu, O. Calculation of accurate permanent dipole moments of the lowest $^{1,3}\Sigma^{+}$ states of heteronuclear alkali dimers using extended basis sets. *J. Chem. Phys.* **122**, 204302 (2005).
54. Igel-Mann, G. *et. al.* Ground-state properties of alkali dimers XY (X, Y=Li to Cs). *J. Chem. Phys.* **84**, 5007 (1986).
55. Korek, M. *et. al.* Theoretical study of the electronic structure of the LiRb and NaRb molecules. *Chem. Phys.* **256**, 1 (2000).
56. Dutta, S. Experimental Studies of LiRb: Spectroscopy and Ultracold Molecule Formation by Photoassociation. Doctoral dissertation, Purdue University (2013).
57. Ivanova, M. *et. al.* The $B^{1}\Pi$ and $D^{1}\Pi$ states of LiRb. *J. Chem. Phys.* **138**, 094315 (2013).
58. Shuman, E. S., Barry, J. F. & DeMille, D. Laser cooling of a diatomic molecule. *Nature* **467**, 820 (2010).
59. Metcalf, H. J. & van der Straten, P. *Laser Cooling and Trapping*. (Springer, 2001).
60. Gilbert, S. L. & Wieman, C. E. Laser Cooling and Trapping for the Masses. *Photonics News* **4**, 8 (1993).
61. Libbrecht, K. G. *et. al.* Teaching physics with 670 nm diode lasers – construction of stabilized lasers and lithium cells. *Am. J. Phys.* **63**, 729 (1995).

62. Antypas, D. Measurement of a weak transition moment using Coherent Control. Doctoral dissertation, Purdue University (2013).
63. Dutta, S., Elliott, D. S. & Chen, Y. P. Mode-hop-free tuning over 135 GHz of external cavity diode lasers without anti-reflection coating. *Appl. Phys. B.* **106**, 629 (2012).
64. Dutta, S. *et. al.* Interspecies collision-induced losses in a dual species ^{7}Li-^{85}Rb magneto-optical trap. (Submitted 2013). Preprint available at: *http://arxiv.org/abs/1306.5196*
65. Ketterle, W. *et. al.* High densities of cold atoms in a *dark* spontaneous-force optical trap. *Phys. Rev. Lett.* **70**, 2253 (1993).
66. Eppink, A. T. J. & Parker, D. H. Velocity map imaging of ions and electrons using electrostatic lenses: Application in photoelectron and photofragmention imaging of molecular oxygen. *Rev. Sci. Instrum.* **68**, 3477 (1997)
67. Napolitano, R. *et. al.* Line Shapes of High Resolution Photoassociation Spectra of Optically Cooled Atoms. *Phys. Rev. Lett.* **73**, 1352 (1994).
68. Dutta, S. *et. al.* Photoassociation of ultracold LiRb* molecules: observation of high efficiency and unitarity-limited rate saturation. *Phys Rev. A* **89**, 020702(R) (2014).
69. Dutta, S., Elliott, D. S. & Chen, Y. P. Formation of ultracold LiRb molecules by photoassociation near the Li($2s^2S_{1/2}$) + Rb($5p^2P_{1/2}$) asymptote. *EPL* (*Europhys. Lett.*) **104**, 63001 (2014).
70. Grochola, A. *et. al.* Photoassociation spectroscopy of the $B^1\Pi$ state of LiCs. *J. Chem. Phys.* **131**, 054304 (2009).
71. LeRoy, R. J. & Bernstein, R. B. Dissociation Energy and Long-Range Potential of Diatomic Molecules from Vibrational Spacings of Higher Levels. *J. Chem. Phys.* **52**, 3869 (1970).
72. Movre, M. & Beuc, R. van der Waals interaction in excited alkali-metal dimers. *Phys. Rev. A* **31**, 2957 (1985).
73. Bussery, B., Achkar, Y. & Aubert-Frécon, M. Long-range molecular states dissociating to the three or four lowest asymptotes for the ten heteronuclear diatomic alkali molecules. *Chem. Phys.* **116**, 319 (1987).
74. Jones, K. M. *et. al.* Fitting line shapes in photoassociation spectroscopy of ultracold atoms: A useful approximation. *Phys. Rev. A.* **61**, 012501 (1999).
75. Wigner, E. P. On the Behavior of Cross Sections Near Thresholds. *Phys. Rev.* **73**, 1002 (1948).

76. Ovsiannikov, V. D., Glukhov, I. L. & Nekipelov, E. A. Radiative Lifetime and Photoionization Cross-Section for Rydberg States in Alkali-Metal Atoms. *Optics and Spectroscopy* **111**, 25 (2011).
77. LeRoy, R. J. Level 8.0: A Computer Program for Solving the Radial Schrödinger Equation for Bound and Quasibound Levels, University of Waterloo Chemical Physics Research Report CP-663 (2007). See http://leroy.uwaterloo.ca/programs/
78. Banerjee, J. *et. al.* Spectroscopy of the double minimum $3^3\Pi_\Omega$ electronic state of $^{39}K^{85}Rb$. *J. Chem. Phys.* **138**, 164302 (2013).
79. Bergeman, T. *et. al.* Prospects for production of ultracold $X^1\Sigma^+$ RbCs molecules. *Eur. Phys. J. D* **31**, 179 (2004).
80. Korek, M. Private communication (2009).
81. Zener, C. Non-Adiabatic Crossing of Energy Levels. *Proc. R. Soc. Lond. A* **137**, 696 (1932).
82. Landau, L. D. Zur Theorie der Energieübertragung. II. *Phys. Z.* **2**, 46 (1932).
83. Wittig, C. The Landau-Zener Formula. *J. Phys. Chem. B* **109**, 8428 (2005).
84. Wang, D. *et. al.* Rotationally resolved depletion spectroscopy of ultracold KRb molecules. *Phys. Rev. A.* **75**, 032511 (2007).
85. Chen, C., Yin, Y. & Elliott, D. S. Interference between optical transitions. *Phys. Rev. Lett.* **64**, 507 (1990).
86. Yamazaki, R. & Elliott, D. S. Observation of the Phase Lag in the Asymmetric Photoelectron Angular Distributions of Atomic Barium. *Phys. Rev. Lett.* **98**, 053001 (2007).

VITA

VITA

Adeel Altaf was born in Karachi, Pakistan. He attended Lafayette College for his undergraduate studies and graduated with a Bachelor of Science degree in 2006. He obtained a Masters of Science degree from Purdue University in 2008.